UCLA
UCLA Electronic Theses and Dissertations

Title
Dual-Mode Based Filters and Filtering Antennas

Permalink
https://escholarship.org/uc/item/67d6v711

Author
Dhwaj, Kirti

Publication Date
2018

Peer reviewed|Thesis/dissertation

eScholarship.org
Powered by the California Digital Library
University of California

UNIVERSITY OF CALIFORNIA
Los Angeles

Dual-Mode Based Filters and Filtering Antennas

A dissertation submitted in partial satisfaction
of the requirements for the degree
Doctor of Philosophy in Electrical Engineering

by

Kirti Dhwaj

2018

© Copyright by
Kirti Dhwaj
2018

ABSTRACT OF THE DISSERTATION

Dual-Mode Based
Filters and Filtering Antennas

by

Kirti Dhwaj
Doctor of Philosophy in Electrical Engineering
University of California, Los Angeles, 2018
Professor Tatsuo Itoh, Chair

The dissertation details several new filter and filtering antenna topologies. For filters, the novelties introduced include a microstrip version of Möbius loop resonator based filter, a packaged dual-band filter constituted by novel dual-mode and dual-resonance substrate integrated waveguide (SIW) cavities and a methodology for integration of planar resonators with SIW cavities in lieu of compact filtering structures. For the filtering antennas, flexible transmission zeroes (TZs) are introduced using source-load coupling, followed by the first single-layer SIW dual-band filtering antenna with orthogonal polarizations in the two bands. A methodology for synthesizing filtering antennas using coupling matrix synthesis is introduced. Also is shown a method of using multi-band filtering antennas to break the conventional limit of maximum possible n TZs from a n resonator filter. Finally, an on-chip resonant terahertz antenna with reasonable gain and bandwidth is reported.

The dissertation of Kirti Dhwaj is approved.

Chang-Jin Kim

Robert Candler

Yahyaa Rahmat-Samii

Tatsuo Itoh, Committee Chair

University of California, Los Angeles

2018

To Ma

and Ma-si

for being the cogs

that made my broken wheel spin

TABLE OF CONTENTS

LIST OF FIGURES

LIST OF TABLES

ACKNOWLEDGMENTS

I would like to thank Dr. Richard Snyder for being generous and enabling research on a topic marred by dearth of academic funding. Knowing that he would be part of my thesis committee (didn't actually transpire, courtesy some deft handling on part of UCLA) meant that there would be no easy ticket to the degree; it also meant that I graduate with a modest command over filter theory. It goes without saying that not much of it would have come about without my advisor, Tatsuo Itoh's guidance. He has been much more than an advisor to me. I lived in a protective cocoon that he spun around and the sunlight of real world has already started p(r)icking on me. Professor Chang-Jin Kim for spending much of his valuable time with a young student from a department not his own. Not much came out of the enlightening discussions I had with him – it does not mean nothing will. I firmly believe that time is a good leveller. I would also like to thank Professors Yahyaa Rahmat-Samii and Robert Chandler for agreeing to be in my PhD committee sparing their time and effort to improve the quality of this dissertaion. A very special thanks goes out to Professor Li Jun Jiang from the University of Hong Kong, who not only drove the research with his valuable inputs, but also provided for exquisite measurement facilities at his institute.

I would like to thank Sharam Mahdavi, for goading me into these long but delightful years in PhD. Noriaki Kaneda, for being a kind guide at Bell Labs and enabling my research through much needed finances. Jacky Chan, Cameron Gunn, Adeel Bajwa, Richard Al-Hadi, Jordan Budhu and Sebastian Broere for being the moral support that is such a necessity during PhD years. Xiaoqiang Li, for teaching me more than any book could - often through heated arguments. Cheng Tao and Haozhan Tian, for being patient, bearing with me and making the learning experience fun. Finally, and most importantly, my family–it wouldn't do justice to write out what I feel about them; words are not enough.

VITA

1994–2007	Lower Kinder Garten to Standard XII St. Anselms Pink City Sr. Secondary School, Jaipur, India.
2008–2012	B. Tech, Indian Institute of Information Technology Allahabad, India
2012–2014	M.S. (Electrical Engineering), UCLA, Los Angeles, USA.

PUBLICATIONS

Dhwaj K, Li X, Shen Z, Qin S. Cavity resonators do the trick: A packaged substrate integrated waveguide, dual-band filter. IEEE Microwave Magazine. 2016 Jan;17(1):58-64.

Dhwaj K, Kovitz JM, Tian H, Jiang LJ, Itoh T. Half-Mode Cavity-Based Planar Filtering Antenna With Controllable Transmission Zeroes. IEEE Antennas and Wireless Propagation Letters. 2018 May;17(5):833-6.

Dhwaj K, Li X, Jiang LJ, Itoh T. Low-Profile Diplexing Filter/Antenna Based on Common Radiating Cavity With Quasi-Elliptic Response. IEEE Antennas and Wireless Propagation Letters. 2018 Oct;17(10):1783-7.

Dhwaj K, Kovitz JM, Al-Hadi R, Itoh T. Compact dual-band filtering antenna based on capacitor loaded patch radiator. InMicrowave Conference (APMC), 2017 IEEE Asia Pacific 2017 Nov 13 (pp. 1188-1191). IEEE.

Dhwaj K, Wu CT, Itoh T. Reconfigurable UWB bandpass filter with flexible notch characteristics. InMicrowave Conference (APMC), 2014 Asia-Pacific 2014 Nov 4 (pp. 100-102). IEEE.

Dhwaj K, Lee H, Jiang L, Itoh T. Transmission-line equivalent and microstrip structure for planar Möbius loop resonator. InMicrowave Symposium (IMS), 2015 IEEE MTT-S International 2015 May 17 (pp. 1-3). IEEE.

Dhwaj K, Zhao Y, Al Hadi R, Li X, Chang FM, Itoh T. A 0.55 THz On-Chip Substrate Integrated Waveguide Antenna. In2018 43rd International Conference on Infrared, Millimeter, and Terahertz Waves (IRMMW-THz) 2018 Sep 9 (pp. 1-2). IEEE.

Dhwaj K, Qin S, Jiang LJ, Itoh T. Tunable transmission zeroes bandpass filter with external quality factor control. InMicrowave Conference (APMC), 2016 Asia-Pacific 2016 Dec 5 (pp. 1-4). IEEE.

Dhwaj K, Tian H, Itoh T. Low-Profile Dual-Band Filtering Antenna Using Common Planar Cavity. IEEE Antennas and Wireless Propagation Letters. 2018 May 3.

Dhwaj K, Hadi R, Yang T, Jiang LJ, Kovitz J, Itoh T. Planar Resonator Embedded Substrate Integrated Waveguide (SIW) Cavity Filter. In2018 48th European Microwave Conference (EuMC) 2018 Sep 23 (pp. 761-764). IEEE.

Dhwaj K, Jiang L, Itoh T. Dual-Band Filtering Antenna with Novel Transmission Zero Characteristics. IEEE Antennas and Wireless Propagation Letters. 2018 Oct 29.

Dhwaj K, Jiang LJ, Itoh T. Microstrip diplexer with low channel-frequency ratio. InMicrowave Conference (APMC), 2016 Asia-Pacific 2016 Dec 5 (pp. 1-4). IEEE.

CHAPTER 1

Introduction

Frequency filters [1] are important components of communication systems. They are used to separate or combine multiple frequency bands. More importantly, they are used to select the appropriate frequencies from the electromagnetic spectrum. As the spectrum – limited in range – adds on new communication standards, filter designers are presented with stricter requirements and new functionalities.

Traditionally, in a RF front end, the filter and antenna are designed independantly and connected through a transmission line (Fig.1.1 (a)). On the other hand, if the last resonator of a traditional bandpass filter network is replaced by a radiating resonator (antenna), size compactness can be achieved (FIg.1 (b)).

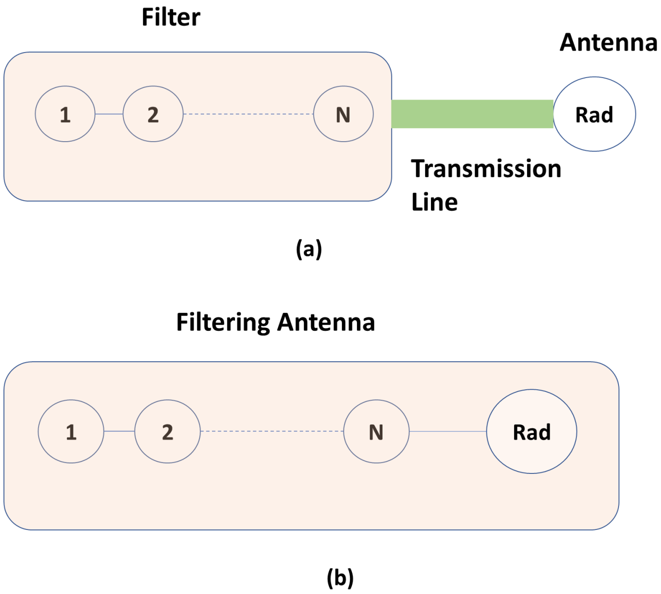

Figure 1.1: (a) Traditional arrangement of a filter and antenna. (b) Integrated Filter/ Antenna. All nodes represent resonators.

Antenna design in sub-millimeter wave region becomes difficult as the chip manufacturing technology is geared towards circuit design and does not cater to electromagnetic radiation. Primary factors are the low resistivity and high dielectric constant of semiconductor processs silicon. Increasing gain and bandwidth of the antenna, thus become major objectives of sub-mmW IC design.

This document aims to provide solutions for the practical problems described above through topologies based on dual-mode resonators. Chapter 2 would deal with compact filtering structures and emphasizes on suppression of out-of-band signal using transmission zeroes. Chapter 3 would present several novel integrated filter/antenna designs with characteristics such as transmission zeroes, multi-band and multi-channel responses. Finally, Chapter 4 would introduce a THz antenna with the highest ever gain and bandwidth reported for an on-chip resonant type antenna. The forthcoming chapters start with their own extensive introduction parts, which would build into the theory of the next sections.

All the designs were implemented on a single-layer printed circuit board (PCB) using conventional PCB manufacturing technology [2] at the UCLA Centre of High Frequency Electronics (CHFE) attesting to their simple and inexpansive nature. It should be noted that a dual-mode resonator necesserily has two degenerate modes in the same structure, with mutually orthogonal field distributions. Although the general theme of the dissertation is the use of dual-mode structures for achieving the desired responses, a few of the structures are not strictly dual-mode and use resonances of two different modes for realizing the passbands.

CHAPTER 2

Microwave Filters

2.1 General Concepts

The most obvious application for microwave filters is for rejecting the unwanted frequencies and only allowing the good frequencies to pass through. Another application is to use a series of filters for combining (MUX) or seperating (DEMUX) a range of frequency channels (Fig. 2.1). Again, as shown by Bode [3], an wideband impedance matching network is essentially a bandpass filter with no reflections in the passband and sharp rejections of frequencies outside the passband.

For a simple microwave transmitter, a channel filter is needed after the upconverter to filter out all the non-linear effects. A MUX is then needed to combine all the RF signals to be transponded by a single antenna. Similarly, a receiver would have a input filter right before the LNA to maximize the LNA's signal to noise ratio. Again, if the signal needs to be sent to different channels a DEMUX would be used at the end of the RF block. An excellent systemic review of microwave filters in communication channels is given in Chapter 1 of [4].

As described above, a filter selects a band of frequencies to be passed from a source to load. The voltage attenuation function of a filter, T(p) is given as

$$T(p) = \frac{E_L}{E_s} = c\frac{(p-p_1)(p-p_3)....(p-p_{2n-1})}{(p-p_2)(p-p_4)....(p-p_{2l})} \tag{2.1}$$

where E_L and E_S are the voltage levels at the load and source respectively, c is a constant and p is a complex frequency variable [5].

The locations p_1, p_3... where T(p) $=$ 0 are called the reflection zeroes (RZs) of the filter and would be referred to as "(transmission) poles" of the filter in the manuscript from

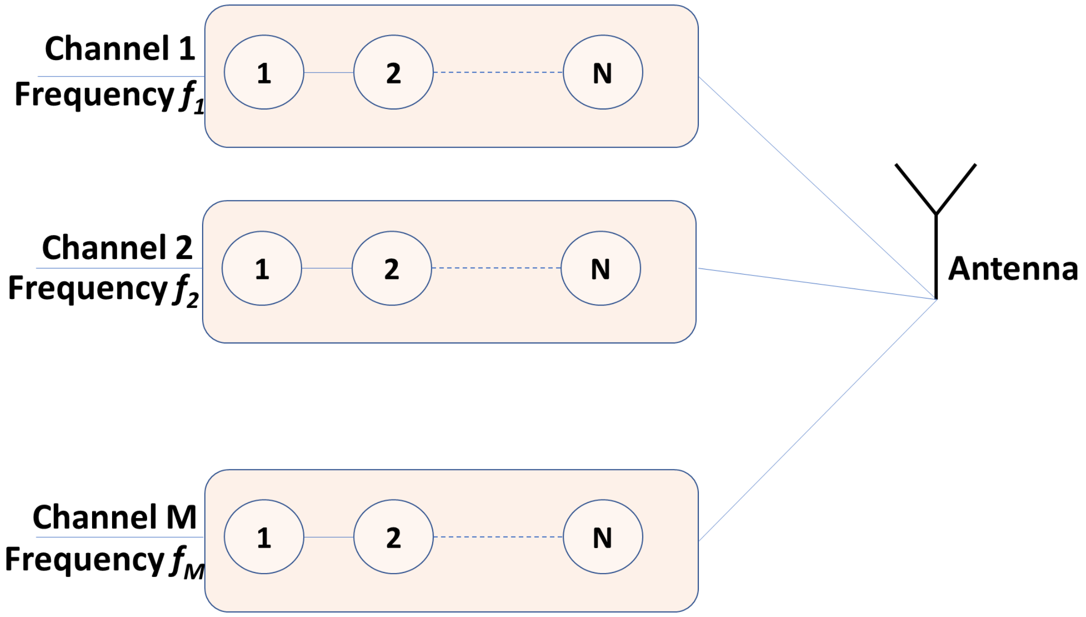

Figure 2.1: Schematic of a Mux/Demux connected to an antenna.

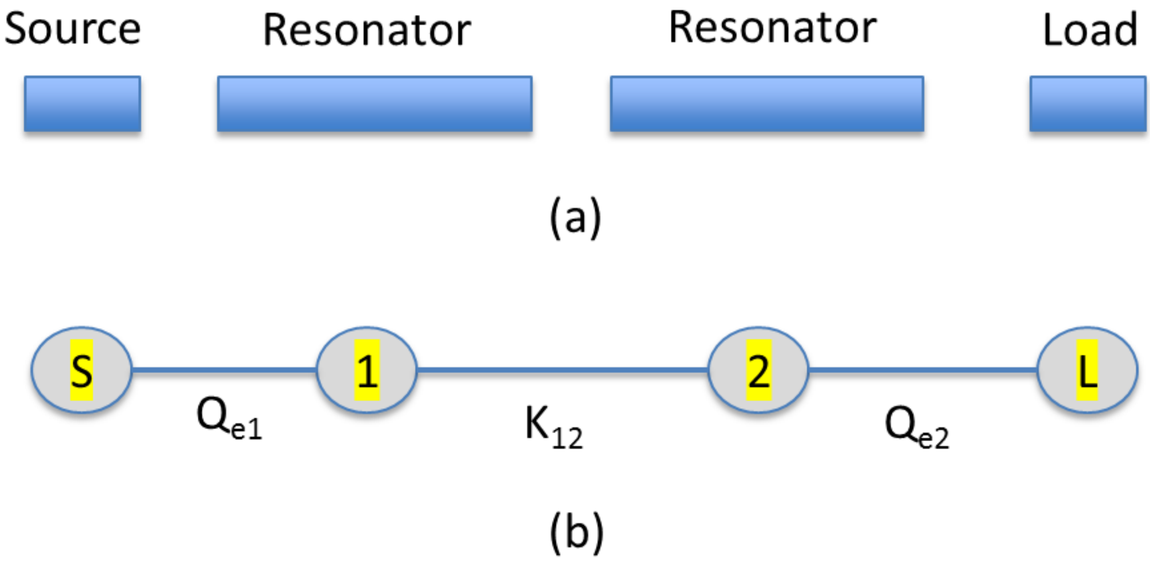

Figure 2.2: (a) A two pole transmission line-based filter. (b) Its coupling scheme.

hereon. These locations are where the transmision loss for a filter is minimum. The number n denotes the number of poles – or the order – of the filter. For example, in Fig. 2.2(a), a transmission-line two pole filter is presented. Each resonator is responsible for producing a pole in the frequency response of the filter and each component of the filter is coupled to the

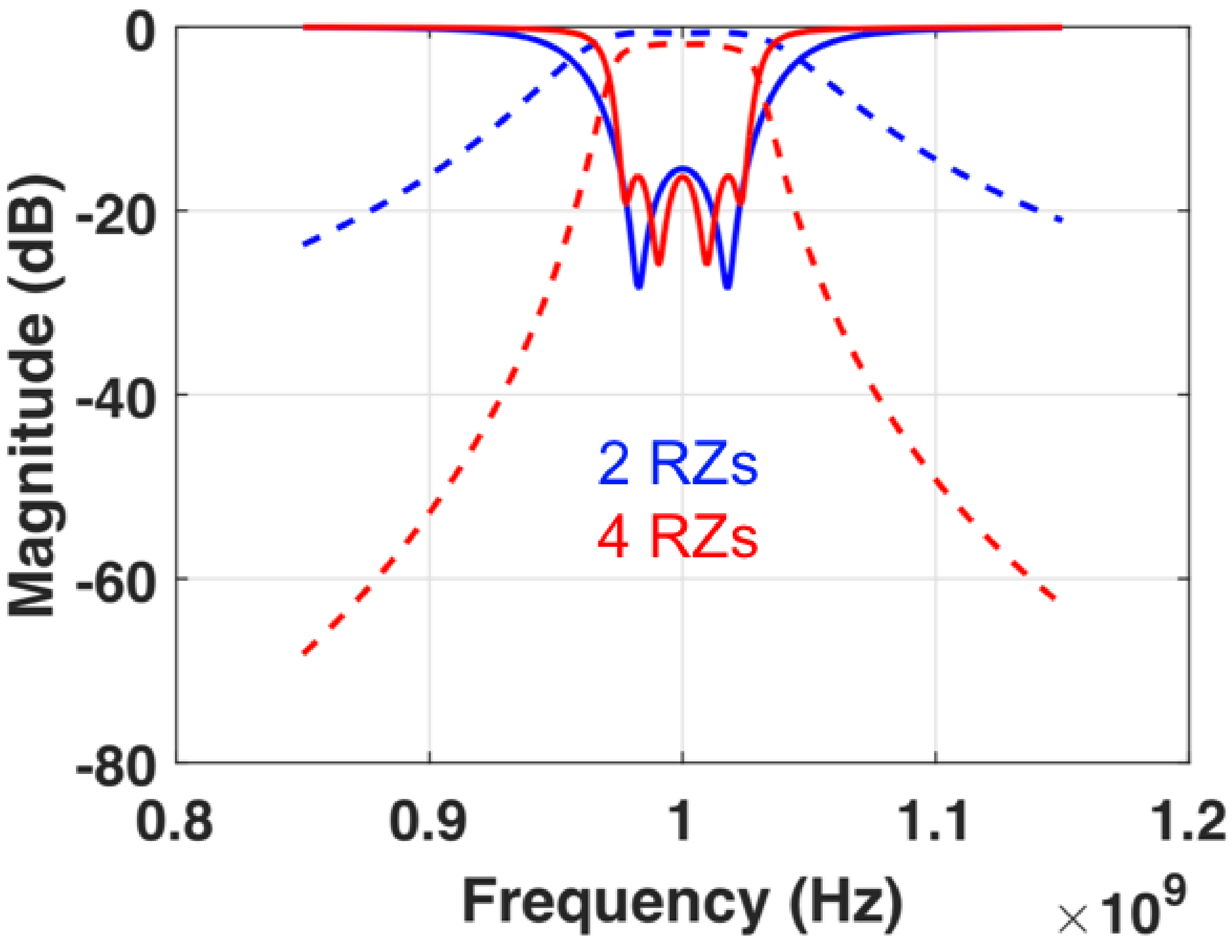

Figure 2.3: Comparison between two pole (or RZs) and four pole filter for the same bandwidth and ripple level. Dashed lines represent S_{21}, while the solid ones represent S_{11}

adjacent one through end-to-end coupling. The filter can be better represented through the coupling schemes in Fig. 2.2 (b), where each node represents a component in the coupled-resonator circuit, the coupling factor K_{12} represents the coupling between the two resonators and the parameters Q_{e1} and Q_{e2} represent the external quality factors of the two resonators respectively. A higher order filter offers higher selectivity (Fig. 2.3), but at the cost of increased size and material loss in the filter.

Earlier techniques for bandpass microwave filter synthesis relied mainly on bandpass transformation from prototype low-pass filters [5]. These low-pass filters would have their elemental values given by look-up tables and would subscribe to a given symmetric filter type i.e, Bessel, Butterworth, Tchebyesheff, Elliptic etc.

Lately, the coupling matrix method of synthesis has garnered increased favour and attention from microwave engineers as it allows various configurations of resonators and arbitrary responses to be synthesized [4]. Matrix operations allow for inversion and partitioning thereby simplifying the synthesis, reconfiguration and partitioning of the network. Each element in the coupling matrix represents an element in the filter, thereby making debugging intuitive.

The coupling matrix m of a n-order filter is given as:

$$\begin{bmatrix} m \end{bmatrix} = \begin{bmatrix} 0 & m_{S1} & m_{S2} & m_{S3} & \dots & m_{Sn} & m_{SL} \\ m_{1S} & m_{11} & m_{12} & m_{13} & \dots & m_{1n} & m_{1L} \\ m_{2S} & m_{21} & m_{22} & m_{23} & \dots & m_{2n} & m_{2L} \\ \vdots & \vdots & \vdots & \vdots & \ddots & \vdots & \vdots \\ m_{nS} & m_{n1} & m_{n2} & m_{n3} & \dots & m_{nn} & m_{nL} \\ m_{LS} & m_{L1} & m_{L2} & m_{L3} & \dots & m_{Ln} & 0 \end{bmatrix}$$

with the scattering parameters given as:

$$\begin{aligned} S_{21} &= -2j[A]^{-1}{}_{n+2,1} \\ S_{11} &= 1 + 2j[A]^{-1}{}_{1,1} \end{aligned} \tag{2.2}$$

The matrix [A] is given by

$$[A] = [m] + \Omega[U] - j[q] \tag{2.3}$$

in which [U] is a unitary identity matrix, except $[U]_{11} = [U]_{nn} = 0$, [q] is a null matrix except $[U]_{11} = [U]_{nn} = 1$ and $\Omega = \frac{1}{FBW}(\frac{f}{f_0} - \frac{f_0}{f})$ with FBW being the 3-dB bandwidth at the operating frequency f_0.

The elements of matrix [m] are related to coupling coefficents as:

$$K_{ij} = FBW.m_{ij} \tag{2.4}$$

and with the external coupling coefficients as

$$Q_{e,iS} = \frac{1}{FBW.m_{iS}^2} \tag{2.5}$$

with i and j being the resonator indices.

It is quite clear from the above equations, that if a desired response of the filter is known, a matrix [m] can be derived exhibiting the said response. This can happen through low-pass prototype development and optimization [6, 7]. The coupling factor, in turn, can be extracted from the physical structure in an electromagnetic simulator by extracting the resonance frequencies and using the formula [1]:

$$\begin{gathered} K = \frac{1}{2}\Big(\frac{f_i}{f_j} + \frac{f_i}{f_j}\Big)\times \\ \sqrt{\Big(\frac{f_{0i}^2 - f_{0j}^2}{f_{0i}^2 + f_2^2}\Big)^2 - \Big(\frac{{f_i}^2 - {f_j}^2}{{f_i}^2 + {f_j}^2}\Big)^2} \end{gathered} \tag{2.6}$$

where

f_i and f_j are the natural resonance frequencies of the two resonators in question

f_{0i} and f_{0j} are the resonance frequencies obtained when the two resonators are coupled together

and the external quality factor is given as

$$Q_{e,i} = \frac{f_{0i}.\tau}{4} \tag{2.7}$$

where τ is the reflection group delay of resonator i at f_{0i}.

Finally, the source-to-load coupling factor K_{SL} is used to create transmission zeroes (TZs) in the frequency response of the filter. It is not calculated directly, but a one-to-one mapping is created through TZ locations in EM simulation of filter and calculation of its equivalent structure.

The TZs, as mentioned above are an extremely useful parameter of filter synthesis. They are used for phase equalization, increasing selectivity without increasing the order and creating stop-bands in the frequency response of the filter [4]. The TZs are created when

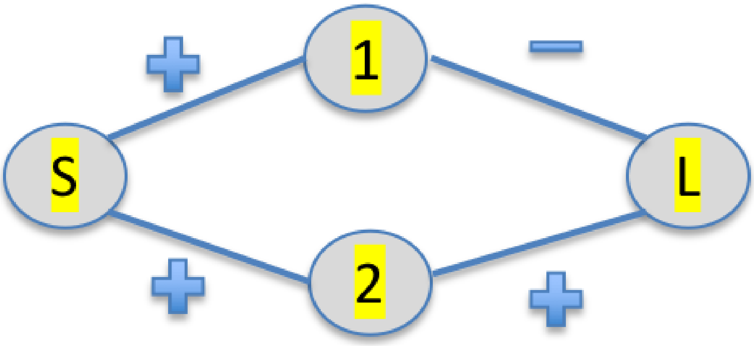

Figure 2.4: Cross-coupling to produce a TZ in a two-pole filter

cross-coupling is present in the filter network (Fig. 2.4). The cross-coupling is defined as an alternate path that a signal can take between the source and the load. The two paths necesserily need to be of opposite phasing to produce TZs in the frequency response of the filter (Fig. 2.5). This cross-coupling is also responsible for causing linear phase response of the filter, but the topic is out of scope of this document.

2.2 Transmission-Line Equivalent and Microstrip Structure for Planar Möbius Loop Resonator [8]

A Möbius strip can be formed by taking a strip of paper, giving it a half twist and joining the ends of the strip to form a loop. If an ant is to start at a point on the seam of the strip, crawl along the length of the seam and reach the same point again, it would have walked along the entire length of both sides of the paper strip. That is, the path length on a Möbius strip is twice as that of the paper strip used to make it. In other words, the Möbius strip has a single boundary [9]. The Möbius topology has been previously used for implementing passive electrical components such as non-inductive resistor [10], signal retention device [11] and Möbius-coupled signal sources [12]. Printed Möbius loop resonators were introduced and used as constituent elements of bandpass filters by Jeffrey M. Pond [13].

The structure of Pond's Möbius Loop resonator is shown in Fig. 2.6. It has been claimed by the author that the “half twist” or 180° phase shift is provided by the shorting vias

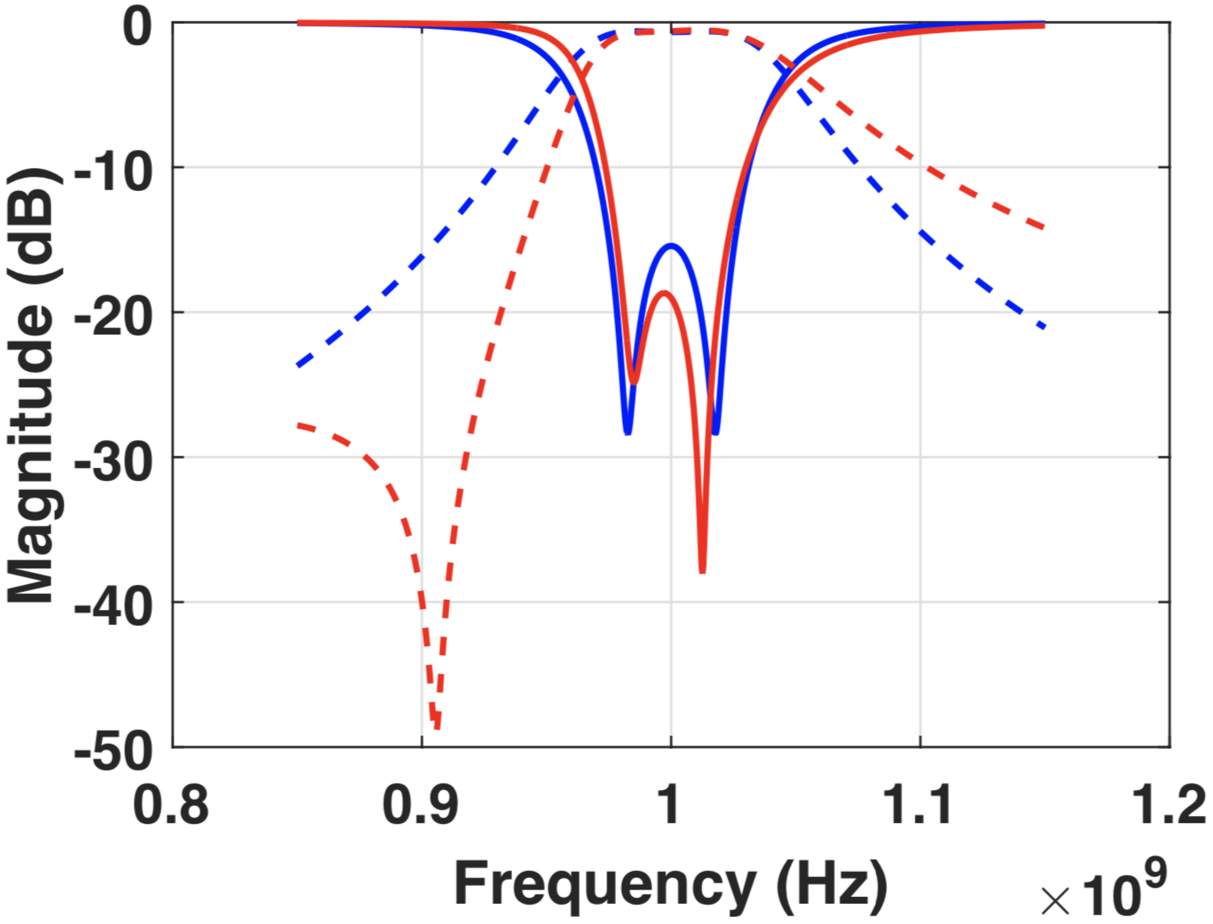

Figure 2.5: Frequency response of a two-pole filter with (red) and without cross-coupling (blue). The dashed lines represent S_{21} characteristics, while the solid lines represent the S_{11} characteristics.

across the substrate. The resonator, when tested, behaves as a dual mode filter with two transmission zeroes on either sides of the passband.

Here, we attempt to provide a robust theoretical basis for the Möbius loop structure through a transmission-line model. It is shown that the presence of vias act as electromagnetic perturbations, which account for the dual-mode resonances of the Möbius loop structure. Also, the effect of coupling factor between the two degenerate modes on the pair of transmission zeroes is observed. The transmission line model lends itself to the implementation of Möbius loop resonator in various types of transmission lines. Finally, a microstrip equivalent of Pond's planar Möbius loop resonator is presented.

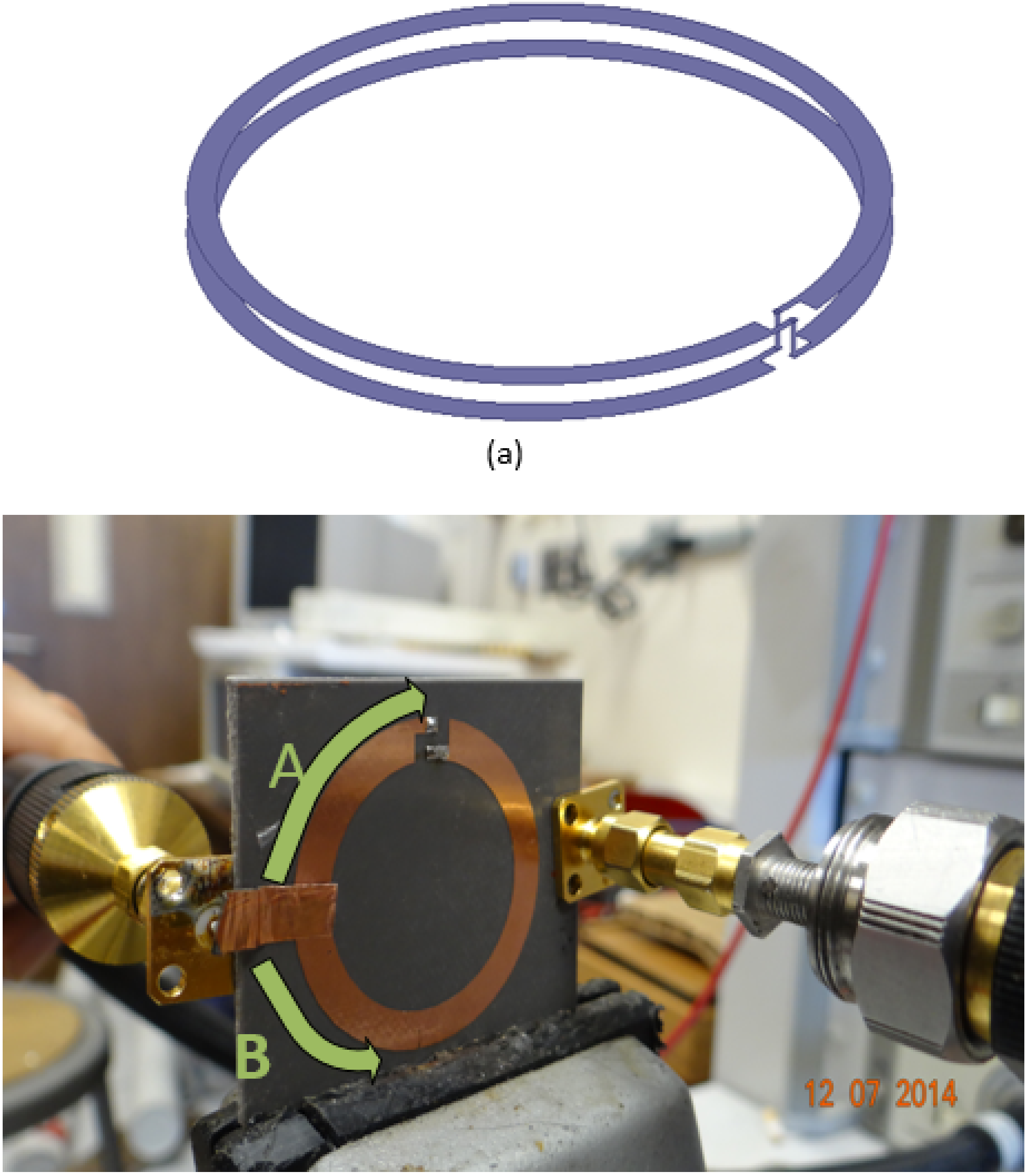

(a)

(b)

Figure 2.6: (a) Schematic and (b) Structure of the Möbius Loop resonator presented in [13].

2.2.1 Transmission-Line Model

Before proceeding to make the transmission line model for the Möbius loop resonator, it is necessary to trace the signal flow from one port to another. In the structure presented

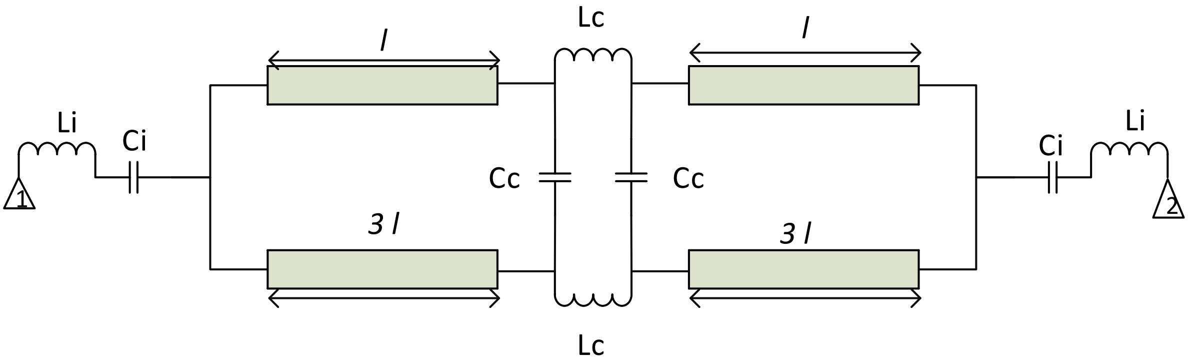

Figure 2.7: Transmission-line equivalent model of the planar Möbius loop resonator.

by Pond (2.6(b)), the Möbius loop resonator is a two layered structure with input and outpot ports lying on the opposite faces of the substrate. The input and output signals are capacitively coupled to the resonator in a broadside manner. This is achieved by depositing metal overlays over thin dielectrics. Once the signal enters a port, it gets divided into two branches. The path **A** shown in Fig.2.6(b) makes the signal travel a phase $\phi = 90°$, travel through via to the other face of substrate and again travel $\phi = 90°$ before coming out of the second port. On the other hand, the signal through the path B has to travel a corresponding angle $\theta = 3\phi$. That is, the length of path **B** is three times that of **A**.

The transmission-line equivalent of the resonator is shown in Fig.2.7. It can be seen that the length of the transmission lines in the bottom branch (corresponding to signal path **B**) is thrice of the corresponding lines in the top branch. The total length of the transmission line is such that combined electrical length is 360°at the resonant frequency. Lc represents the inductance of shorting vias, whereas Cc denotes the capacitive coupling between the two vias and the metal strips on two sides of the substrate. Also, Ci gives the capacitance between the metal overlays and Möbius resonator and Li the inductance of the inner conductor of coaxial cable. The response of the model is shown in Fig.2.8. It can be clearly seen that the model response has two transmission poles and two transmission zeroes, as depicted in Pond's paper.

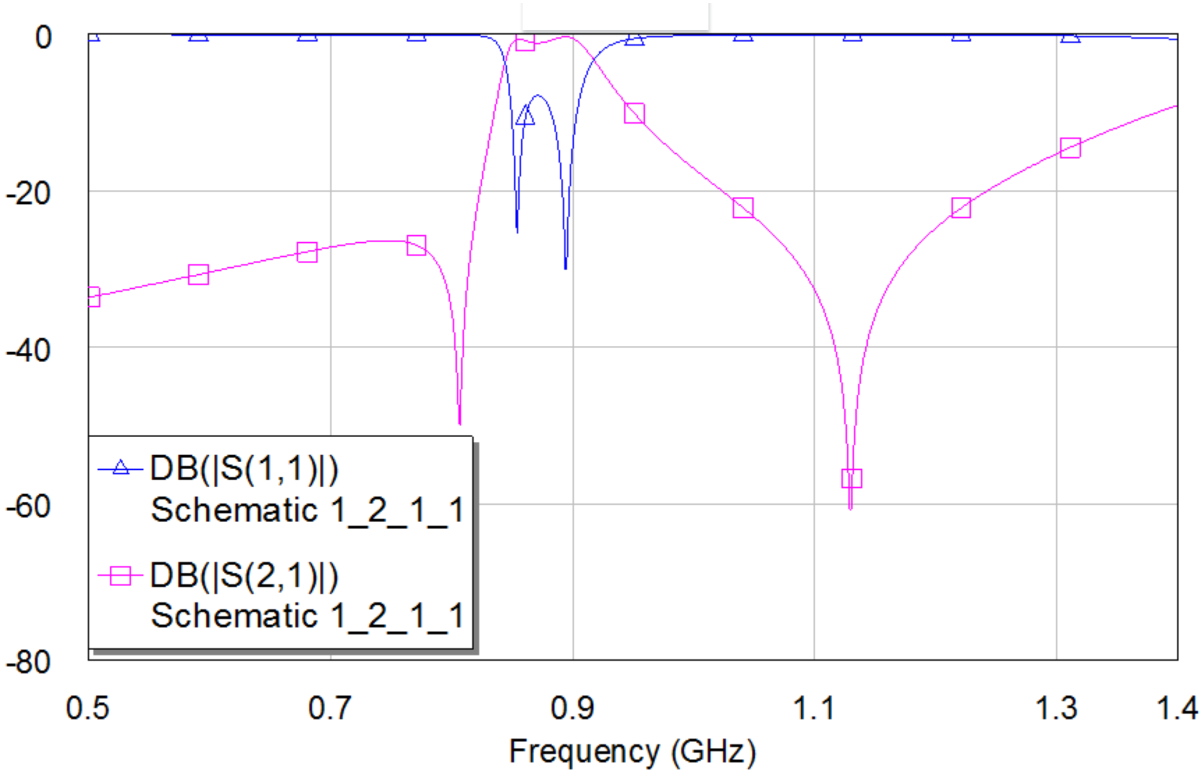

Figure 2.8: Response of the transmission-line model.

2.2.1.1 Dual-Mode Resonance

We say that it is the presence of perturbations due to the capacitive and inductive couplings produced by via structure and two strips of resonator that makes the two modes of resonance possible. To prove our point, we proceed with the even-odd mode analysis of our model. Let us drop the coax inductance and overlay capacitances from the transmission line model to analyze the natural resonance frequencies of the two orthogonal modes in the resonator. We place an *open* plane at the axis of symmetry for even mode(Fig.2.9(a)) analysis, whereas a *short* plane for odd mode(Fig.2.9(b)) analysis.

In case of even-mode analysis, as shown in Fig.2.9(a), the resonance happens when the shown transmission line is half-wavelength long at the resonance frequency. It means that the total transmission line length of the Möbius loop resonator is one wavelength long at the resonant frequency. The behaviour is similar to a closed-loop ring resonator.

On the other hand, for the odd mode (Fig.2.9(b)), the coupling capacitance Cc and via

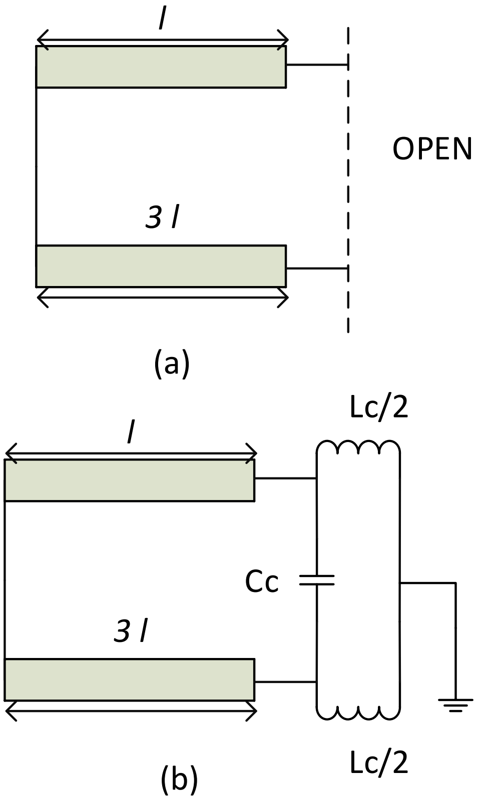

Figure 2.9: (a) Even and (b) Odd mode equivalent circuits of the Möbius loop resonator.

inductance Li are both present. It shows that the resonance frequency of the odd-mode would be different from that of the even-mode. For verification, we varied Cc in our model. We observed that only the lower resonance frequency moves with the change of coupling capacitance, Cc. Thus, it can be safely said that the lower resonant frequency is the odd-mode resonance of the Möbius loop resonator.

2.2.1.2 Transmission Zeroes

As described before, TZs are caused due to cross-coupling in the filtering network. However, a single cross-coupling path as shown in Fig. 2.4 would only produce a single TZ. The presence of second TZ in the frequency response of the Möbius loop resonator-based filter can be explained by considering the parasitic source-load coupling in Fig. 2.10. In the coupling scheme, clearly node *1* represents the odd mode, while *2* is for the even mode. The

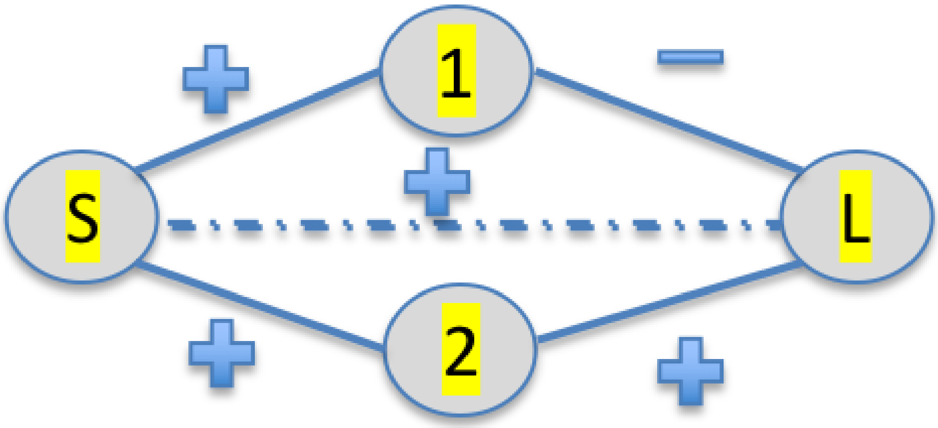

Figure 2.10: Coupling scheme of the Möbius loop resonator based filter with positive sign denoting electrical coupling.

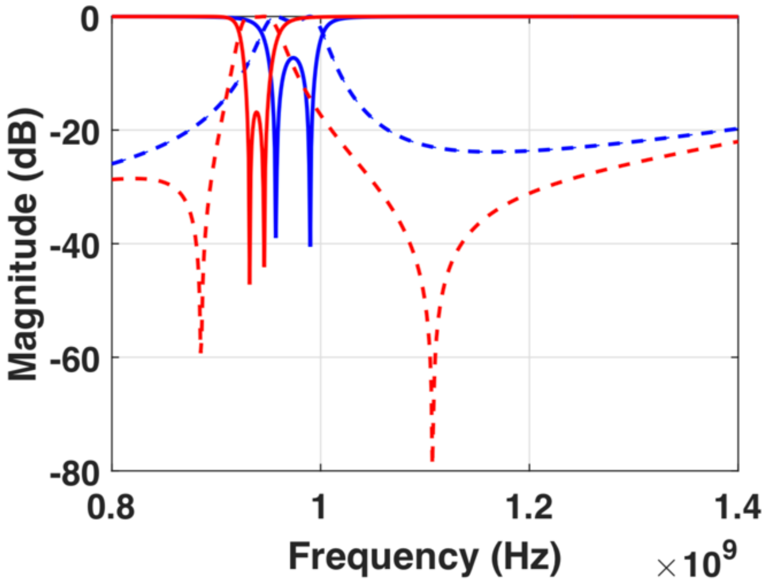

Figure 2.11: Response of the coupling scheme in Fig. 2.10 with $f_o < f_e$ (or $Cc > 0$)(red) and with $f_o > f_e$ (blue). The dashed lines represent S_{21} characteristics, while the solid lines represent the S_{11} characteristics.

response of the coupling scheme (Fig. 2.11) shows that the the pair of TZs are only present when odd-mode resonance frequency (f_o) is smaller than that of the even mode (f_e).

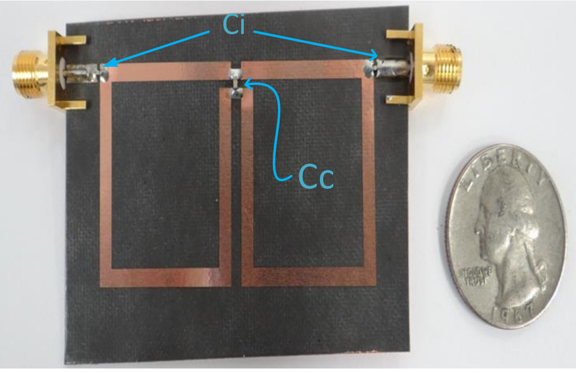

Figure 2.12: Fabricated filter based on microstrip Möbius loop resonator.

2.2.2 Microstrip Möbius Loop Resonator-Based Filter

While the Möbius loop resonator presented in [13] does reduce the volume of the resonator by vertically stacking it into two equal parts, the structure is not convenient for planar integration. The structure has four metal layers with input and output coupled to the resonator using thin dielectric layers only at the feeding points. Also, lack of a clear ground plane makes the use of the structure in planar transmission line technology difficult.

Now that we have a transmission line model for the Möbius loop resonator, it is possible to implement the resonator by various transmission lines. In this section, we present a microstrip version of the Möbius loop resonator.

Shown in Fig.2.12 is the fabricated vialess microstrip Möbius loop resonator-based filter on a 0.79mm Rogers RT5880 substrate ($\epsilon_r = 2.2$). The length of the transmission line in upper branch is 52mm. The lower branch is three times the length of upper branch. Both transmission lines are 2.5mm wide (100Ω). At the mid-section of both branches are thin strips (1.5mm) of metal, acting as inductors Lc (the via inductance; shown in Fig.2). These metal strips are connected to each other using a chip capacitor for introducing the coupling capacitance Cc. The value of the chip capacitor Cc is 0.75pF. Also, both the input and output ports are coupled to the resonator by input capacitance $Ci(=1.5\text{pF})$.

Fig.2.13 shows the measured results of the microstrip resonator. It is plain to see that the structure exhibits the two transmission zeroes and transmission poles as in [13]. The

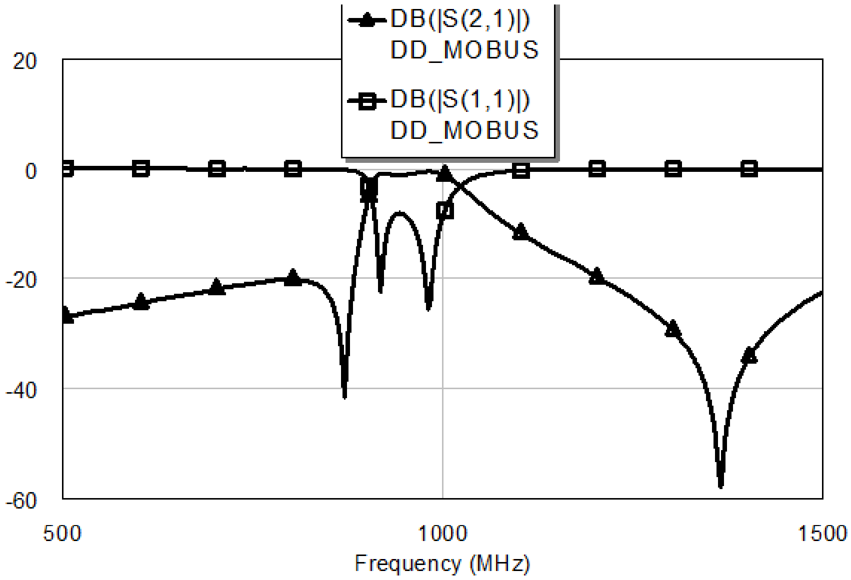

Figure 2.13: Measured frequency response of the microstrip Möbius loop resonator based filter.

result also corroborates our transmission line model. The nature of the response is similar to the one shown in Fig.2.8.

2.3 Packaged Substrate Integrated Waveguide (SIW) Dual-Band Filter [14]

Dual-mode resonator based filters have become mainstay of many communication systems, especially those associated with satellites. The most common topologies used to realize these filtering fucntions at microwave frequencies have been the waveguide cavities and the dielectric resonators [15]. As much as the dual-mode resonator based filters have smaller form factor and weight compared to single-mode resonator beased filters, further miniaturization is needed to satisfy the fuiture satellite and mobile communication systems requirements. Microstrip filters [1] have been touted as veritable solution to the problem - not only do they offer self-equalization and elliptic responses but can also make use of the high temperature superconducting technology [4]. However, the microstrip technology is rather low Q for satellite applications - thereby calling for a PCB based solution which has higher Q compared to microstrip resonators. Again, the dielectric based microwave components are needed to be packaged to prevent environmental damage. Substrate Integrated Waveguide (SIW) technology offers high- Q cavities in planar form [16]. Quite like the waveguide cavities, SIW technology allows for implementation of dual-mode resonator based filters [17, 18].

The dual-band filter presented in this section has to conform to the following requirements:

- Passband 1 should have a fractional bandwidth of 4 %, centered around 10 GHz.
- Passband 1 should have a fractional bandwidth of 4 %, centered around 14 GHz.
- Both bands need a minimum two-pole response.
- Maximum inter-band suppression.
- PCB to be placed in a stratedge package with cross-section smaller than λ x λ, where λ is the free space wavelength at operating frequency of lower band.

For realizing the filter, two new SIW cavities, one a dual-mode circular cavity and the second one that combines two non-degenrate modes to form the passband are presented. Both the cavities operate at a band each and are connected through microstrip lines to form the dual-band filter.

2.3.1 14 GHz Dual-Mode cavity

The design of the filter for 14 GHz is based on dual-mode circular cavity resonator. Dual mode resonators are formed by perturbing the degenerate modes of a resonator [17]. The perturbation leads to different resonance frequencies for the two degenerate modes. The common ways to add perturbations are adding slots, cuts, or small patches that change the electric field pattern of the modes. The rectangular cavity is the most intuitive choice for the SIW filter given the package constraints. However, note that SIW only support TM modes. Provided the height of the substrate is small (the constraint of 0.88 mm provided by the package), it is difficult to get small frequency ratio between two modes of a rectangular cavity (at 14 GHz) in a constrained space without producing spurious resonances at lower frequencies which degrade the rejection of the filter [19]. On the other hand, the circular cavities have the axial field distribution of the form

$$A_m(\phi) = sin(m\phi) + cos(m\phi) \tag{2.8}$$

where A represents fields associated with the mth mode of the resonator, ϕ denotes the angle in the axial direction. From (2.8), it is clear to see that the odd (sin) and even (cos) modes can be independently controlled by proper perturbations.

To achieve a dual mode, we chose the TM_{110} mode because the TM_{010} does not provide the flexibility to tune the even and odd modes independently. Meanwhile, when TM_{110} is at 14 GHz, the TM_{010} mode will be at around 8.79 GHz, which is below the lower passband (10 GHz) [19]

For the filter design, the substrate is a 25-mil-thick Rogers TMM 10 with a relative dielectric constant of 9.8 and loss tangent of 0.0022. A large dielectric constant is chosen to make a compact design that fits in the StratEdge package. Thicker substrate is preferred as it corresponds to a wider fabricated 50 Ω microstrip transmission line. Both sides of the substrate are cladded with copper of 35 μm thickness. The substrate is mechanically hard, inflexible and thus robust during the fabrication process.

The design of the cavity is shown in Fig 2.14. It is a circular SIW cavity with two feeding lines being perpendicular to each other. For TM_{110}, from (2.8), it can be shown that if A represents electrical field, the maxima of the even mode would lie on the symmetrical plane, while that of the odd mode would lie on the asymmetrical plane. From Fig. 2.14, it can be observed that in the presented design, the vias on the asymmetrical plane are moved in a certain distance, thereby changing the natural resonance frequency of the odd mode. This makes the cavity act as a dual-mode resonator. Moving the vias inside the cavity on the asymmetrical plane makes the effective size for the odd mode smaller than that for even mode. This technique allows for the control of the filter bandwidth [20]. The electric field distribution for the even and odd mode is shown in Fig. 2.15. The coupling diagram of the

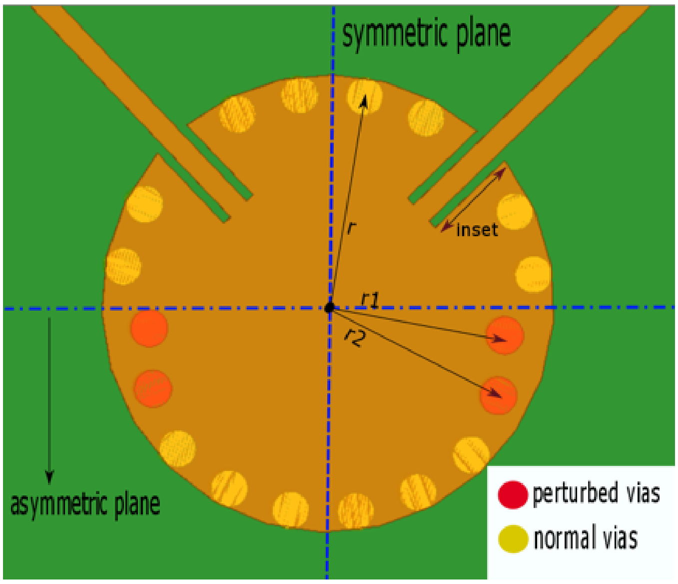

Figure 2.14: Schematic of the SIW cavity for 14 GHz, r=4.5mm, r1=4.1mm, r2=4.3mm, inset=2.1mm

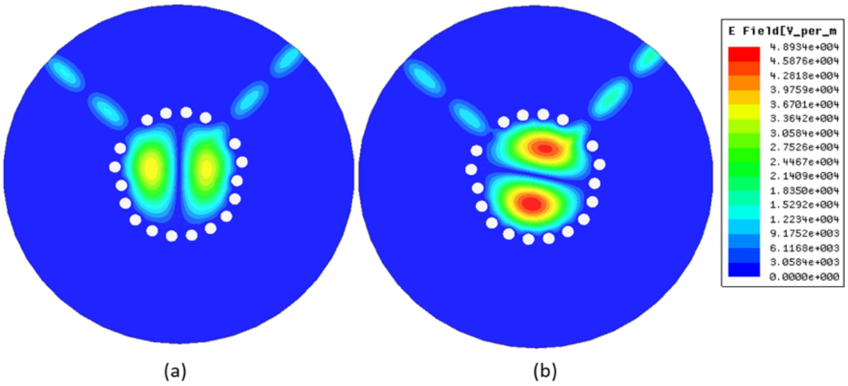

(a)

(b)

Figure 2.15: Electric field distribution for (a) the odd mode (14.22 GHz) and (b) the even mode (13.82 GHz).

cavity based filter is that of a doublet (Fig. 2.16), which allows for presence of two TZs in the frequency response.

Simulation of the SIW cavity shows that the center frequency of the passband is 14.02 GHz, the insertion loss is around 1.61 dB, and the 3-dB fractional bandwidth is 4.0% (Fig. 2.17). Also, the out-of-band rejection between 10 GHz and 13.5 GHz is more than 25 dB with the presence of transmission zero.

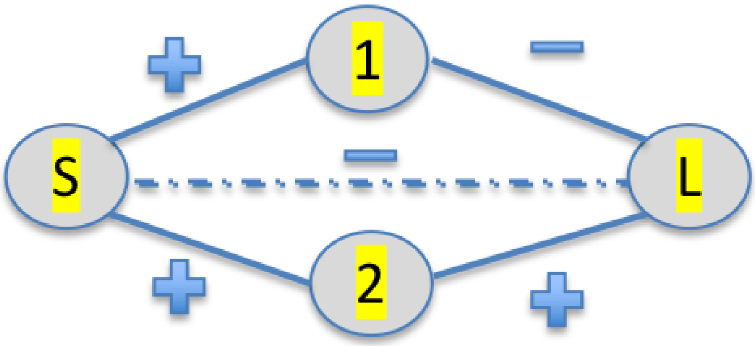

Figure 2.16: Coupling scheme of the dual-mode resonator based filter, with $Q_{e1} = 39.63$ and $Q_{e2} = 45.22$

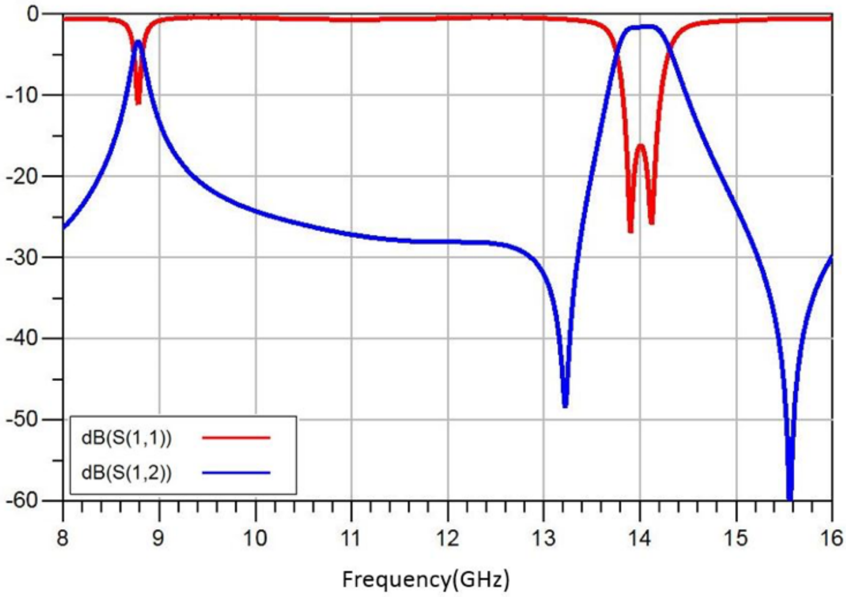

Figure 2.17: Simulated return loss and insertion loss of the 14 GHz SIW cavity

2.3.2 10 GHz Dual Resonance Cavity

Employing the perturbation theory mentioned in the previous section, we can again create a dual-mode resonator at 10 GHz. The topology will be similar and we only need to scale it for lower frequency. However, a critical problem arises since the frequency ratio of mode TM_{110} and TM_{210} in a circular cavity is 1.34 [19]. So when the TM_{110} mode works at around 10 GHz, another mode will appear at around 14 GHz, which is exactly the higher band in

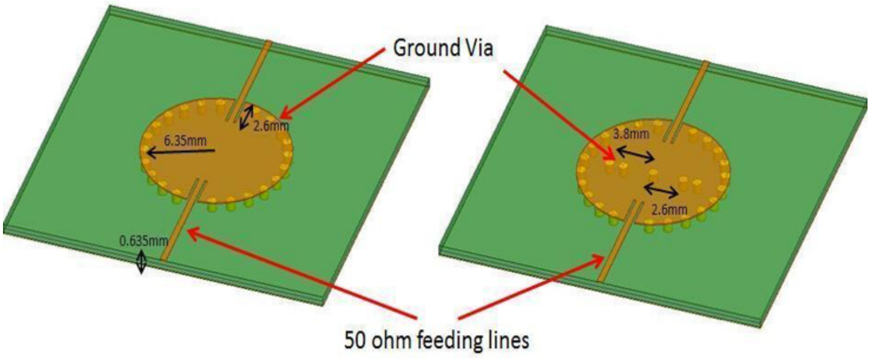

Figure 2.18: Schematics of the SIW cavity for 10 GHz (a) without and (b) with the perturbing copper vias.

demand. Since we want two different resonators to work on the bands separately without affecting each other, we need to avoid such a circumstance. Therefore, another method should be proposed to create the lower passband.

For this case, we try to create a dual-mode resonator by placing copper pins inside the cavity (Fig. 2.18). Since only TM modes exist inside the SIW structure, there will be electrical fields perpendicular to the cavity surface. That is to say that the electric fields are tangential to the copper pins (vias). According to the boundary conditions for metals, the electric field on the copper surface would be forced to be zero. As a result, the field distribution inside the cavity will be distorted, creating a frequency shift for the related cavity modes.

The argument for placing the copper vias at the locations described in Fig. 2.18 can be explained by the field distributions of different modes shown in Fig. 2.19. For TM_{110} mode, since the ground pins are placed at the location where the electric field itself is zero, such a process will not make any difference. On the other hand, for TM_{010} mode and TM_{210} mode, the pins will perturb the field, making the equivalent size of the cavity smaller and increasing the resonant frequencies in return. Therefore, we not only exclude the TM_{210} mode from the higher passband by increasing its frequency, but also shift the TM_{010} mode higher and use it to create a second order resonance at around 10 GHz by combining it with the TM_{110} mode. The S-parameters of the case before placing the pins as well as the case after are

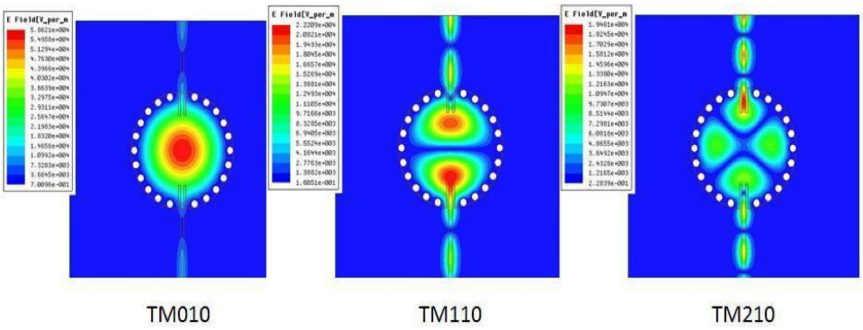

Figure 2.19: The field distribution of TM_{010} mode, TM_{110} mode and TM_{210} mode for the 10 GHz cavity.

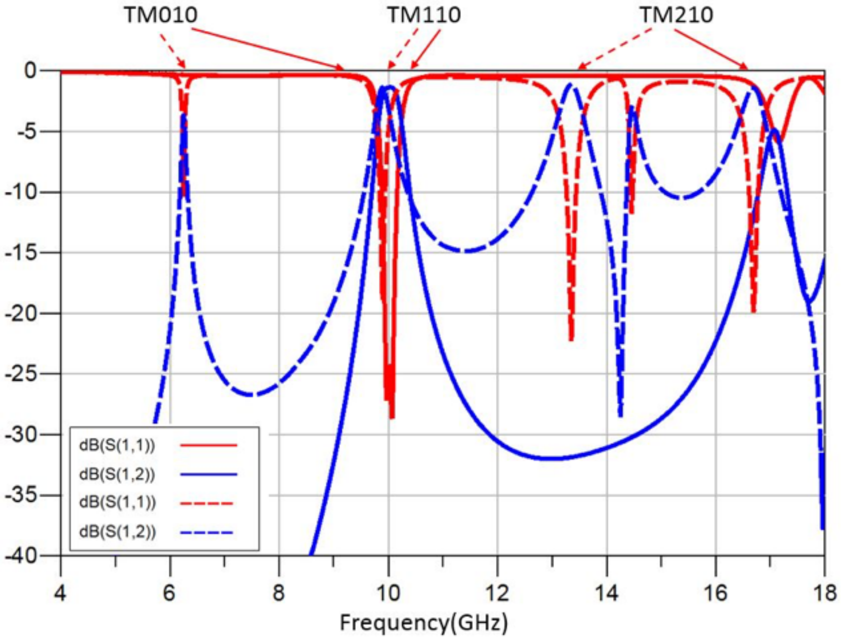

Figure 2.20: Simulated return loss and insertion loss of the second-order dual-band filter.

shown in Fig. 2.19 for comparison. Also, one can observe the low in-band insertion loss and high rejection at the higher passband and the frequencies in between the two bands. As the two modes have similar field configuration, when they form the passband the coupling scheme can be constructed with similar external quality factors (Fig. 2.21).

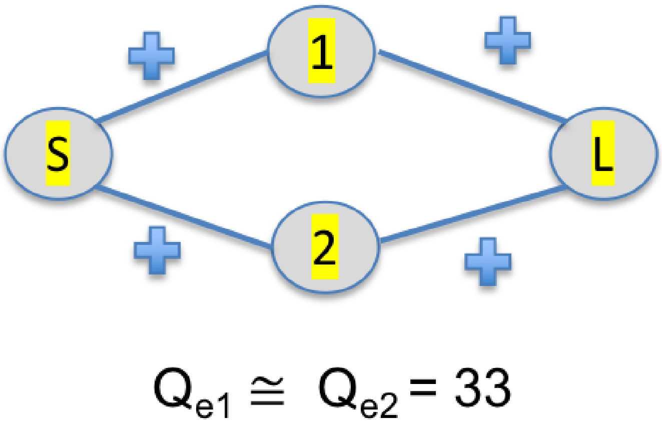

Figure 2.21: Coupling scheme of the dual resonance cavity based filter.

2.3.3 Dual-band Filter

Once the two cavity resonators are designed separately, they are put together to form a dual-band filter. This is accomplished by extending the 50 Ω microstrip feeding lines for both the cavities to meet at T-junctions. By controlling the length of the feeding line of each cavity, we can make one branch appear open at the T-junction for the other band's operating frequency (Fig. 2.22). For example, at 10 GHz, the input signal will only go through the bigger cavity while the smaller cavity (14 GHz) branch will appear as open. By using this method, the cavities could be made to operate in a manner identical to what they would do if placed separately. The simulated S-parameter response for the dual-band filter of Fig.2.22 is shown in Fig. 2.23. Some of the useful parameters are:

- Central frequency of the two passbands: 10.02 GHz and 14.02 GHz respectively
- Fractional bandwidths of the two bands: 4.1% for both the bands
- In-band insertion loss for the two bands: 1.8 dB (10 GHz) and 1.9 dB (14 GHz)
- Rejection of the frequencies in between the two bands: around 50 dB

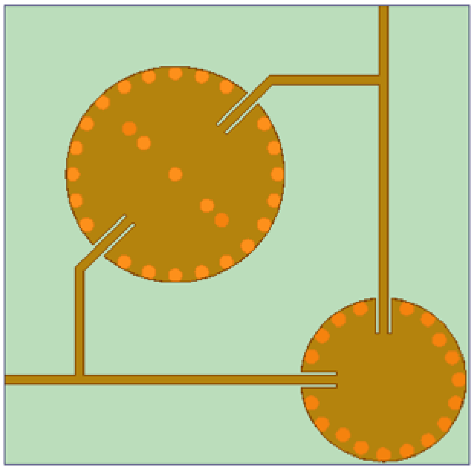

Figure 2.22: Schematic of the dual-band filter with the extended microstrip lines.

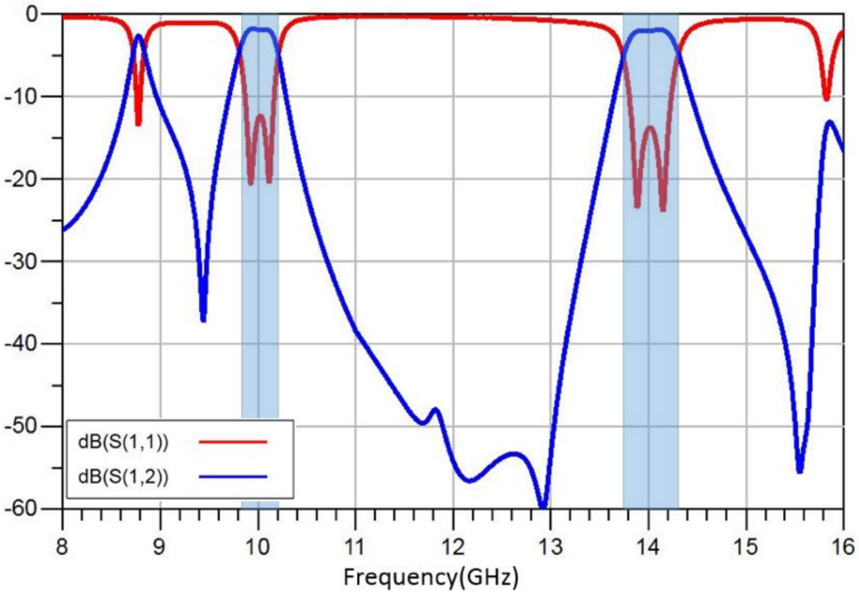

Figure 2.23: Schematic of the dual-band filter with the extended microstrip lines.

2.3.4 Fabrication and Measurement of Unpackaged Filter

The designed filter was first fabricated without the package to validate the performance. The via holes of the SIW cavities were drilled by a LPKF Protomat machine to ensure the precision of their positions. The holes were then filled by the cylindrical copper pins and soldered with the copper claddings on the top and bottom of the substrate to enhance the connection. The input and the output microstrip-line ports were soldered directly to SMA

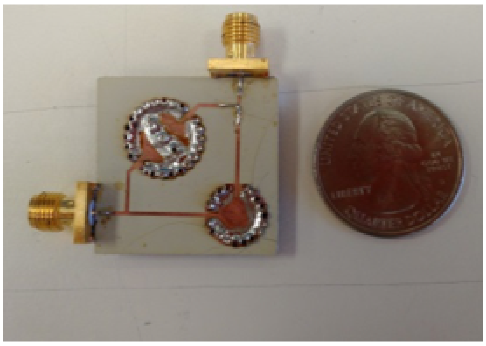

Figure 2.24: Photograph of the unpackaged filter.

connectors. Fig. 2.24 shows the photo of the unpackaged filter.

The measured insertion loss is plotted and compared with simulation in Fig. 2.25. The center frequencies of the two passbands are 9.92 GHz and 13.9 GHz, which are both slightly lower than simulation, possibly because the substrate is inevitably dispersive and its actual dielectric constant at high frequencies is larger than the nominal value provided by the vendor. The 3-dB fractional bandwidths are 3.9% for the 10 GHz passband and 5.7% for 14 GHz. The second passband is wider than simulation, possibly due to the poor contact between the vias and the copper claddings on the substrate, which introduces inaccurate perturbation and splits the two modes further. The lowest insertion losses are 2.6 dB for the 10 GHz passband and 3.7 dB for 14 GHz. They are worse than simulation as the transition from the SMA connector to the microstrip line adds some loss. The rejection between the two passbands is over 24 dB. With better fabrication process especially for the vias, we believe we would achieve closer performance to simulation.

2.3.5 Packaged Filter

The SMA connectors were then removed from the unpackaged prototype, before it was inserted into the StratEdge package provided by the competition committee. The backside ground plane of the substrate was attached to the package ground pad with EPO-TEK H20E silver epoxy adhesive . The input and output ports on the substrate were bonded to their each closest signal pin on the package sidewall by a 20 mil × 50 mil × 10 mil gold

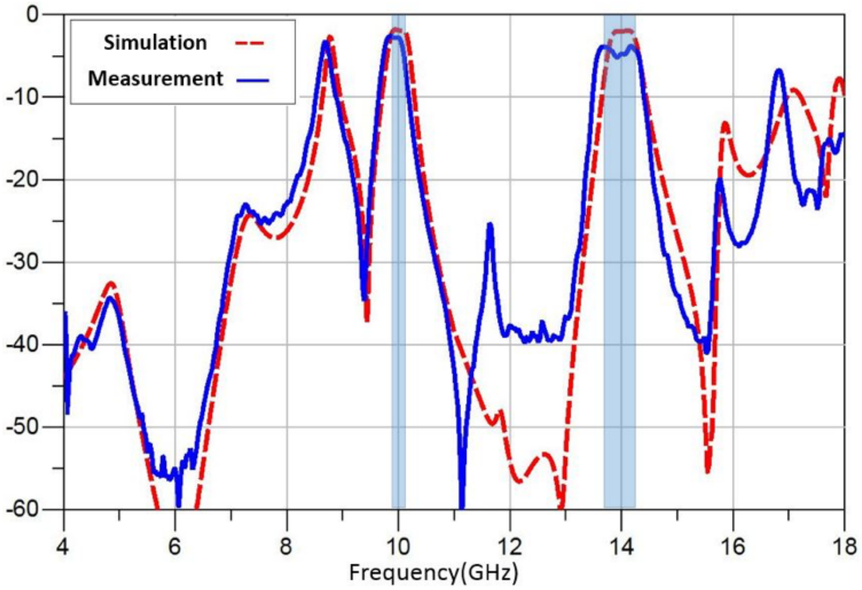

Figure 2.25: Comparison between simulated and measured insertion loss of the unpackaged filter.

Figure 2.26: Photograph of the packaged filter (a) without and (b) with copper cover..

pad to minimize the loss. Outside the package, each signal pin was inserted to the inner conductor socket of a no-pin SMA connector. The outer conductor of the SMA connector was then attached closely to the package sidewall with silver epoxy adhesive, as the no-pin SMA connector we had was made of steel which was not easy to solder. To further enhance the mechanical firmness, an additional layer of nonconductive epoxy adhesive was applied to connect the SMA connector and the package, which was harder to break than silver epoxy adhesive. Fig. 2.26 (a) shows the photo of the packaged filter, which was finally covered by a copper tape (Fig.2.26 (b)) during the measurement.

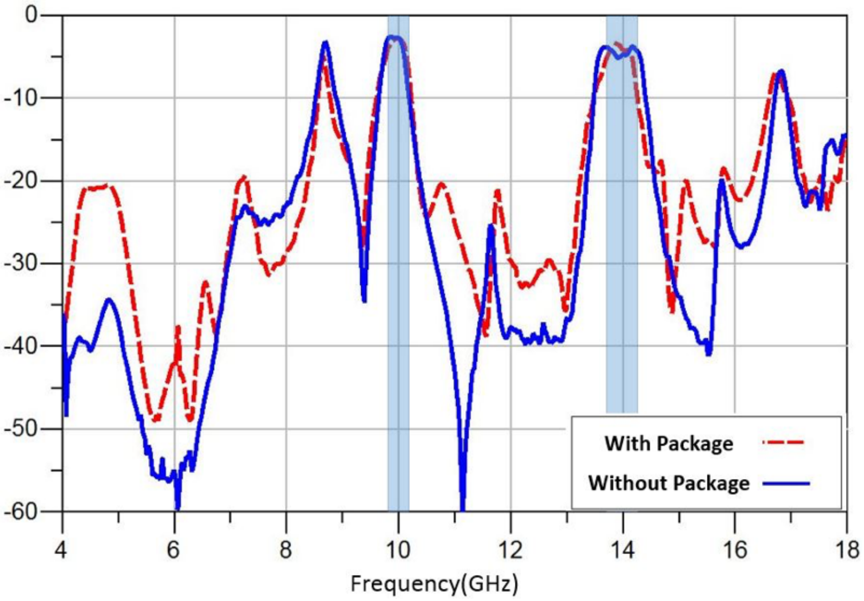

Figure 2.27: Measured insertion loss of the unpackaged and the packaged filter.

The measured insertion loss of the packaged filter is compared with the result of the unpackaged one in Fig. 2.27. The center frequencies of the two passbands are intact because of the same cavities. The insertion losses are 2.9 dB and 3.5 dB for the 10 GHz and 14 GHz passbands, respectively. The 3-dB fractional bandwidths are 4.3% for the 10 GHz passband and 4.2% for 14 GHz. The package introduces additional mismatch and improves or degrades the insertion losses and the bandwidths. The rejection between the two passbands is over 21 dB, generally less than the unpackaged filter because the copper-tape cover reflects back the little radiation from the microstrip line.

The performances of the filter in simulation and measurement are summarized in Table 2.1 and Table 2.2. Note that the center frequencies and the bandwidths are very close to the specifications. To approach the outstanding simulated results, the fabrication process of our design could be improved. To accurately account for the package effect, we could include the package in simulation to optimize the design. It should be mentioned here that the deterioration in the measured results vis-a-vis simulations can be coreected on identifying the precise cause for the deviation. A circuit model for the two resonance cavities can aid in this regard; a transmission line model for synthesizing SIW filters is shown in the next section.

Table 2.1: Performance Summary of the Dual-Band Filter

	Band 1			Band2		
	Central Freq (GHz)	BW	Insertion Loss (dB)	Central Freq (GHz)	BW	Insertion Loss (dB)
Sim.	10	4.1%	1.8	14	4.1%	1.92
Meas. w/o package	9.92	3.92%	2.64	13.92	5.7%	3.7
Meas. with package	9.94	4.3%	2.89	13.9	4.2%	3.53

Table 2.2: Maximum Inter-Band Rejection Levels

	Rejection Level (dB)
Sim.	>40
Meas. w/o package	>20
Meas. with package	>21

2.4 Planar Resonator Embedded Substrate Integrated Waveguide (SIW) Cavity Filter [21]

In this work, a pair of additional transmission poles are introduced in the frequency response of a two cavity SIW filter by embedding two capacitor-loaded planar resonators in the filter structure. The SIW cavities operate in TM_{110} mode, resulting in compact size of the filter. Methodology for determining the couplings between the resonators and their external quality factors is presented in the paper. It is also shown that the planar resonators are responsible

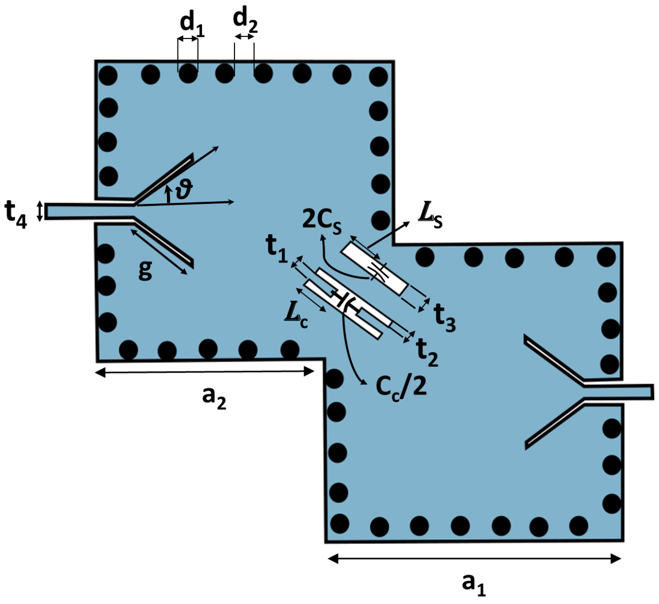

Figure 2.28: Schematic of fourth order SIW cavity filter. Relevant dimensions are : $a_1 = 28.4$ mm, $a_2 = 21.9$ mm, $g = 7$ mm, $\theta = 40.53°$, $d_1 = 1.6$ mm, $d_2 = 2$ mm, $L_c = 2.9$ mm, $L_s = 2.2$ mm, $t_1 = 0.5$ mm, $t_2 = 0.6$ mm, $t_3 = 1$ mm, $t_4 = 1.2$ mm.

for introducing a pair of TZs in the frequency response of the filter. As would be shown in the following sections, each TZ is produced by interfernce of signal propogating through a planar resonator with that of the SIW resonators.

2.4.1 Theory

Shown in Fig. 2.28 is the schematic of the proposed SIW cavity filter implemented on a 1.28 mm thick Rogers/ Duroid 6010 ($\epsilon_r = 10.2$, $\tan\delta = 0.0023$) board. The filter is designed to operate at 2.35 GHz with a fractional bandwidth (FBW) of 5% and a pair of TZs on either side of the passband (at 2.25 GHz and 2.45 GHz). It consists of a capacitor ($C_c/2$) loaded coplanar waveguide (CPW) and a capacitor ($2C_s$) loaded slotline (SL) embedded in a two cavity SIW structure.

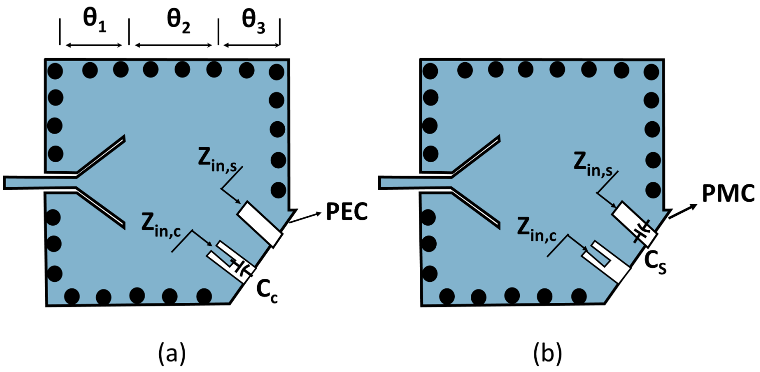

Figure 2.29: Schematic of the (a) odd-mode and (b) even mode equivalent structures of the fourth order filter. The electrical lengths at 2.45 GHz are: $\theta_1 = 55°$, $\theta_2 = 91°$, $\theta_3 = 34°$.

2.4.1.1 Resonance Mechanism

$$f_{SIW} = \frac{c_0}{\sqrt{2\epsilon_r a_1}} \tag{2.9}$$

where c_0 is the speed of light in vacuum. On the other hand, odd and even mode analysis is used to determine the resonance frequencies of the CPW and SL structures (Fig. 2.29). The condition for resonance of CPW and SL structures is given as $Z_{in,\{c,s\}} = 0$, where $Z_{in,c}$ and $Z_{in,s}$ are the input impedances of the CPW and SL structures respectively. The above condition can be simplified for the resonance frequency of CPW structure in odd mode (f_c) and that of SL in even mode (f_s) as :

$$f_{\{c,s\}} = \left(2\pi Z_{0,\{c,s\}} C_{\{c,s\}} \tan\left(\beta_{\{c,s\}} L_{\{c,s\}}\right)\right)^{-1} \tag{2.10}$$

where $\beta_{\{c,s\}}$ and $Z_{0\{c,s\}}$ represent the phase constant and characteristic impedances of CPW and SL structures respectively. Fig. 2.30 shows the variation of the two frequencies with C_c and C_s, where a commercial EM solver (Ansys HFSS) has been used for simulations. Likewise, the even mode frequency of CPW resonator and the odd mode frequency of SL resonator can be given by solving the equations:

$$\beta_c L_c = \pi/2 \tag{2.11}$$

$$\beta_s L_s = \pi \tag{2.12}$$

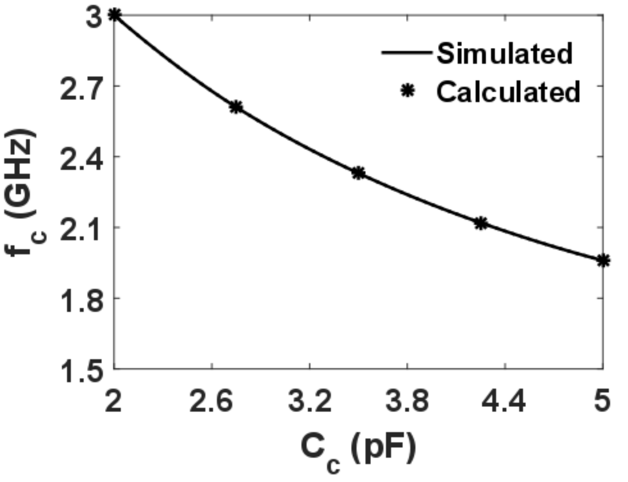

(a)

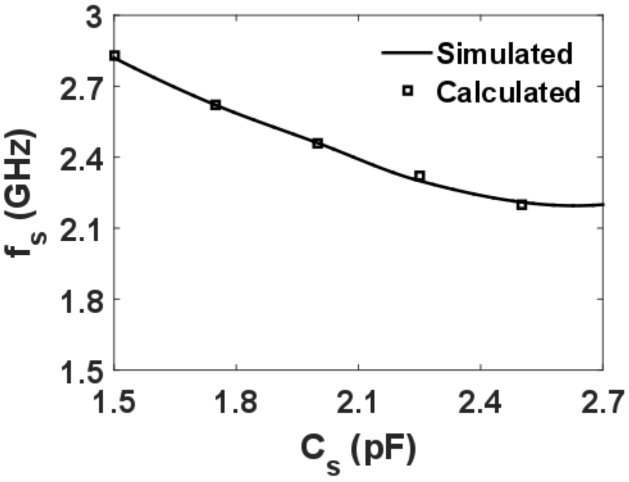

(b)

Figure 2.30: Variation of (a) f_c with C_c (b) f_s with C_s. For calculations, $Z_{0,c}$ = 53.64 Ω and $Z_{0,s}$ =177.48 Ω. Effective relative permittivities are 6.06 and 5.8 for CPW and SL structures respectively.

To analyze the effect of planar resonators on SIW cavity, TEM transmission line models are created for the odd and even mode equivalents of the filter as shown in Figs. 2.31(a) and 2.31(b) respectively. The phase constants of various elements in TEM line model correspond to that in the physical structure at the resonance frequency of SIW cavity, i.e. 2.45 GHz (from (2.9)). Inductors $\widetilde{L_e}$ and -$\widetilde{L_o}$ are added to the TEM line models to account for frequency

(a) (b)

Figure 2.31: TEM transmission line models for (a) odd-mode equivalent and (b) even-mode equivalent of the filter. Parameter values: $\widetilde{L_o}$ =0.0004 nH, $\widetilde{L_e}$ = 0.0025 nH, $Z_{o,SIW}$ = 0.46 Ω. It should be noted the lengths of planar resonators,L_s and L_c are along the diagonal of the structure. The corresponding electrical lengths are given by $\beta_s L_s$ and $\beta_c L_c$.

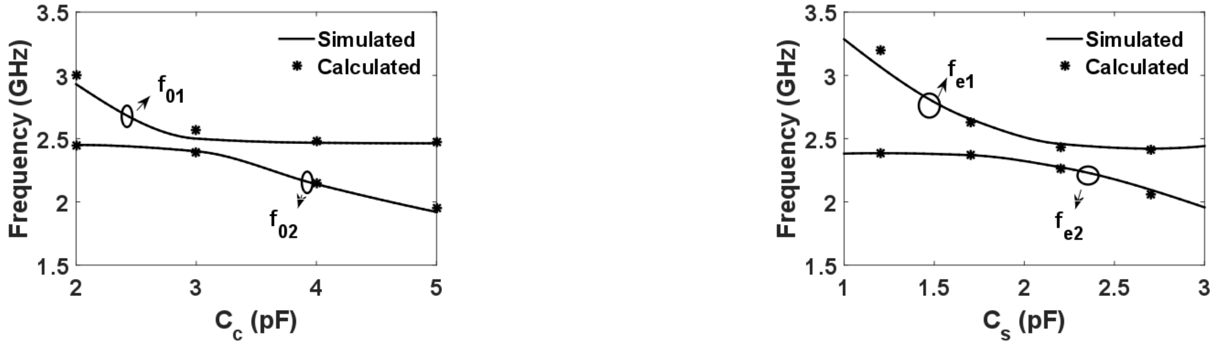

(a) (b)

Figure 2.32: Variation of resonant frequencies of (a) odd-mode structure with C_c and (b) even mode structure with C_s.

shifts of SIW cavity in even and odd modes respectively. It should be noted that the negative value of $\widetilde{L_o}$ is not a real quantity, but used to convey the phase characteristics as in the case of immitance inverters [1]. The resonance frequencies of the structures in Fig. 2.29 can then be extracted by the condition $Im\{Z_{left} + Z_{right}\} = 0$. The frequency responses of the two equivalent structures are shown in Fig. 2.32. Due to inability of uniquely defining characteristic impedance, $Z_{0,SIW}$ of the SIW structure, the value is obtained by curve fitting

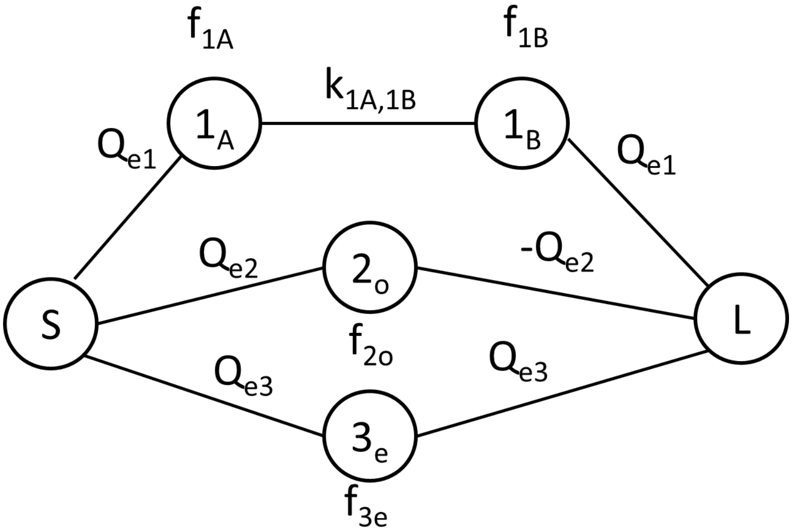

Figure 2.33: Coupling scheme of the fourth order filter. Parameter values: $f_{1A} = f_{1B} = 2.35$ GHz, $f_{2o} = 2.26$ GHz, $f_{3e} = 2.4$ GHz, $k_{1A,1B} =$ -0.026, $Q_{e1} = 27.61$, Q_{e2} =180.2 and Q_{e3} =147.06.

the response of either the even or odd mode equivalent structure.

2.4.1.2 Filter Prototype Development

Coupling scheme of the fourth order filter is shown in Fig. 2.33. Here, resonators 1_A and 1_B represent the two SIW cavities. The odd mode CPW resonance is represented by the node 2_o, while the even mode slot resonance is represented by 3_e. From (2.11) and (2.12), the CPW even mode frequency and the SL odd mode frequency can be found as 10.5 GHz and 31.1 GHz respectively. These resonances do not contribute to the filter network and are not considered in the coupling scheme.

2.4.1.2.1 Transmission Zeroes

The TZs are generated by the interference at the load in Fig. 2.33 of the signal propagating through planar resonators with that propagating through the SIW resonators. For verifying, resonators 2_o and 3_e are detuned from the filter operating frequency as shown in Fig. 2.34

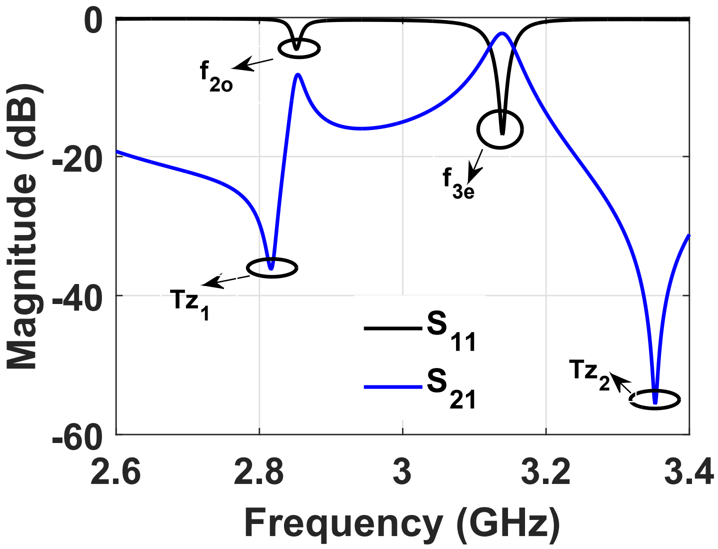

Figure 2.34: Coupling scheme of the fourth order filter. Parameter values: $f_{1A} = f_{1B} = 2.35$ GHz, $f_{2o} = 2.26$ GHz, $f_{3e} = 2.4$ GHz, $k_{1A,1B}$ = -0.026, $Q_{e1} = 27.61$, Q_{e2} =180.2 and Q_{e3} =147.06.

by changing the value of chip capacitors.

2.4.1.2.2 Coupling Factor

For generating a quasi-elliptic response, the resonance frequencies of planar resonators are chosen from Fig. 2.32, such that $f_{2o} = f_{o2}$ and $f_{3e} = f_{e1}$. Also, the values of chip capacitors are chosen such that frequencies f_{o2} and f_{e1} are placed on the lower and upper edges of the passband respectively. This has been done so that the TZ associated with resonator 2_o (TZ_1) is placed on the lower side of then passband, while that associated with 3_e (TZ_2) is placed on the upper side of the passband. On the other hand, the remaining two inner frequencies, f_{o1} and f_{e2} are assigned as the resonance frequencies of the SIW cavities in odd and even modes respectively. Doing so accounts for the effect of planar resonators on SIW cavities in Fig. 2.33. Thus, the coupling coefficient between resonators 1_A and 1_B is given as :

$$k_{1A,1B} = \frac{{f_{e2}}^2 - {f_{o1}}^2}{{f_{e2}}^2 + {f_{o1}}^2} \tag{2.13}$$

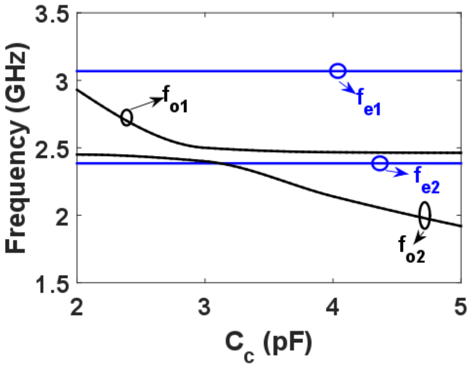

Figure 2.35: Variation of resonance frequencies of the filter with C_c. C_s is held fixed at 1.2 pF.

It can be verified from Fig. 2.35 that the frequency response of even-mode equivalent structure is independant of C_c , implying that there is no coupling between the resonators 2_e and 3_o.

2.4.1.2.3 External Quality Factor

The external quality factors of the resonators can be calculated as

$$Q_e = \frac{2\pi f \tau}{4} \tag{2.14}$$

where τ is the group delay of the loaded resonator at its resonant frequency f. Resonators 2_o and 3_e are detuned from operating frequency for calculation of Q_{e1}. On the other hand, schematics of Fig. 2.29 (a) and Fig. 2.29 (b) are used to calculate Q_{e2} and Q_{e3}, respectively.

Regular filter design method following [22] can be used to design the filter with the extracted coupling coefficient and Q_e. Minor optimization is needed to compensate for frequency shifts due to external loading.

2.4.2 Measurements

Chip capacitors are used to realize $C_c/2$ = 1.6 pF (AVX 04021J1R6P4STR\500) and $2C_s$ = 3.7 pF (Murata GJM1555C1H3R7BB01D) for implementing the fourth order filter. The

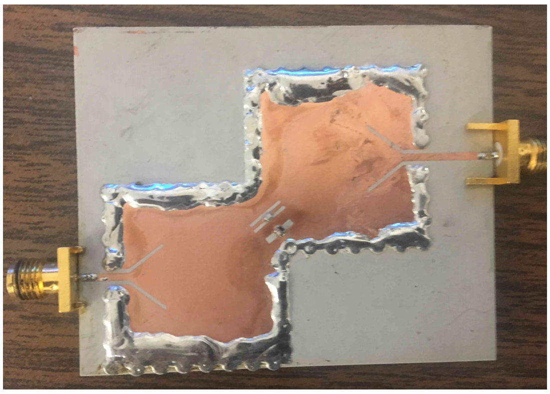

Figure 2.36: Photograph of the fabricated filter.

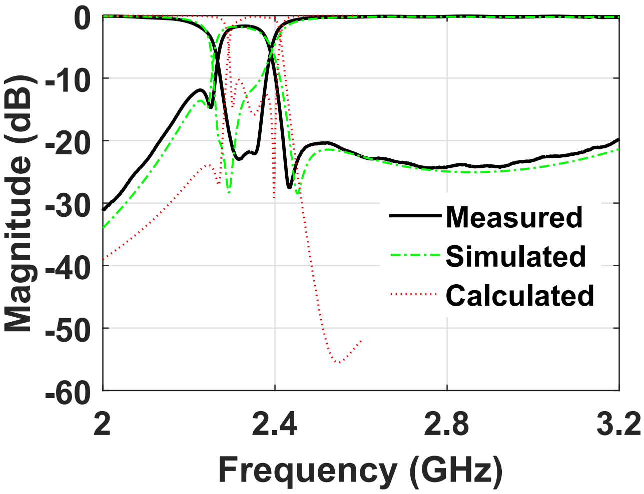

Figure 2.37: Frequency response of the fourth order filter.

photograph of the fabricated filter is shown in Fig. 3.29. Simulated, measured and calculated results of the filter are shown in Fig. 2.37. The filter operates at 2.35 GHz with a mid-band insertion-loss of 1.65 dB, including the connector loss. However, the measured bandwidth is reduced to 4.65 % compared to the simulated bandwidth of 5 % due to fabrication inaccuracies. This leads to an estimated unloaded quality factor of 245. The in-band return loss is lower than -20 dB. Moreover, a quasi-elliptic filter response is produced due to presence of TZs on either side of the passband (i.e. at 2.25 GHz and 2.43 GHz). The filter occupies an area of 1517 mm^2 on a single layer board.As a result, high degree of compactness with low loss is achieved by the proposed filter. The comparison of the proposed filter with SIW filters in literatyre is shown in Table 2.3. It can be clearly seen that the mixed planar

Table 2.3: Comparison of Filters in SIW Technology

	f_o **(GHz)**	**FBW (%)**	**Insertion Loss (dB)**	**Volume** $(\lambda_g{}^3)$	**TZs**	**Qu**
[22]	20	4	0.9	0.0965	1B, 1A	505
[23]	5.1	4.2	2.05	0.0418	1B, 1A	225
[24]	5.25	5.2	1.5	0.0531	1B, 2A	240
[25]	5.75	1.8*	3.6	0.0949	1B, 1A	225
This Work	2.35	4.65	1.65	0.0377	1B, 1A	245

[*] Note: f_0 : Center Frequency; B:Below, A:Above; *1-dB BW

resonator/SIW topology affords good quality factors with compact size of the filter.

CHAPTER 3

Microwave Filtering Antennas

3.1 General Concepts

Most RF-front end systems have an antenna cascaded right after the bandpass filter to filter out the unwanted frequencies. The filters and antennas often serve as independant body subjects [26, 5], designed independantly and connected, generally, through a 50 Ω line. However, there are certain drawbacks associated with this approach

- The 50 Ω line needs to be long enough to ensure minimal field coupling between the filter and the antenna elements. Moreover, in a single-channel case, the filter and antenna generally operate on concurrent frequencies, with the express goal of achieving filtering and radiation respectively – thereby increasing the resonator redundancies. Both the above mentioned factors lead to an increased footprint of antenna/filter combine.
- Due to nature of microwave filter synthesis, the filter response is flatter in the band and sharper at the band-edges compared to the response of an antenna. If the antenna and filter are designed for coincidental passbands, it leads to degradation of filter response characteristics at the band-edges of the antenna [27].
- Planar resonant antennas are inherently narrowband in nature due to small radiation resistance [28]. Methods of widening the bandwidths of these antennas include perturbations in the signal plane [29] or in the ground plane [30] of the antenna. However, the perturbations result in loss of antenna gain. By using antenna element as a resonator of filtering network, larger bandwidth with the gain almost similar to that of the original element can be obtained [31].

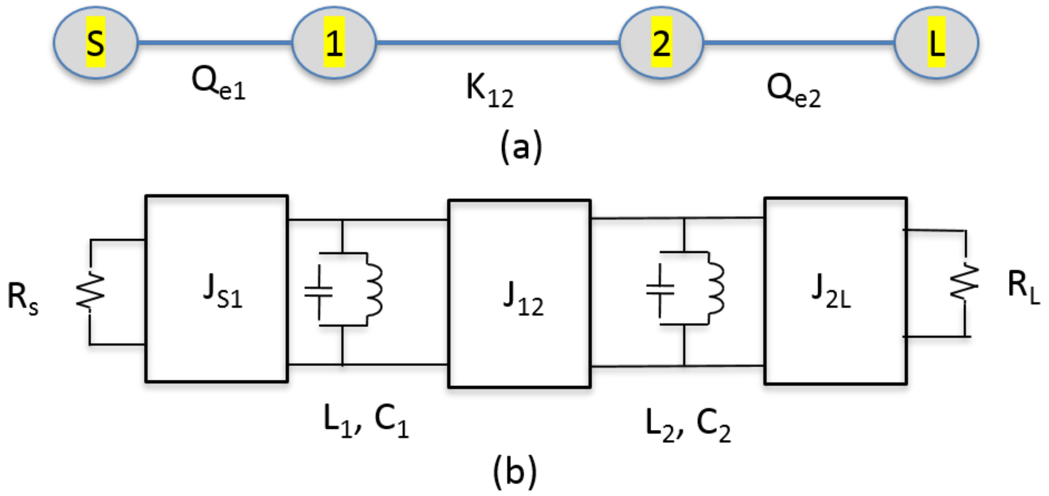

Figure 3.1: (a) Coupling matrix representation and (b) Network representation of a two pole filter.

A remedy to these problems is the integrated filter/ antenna also known as filtering antenna.There are two general approaches to implement filtering antennas.

- Antenna Fusion Approach: This approach involves integrating additional resonators in the antenna structure to get multiple resonances [32, 33]. The approach is similar to implementation of multiple mode wideband antennas [29], with the difference being the focus on gain response.
- Integration of Frequency Selective Surfaces in Horns: Metallic films with [34] or without [35] substrates are placed on the open ends of horn antennas. The aim is to achieve a polarizing capability over a narrowband of the horn operational range.
- Filter Synthesis Approach: The most comprehensive approach to filtering antenna development, with antenna element considered as a terminating resonator in the multi-resonator filter network [27, 31].

Neither of the first two approaches answer the basic question of filter development i.e. how to control the order of the filter. This puts into question the scalability of the two approaches.

The filter synthesis approach introduced by Lin and Jung [31] necessarily focuses on

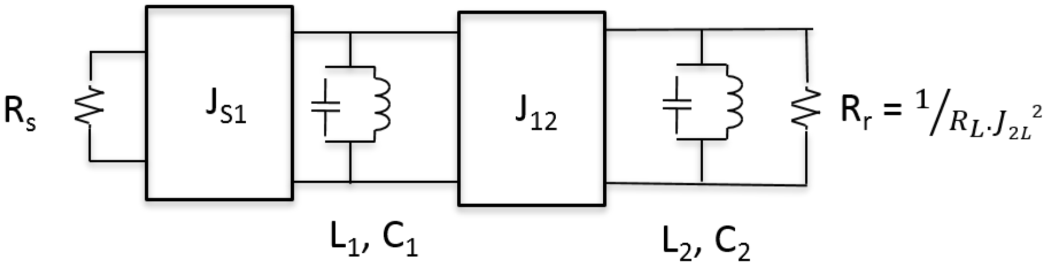

Figure 3.2: Equivalent network representation of the two pole filter, with the second resonator a low Q radiating element.

the network synthesis approach (Fig. 3.1), rather than the coupling matrix approach as introdeced in Chapter 2. The parameters of one representation can be directly translated to another over a narrowband [4]. The reason for failure of coupling matrix extraction can be deciphered if the second resonator in Fig. 3.1 (a) is considered as the radiating element (antenna). In that case, it is difficult to assign the external quality factor Q_{e2} as there is no direct way for calculating loaded bandwidth or group delay of the antenna resonator. However, if one considers the network model in Fig. 3.1 (b), an equivalent model as shown in Fig. 3.2 can be constructed, which allows for extraction of the antenna resistance R_r using an EM simulator. This is an extra-step because unlike with the coupling scheme parameters, the parameters of netwok approach can not be direct extracted from the EM simulator. The process involves tedious parameter conversion and additional dembedding to extract the rasistance due to radiation of the antenna element. Moreover, the dembedding becomes an ardent task if the antenna resonator is not of a regular shape.

It has been shown in the previous chapter that TZs are caused due to cross-coupling between non-adjacent nodes in the filter scheme. However, in all the three designs presented in the previous chapter, the cross coupling paths had resonators embedded in both of the cross-coupling paths. That is, if the TZ locations have to be adjusted, so will change the location of transmission poles of the filter, which would affect both its operating frequency and bandwidth. On the other hand, having direct source to load coupling in parallel with main filtering line (Fig.3.3) can allow control of TZs independant of passband characteristics

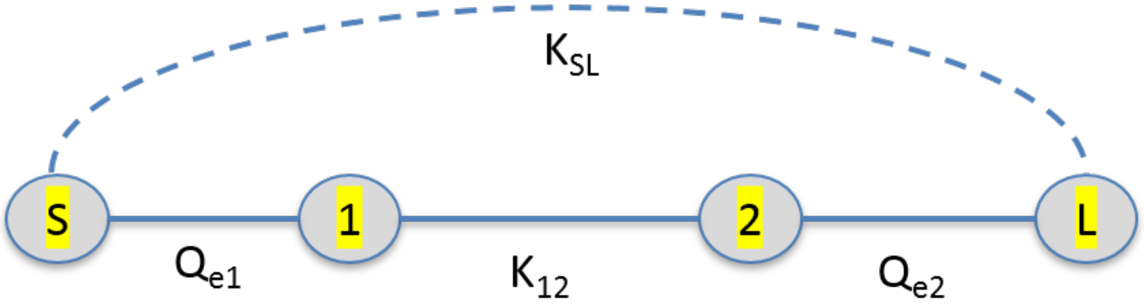

Figure 3.3: Equivalent network representation of the two pole filter, with direct source-load coupling.

[36, 37], provided the field coupling through the direct source to load path is weak compared to the main filter path.

Continuing with the theme of TZs, the maximum number of TZs that can be synthesized using a n–resonator network is also n [1]. Out-of-path resonators can be added like that in bandstop filters [38], but the process results in larger filter size.

It should also be mentioned while the filter synthesis will give the exact S_{11} of the filtering antenna, the Realized Gain characteristics will only mirror S_{21} characteristics in a single observation direction and therefore, is an approximation at best. This can be further explained by looking at the analogy between the two:

For filters,

$$S_{21}{}^2 = (1 - |S_{21}|^2) \times e \tag{3.1}$$

where e is the material efficiency of the filter and also encompasses losses due to multi-path destructive interference. For filtering antennas,

$$Realized\ Gain\ (\theta, \phi) = (1 - |S_{21}|^2) \times e \times D\ (\theta, \phi) \tag{3.2}$$

where D is the directivity of the antenna element.

The absence of an additional directional term, D in (3.1) compared to (3.2) makes the dichotomy between Realized Gain and S_{21} evident. Also, important to note is that unlike filters, TZs can be produced in the frequency response of the filtering antennas both due to to inter-resonator coupling and directivity nulling.

Finally, it is important to develop single layer topologies for all planar circuits as multilayer technologies may be height constrained in many technologies [39], limiting the quality factor of constituent resonators.

3.2 Half-Mode Cavity Based Planar Filtering Antenna with Controllable Transmission Zeroes [40]

Implementing filtering antennas in substrate integrated waveguide (SIW) technology provides high-Q selective nature of *3*-D cavities in planar form [41, 42, 43]. Most of the SIW planar designs presented in the literature have multilayer integration of SIW cavities with radiating elements [41, 42]. In [43], a single layer Chebyeshev SIW filtering antenna with cavity backed slot antenna as the radiating element has been developed. Also, as described in [42, 43], the feeding microstrip lines also produce spurious radiation and affect the out-of-band characteristics of the filter. Metallic shields have been used in [42, 43] to remove the unintended effect of microstrip lines.

In this work, a half-mode SIW (HMSIW) cavity resonator [44] is used in conjunction with a conventional SIW cavity to obtain a single-layer two-pole filtering antenna design. Electric coupling is introduced by using a coplanar waveguide (CPW) to couple the two cavities [45]. Source-load coupling is introduced by using a radiating microstrip line to feed the antenna. By doing so, a transmission zero (TZ) is generated on either side of the passband leading to a quasi-elliptic frequency response. The position of TZs is then controlled by varying the feeding microstrip line length and terminating it by a coaxial line. The proposed HMSIW-integrated filtering antenna offers compact size and low cross-polarization, while maintaining reasonable antenna gain and efficiency values. The design methodology along with simulation and measured results of the proposed filtering antenna are presented in the following sections.

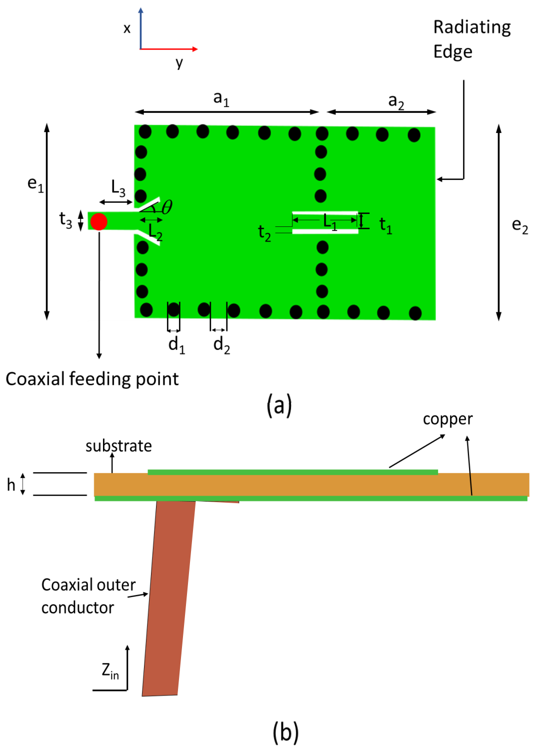

Figure 3.4: (a) Schematic of the proposed filtering antenna (top view) with $a_1 = 26$ mm, $a_2 = 13$mm, $e_1 = 26$mm, $e_2 = 26$mm, $d_1 = d_2 = 1.6$ mm, $L_1 = 8.5$ mm, $L_2 = 2.8$ mm, $L_3 = 4.5$ mm, $\theta = 45$, $t_1 = 2$ mm, $t_2 = 0.5$ mm, $t_3 = 2.4$ mm. (b) Side view with $h = 0.79$mm.

3.2.1 Theory

Shown in Fig. 3.4 is the schematic of proposed filtering antenna. The antenna is designed for Rogers RT/Duroid 5880 board with $\epsilon_r = 2.2$ and tan $\delta = 0.001$. The filtering antenna is composed of two resonators — a high Q conventional SIW cavity and a radiating HMSIW cavity — connected in an in-line topology through a coplanar waveguide (CPW) transmission line. The filtering antenna is fed by a 50 Ω microstrip line, which in turn, is fed by a 50 Ω coaxial line to minimize the reflection losses between the two.

The HMSIW cavity resonator is formed by removing half of the conventional SIW cavity through its symmetrical plane such that the TM_{110} field pattern in the remaining cavity is largely unaltered [44]. The open plane discontinuity, however, functions as a radiating discontinuity and is used in this design to provide terminating resistance to the two pole

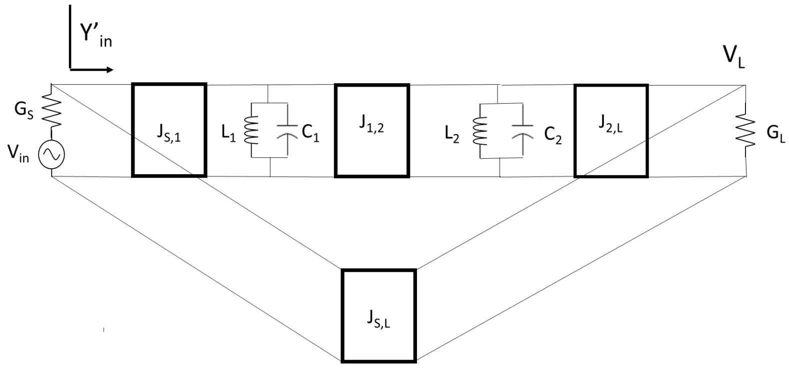

Figure 3.5: Lumped element model of the filter network. Parameters: C_1 = 3.884 pF, C_2 = 1.966 pF, L_1 = 0.2149 nH, L_2 = 0.425 nH, G_s = 0.02 S, G_L = 0.01 S, $J_{S,1}$ = 8.114 x 10^{-3} S, $J_{2,L}$ = 3.697 x 10^{-3} S, $J_{1,2}$ = 2.22 x 10^{-3} S, $J_{S,L}$ = - 8.5 x 10^{-4} S.

filtering network. Moreover, compared to a conventional SIW cavity, the HMSIW cavity provides a size shrinkage of more than 50%.

The lumped-element equivalent circuit for a two stage in-line filter is shown in Fig. 3.5, where the LC tank circuits are used to model the two cavity resonators and admittance inverters are used to model the interstage couplings. The direct source-to-load coulping due to radiation from feeding network is modeled by the admittance inverter, $J_{S,L}$.

The lumped-element circuit model can be obtained by optimization methods shown in literature [4]. In this paper, the lumped-element prototype is built for a 2.8% bandwidth filter with an in-band ripple level of 0.15 dB, operating frequency as 5.5 GHz and a TZ on either side of the passband (@5.25 GHz and @5.8 GHz) (Fig. 3.5).

Response of the circuit model is shown in Fig. 3.6. Once the lumped-element values of the equivalent circuit are obtained, the constituent elements of the filtering antenna can be designed.

3.2.1.1 Conventional SIW Cavity

The resonance frequency of the conventional SIW resonator in the TM_{110} mode can be obtained as:

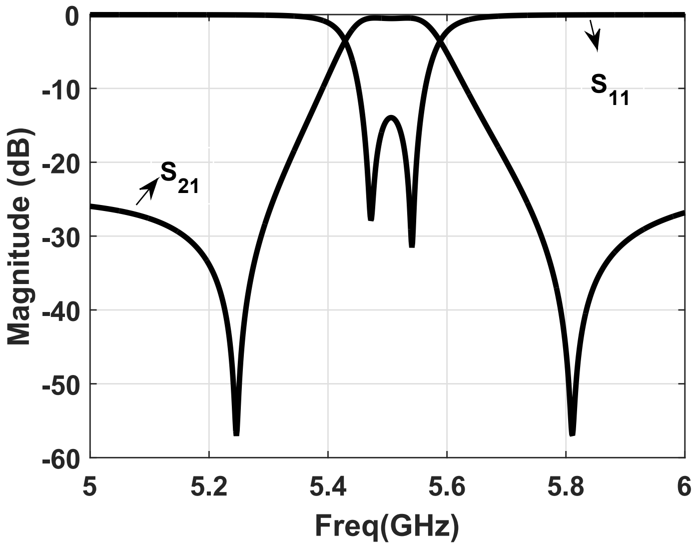

Figure 3.6: Frequency response of the circuit model.

$$f_1 = \frac{c_0}{2\sqrt{\epsilon_r}}\sqrt{(\frac{1}{a_1})^2 + (\frac{1}{e_1})^2} \tag{3.3}$$

where c_0 is the speed of light in air. The values of capacitances C_1 and inductance L_1 can be calculated as [4]:

$$C_1 = \frac{\epsilon_0\epsilon_r a_1 e_1}{4h}, L_1 = \frac{1}{(2\pi f_1)^2 C_1} \tag{3.4}$$

3.2.1.2 HMSIW Cavity

In case of the HMSIW cavity resonator, the radiating edge presents a lumped capacitance ΔC due to fringing fields and a lumped resistance, R_r to account for the far-field radiation. Although R_r and ΔC can be evaluated using analytical methods [46], an EM-solver (Ansys HFSS) has been used to de-embed the values for the proposed design. The variation of R_r and normalized susceptance of waveguide aperture B/Y_0 (where $B = 2\pi f\Delta C$ and Y_0 is the characteristic admittance of the HMSIW) with the parameters h and e_2 is shown in Fig. 3.7.

The resonance frequency of HMSIW cavity, f_2 can be evaluated from the transmission-

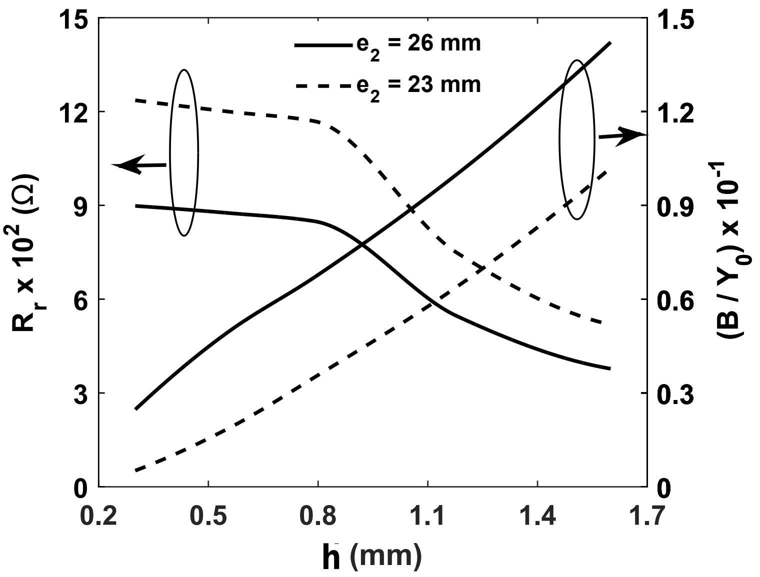

Figure 3.7: Variation of resistance R_r and normalized susceptance of the HMSIW cavity resonator.

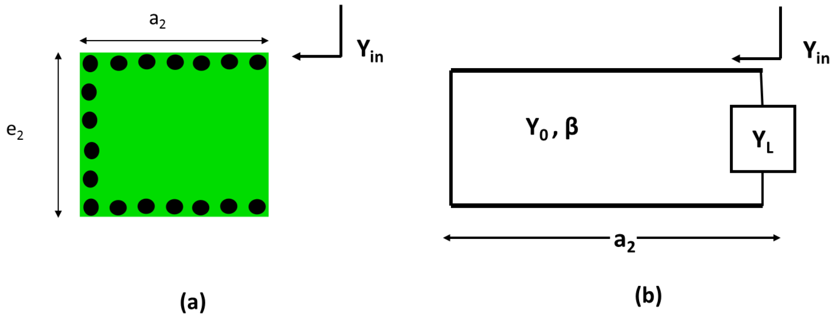

Figure 3.8: (a) HMSIW cavity resonator and (b) its transmission-line model with $Y_L = 1/R_r + jB$.

line model (Fig. 3.8) by using the condition $Im\{Y_{in}\} = 0$, where

$$\frac{Im\{Y_{in}\}}{Y_o} = \frac{B}{Y_0} - \cot(\beta a_2) \tag{3.5}$$

with β as guided wave phase constant for the dominant mode of HMSIW, given by:

$$\beta = \sqrt{(\frac{2\pi f_2}{c_0})^2\epsilon_r - (\frac{\pi}{e_2})^2} \tag{3.6}$$

Fig. 3.9 shows the variation of resonance frequency of HMSIW cavity resonator. It can

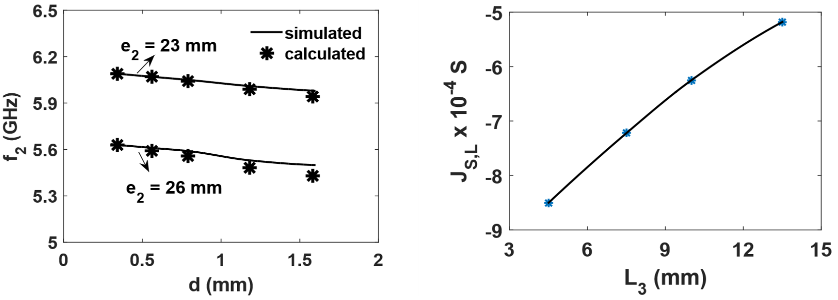

(a) (b)

Figure 3.9: Variation of (a) resonance frequency of the HMSIW cavity. (b) the admittance inverter $J_{S,L}$

be seen that the calculated f_2 values closely follow the simulated ones.

For calculating the values of L_2 and C_2, the HMSIW cavity is first terminated by a magnetic wall at its open end. The corresponding resonator lumped element values are given as:

$$C_2{}' = \frac{\epsilon_0 \epsilon_r a_2 e_2}{4h}, \quad L_2{}' = \frac{1}{(2\pi f_2{}')^2 C_2{}'} \tag{3.7}$$

where $f_2{}'$ is the resonance frequency of HMSIW cavity terminated by magnetic wall and can be calculated using (3.5) with $B = 0$. As there is no radiation from the HMSIW in this condition, $R_r = \infty$. Now, if on removing the magnetic wall, $B/Y_0 << 1$, then the slight change in resonance frequency of HMSIW cavity resonator , $f_2{}'$ - f_2 , can be attributed to ΔC with the inductive component of tank resonator remaining constant, i.e.

$$C_2 = C_2{}' + \Delta C, \quad L_2 = L_2{}' \tag{3.8}$$

with $\Delta C = ((f_2{}' - f_2)/f_2{}') \times 2C_2{}'$. Also, from Fig. 3.5 and Fig. 3.8, it can be deduced that

$$1/R_r = J_{2,L}{}^2/G_L \tag{3.9}$$

3.2.2 Interstage Couplings

The values of admittance inverter parameters can be related to external quality factor Q_e and coupling coefficient k as

$$J_{S,1} = \sqrt{\frac{b_1 G_S}{Q_e}} \tag{3.10}$$

$$J_{1,2} = k\sqrt{b_1 b_2} \tag{3.11}$$

The values of $J_{S,L}$ can be controlled by changing the length of microstrip feed-line (Fig. 3.9 (b)).

The transmission poles are introduced in the frequency response of filtering antenna when circuit admittance (Y'_{in}) seen from the source in Fig. 3.5 meets the condition, $Y'_{in} = G_S$

If the value of source-to-load coupling is small, its effect on the passband characteristics is not significant and as such, the pole locations can be controlled by changing the cavity resonator susceptances or the interstage couplings.

On the other hand, the TZs are generated when voltage on load, $V_L = 0$. This condition requires the signal propagating through the cavity resonators to be cancelled at the load by that propagating directly from source-to-load through $J_{S,L}$ in Fig. 3.5. From an EM point of view, this means cancellation of far-field radiation from HMSIW edge in the broadside direction by that produced by the microstrip feed-line and the its inset in the SIW cavity, leading to broadside directivity, $D = 0$. The positive sign of interstage coupling in Fig. 3.5 refers to electric coupling, which is achieved by using a CPW line to couple the two cavities as shown in Fig. 3.4. As such, the positions of TZs can be altered by varying the microstrip feed-line length (Fig. 3.10) and terminating it with a non-radiating coaxial line. This requires the radiating microstrip line to be considered a part of antenna. It can also be noticed in Fig . 3.10 that the TZs vanish if a metallic shield is kept on top of the feeding microstrip line and its inset (Fig. 3.11). Presence of a shield prohibits radiation from microstrip line, thereby removing the source-to-load coupling.

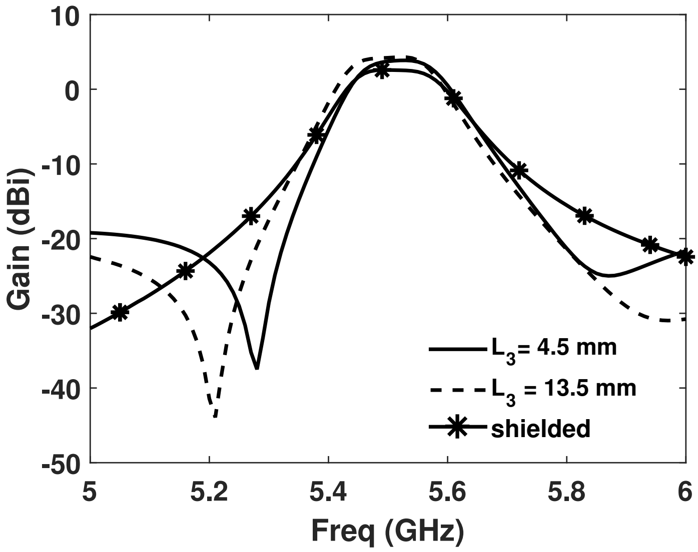

Figure 3.10: TZ variation with microstrip feed line length.

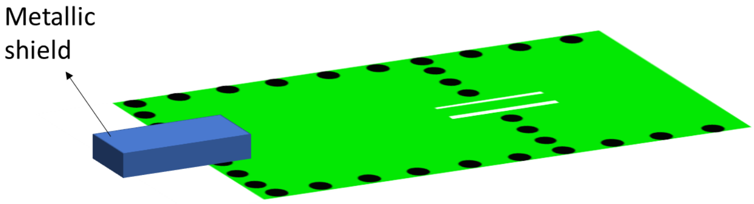

Figure 3.11: Use of metallic shield to suppress the spurious radiation from microstrip feed line. Shown in the figure is only the shield and the top metal plane of the filtering antenna.

3.2.3 Measurements

The reflection coefficient of the filtering antenna is measured using an Agilent 8510C Vector Network Analyzer while the gain values are measured in a spherical near-field chamber at the University of Hong Kong. Simulated and measured responses of the filtering antenna compare closely with each other (Fig. 3.12). The antenna is centered at 5.5 GHz with a gain of 4.3 dBi in both simulation and measurement curves. On the other hand, bandwidth of the measured structure is reduced to 2.6% from the intended 2.8% due to fabrication tolerances. The measured reflection coefficient is less than -20 dB at the operating frequency. Moreover, the filtering antenna shows the presence of two transmission zeroes (TZs), leading to a

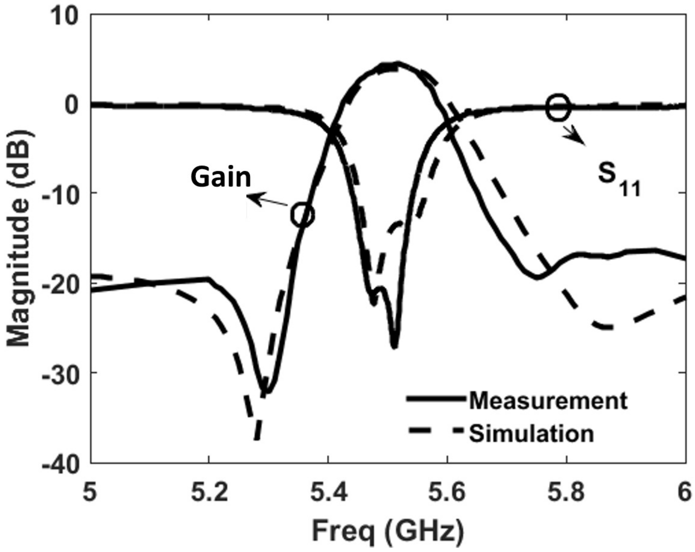

Figure 3.12: Frequency response of the filtering antenna in broadside direction. Here, Gain $= (1 - |S_{11}|^2)$ x e x D.

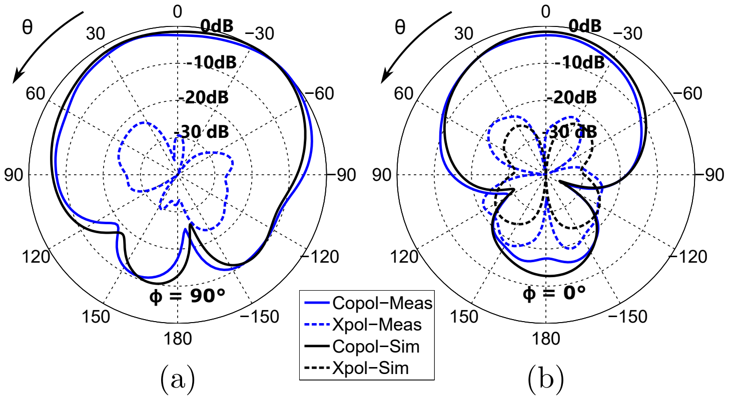

Figure 3.13: (a) E-plane and (b) H-plane radiation patterns of the filtering antenna at 5.5 GHz. Note that copol/xpol components follow Ludwig's 3rd definition of cross-polarization

quasi-elliptic response.

Finally, the radiation patterns of the filtering antenna at the operating frequency are shown in Fig.3.13. It can be seen that the cross-polarized gain level remains 15 dB below the co-polarized gain in both E- and H-planes. The simulated and measured directivities at the broadside are 5.15 dBi and 4.8 dBi respectively. These directivities along with the values of

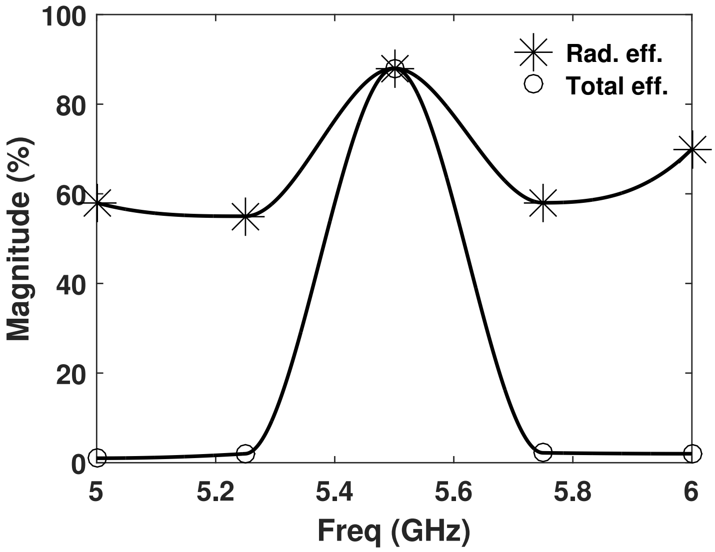

Figure 3.14: Variation of radiation efficiency with frequency. Here, total efficiency, $e_T = (1 - |S_{11}|^2)$ x e.

Table 3.1: Comparison of Filtering Antennas

Filtering Antenna	**Volume (Area x Height)**	**Max. Gain (dBi)**	**Bandwidth** (%)	**S/L**	e(%)
[41]	$0.16\lambda_g{}^3$	4.9	3	No	86^v
[42]	Prepreg size not given	6.79	1.56	No	N/A
[43]	$0.25\lambda_g{}^3$	6.2	6.8	No	89^v
[27]	$0.004\lambda_g{}^3$	≈2.5*	≈ 4	No	N/A
Proposed design	$0.017\lambda_g{}^3$	4.3*	2.6	Yes	89

* Note: * : Broadside Gain, v : Simulated, S/L : Source-Load Coupling

gains mentioned previously, lead to measured and simulated radiation efficiencies, e of 89% and 82% for the filtering antenna (including the microstrip feed-line). Fig. 3.14 shows the variation of measured efficiency with frequency. Finally, the proposed design is compared with other published filtering antennas in Table 3.1, which brings out the twin advantages of controllable TZs and compact size of the proposed design.

3.3 Low-Profile Dual-Band Filtering Antenna Using Common Planar Cavity [47]

To the best of authors' knowledge, no dual-band SIW filtering antenna has been reported in literature. This is quite contrary to recent trends in wireless communications, which require multi-band communications. Adding to that, the filtering antennas require large roll-off values if the two bands are closed to each other. The requirement leads to larger number of resonators in filter network, thereby increasing both the material loss and spatial footprint of the device. An alternative solution lies in using orthogonally polarized antennas for the two closely-spaced bands leading to inter-band isolation. Dual-band filtering antennas with orthogonal polarizations in the two bands have been reported in literature [48, 34]. The microstrip design [48] is based on multi-layer technology, which increases both the height and fabrication cost of the filtering antenna. Moreover, [34] is based on horn antenna technology.

In this paper, a single-layer dual-band SIW filtering antenna with orthogonal polarizations in the two bands is presented. A dual-mode rectangular SIW cavity, with two mutually orthogonal modes at the two band frequencies functions as a common high-Q cavity for the two bands, miniaturizing the antenna size. The two modes of the SIW cavity couple to two slot-loaded (SL) cavities, respectively through evanescant mode waveguides. In turn, the two SL cavities radiate with reasonable gains in mutually orthogonal polarizations. Synthesis method for the development of filtering antenna along with simulated and measured results is presented in the following sections.

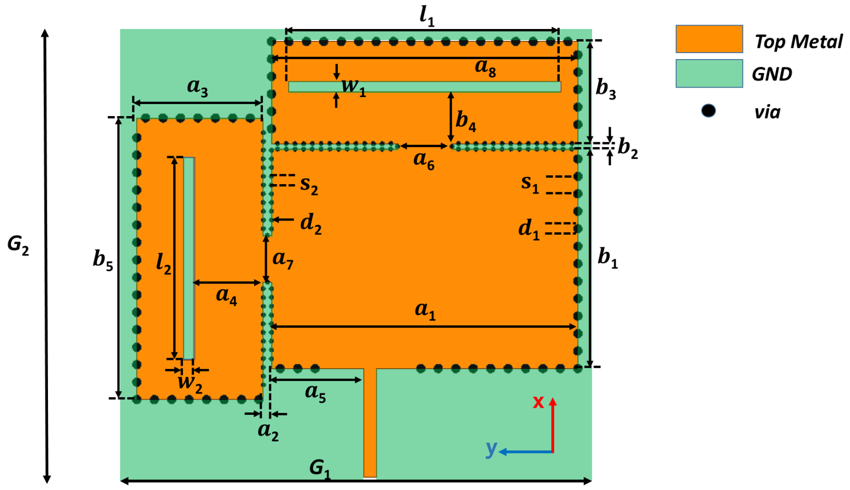

Figure 3.15: Schematic of the proposed design. The dimensions are all in mm: $a_1 = 56.2$, $a_2 = 1.5$, $a_3 = 23.2$, $a_4 = 12.6$, $a_5 = 16.9$, $a_6 = 10$, $a_7 = 9$, $a_8 = 56.2$, $b_1 = 40.2$, $b_2 = 1$, $b_3 = 18.7$, $b_4 = 9.45$, $b_5 = 51.6$, $l_1 = 50$, $l_2 = 37$, $w_1 = 2$, $w_2 = 2$, $G_1 = G_2 = 9$. The large vias have diameter $d_1 = 1.6$ with spacing $s_1 = 3.2$; while the small vias have diameter $d_2 = 0.8$ with spacing $s_2 = 1.6$.

3.3.1 Design

Schematic of the proposed dual-band two pole filtering antenna is shown in Fig. 3.15. The filtering antenna is implemented on a metal-backed Rogers RT/Duroid 5880 board ($\varepsilon_r = 2.2$, $\tan\delta = 0.001$) with thickness, $t = 0.79\,\text{mm}$. The design consists of a common rectangular SIW cavity coupled to two SL cavities through evanescent mode waveguides. The common cavity operates on the orthogonal TM_{120} and TM_{210} modes at low and high frequency bands respectively. The off-center microstrip feeding line allows both modes to be excited. The radiating slots of the two SL cavities provide the load resistance to each two pole filtering network. The SL cavities are placed in orthogonal manner to obtain polarization isolation in the two bands.

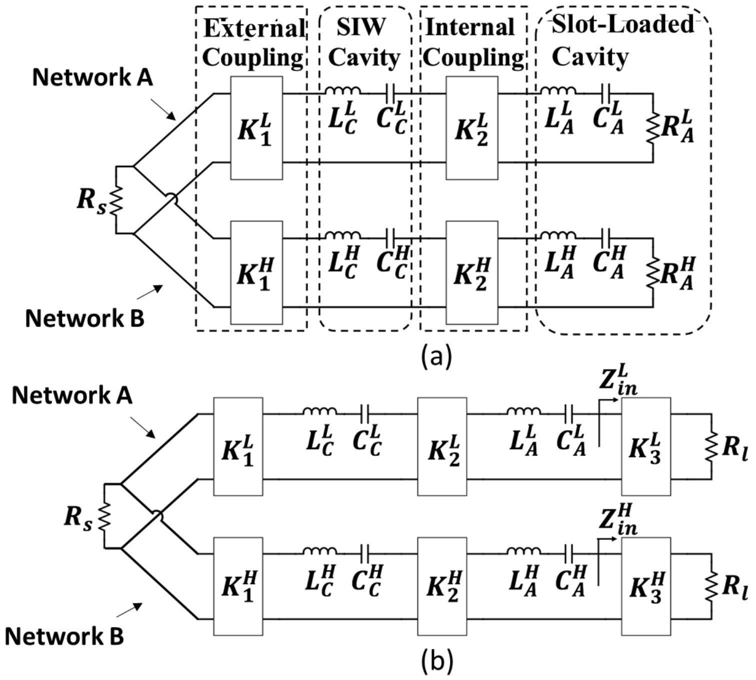

Figure 3.16: Equivalent circuit model loaded with (a) slot resistance R_A and (b) standard 50 Ω R_l, where an additional impedance inverter K_3 is inserted, such that $Z_{in} = R_A$. Parameters: $R_S = R_l = 50\,\Omega$, $K_1^L = 1.24\,\Omega$, $L_C^L = 0.1\,\text{nH}$, $C_C^L = 13.3\,\text{pF}$, $K_2^L = 0.36\,\Omega$, $L_A^L = 3.60\,\text{nH}$, $C_A^L = 0.382\,\text{pF}$, $K_3^L = 12.2\,\Omega$; $K_1^H = 1.72\,\Omega$, $L_C^H = 0.074\,\text{nH}$, $C_C^H = 13.3\,\text{pF}$, $K_2^H = 0.57\,\Omega$, $L_A^H = 2.02\,\text{nH}$, $C_A^H = 0.489\,\text{pF}$, $K_3^H = 14.1\,\Omega$.

3.3.1.1 Equivalent Circuit Model

The lumped-element circuit model of the device is given in Fig. 3.16. Network A and Network B represent the high and low band respectively. A common source is shared by the two networks since the structure has only one feeding line. Coupling between the two networks has been ignored as the modes for the high band and the low band are orthogonal in the common cavity. The series LC-resonators represent the cavity resonances, while the impedance inverters represent interstage couplings.

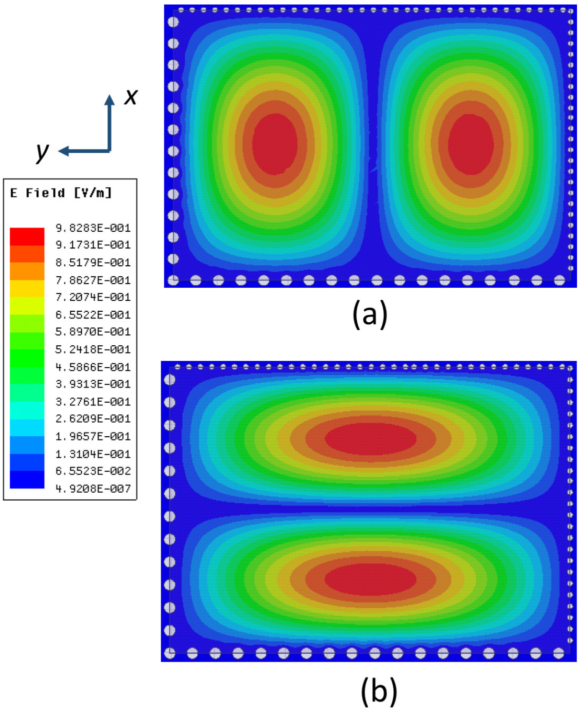

Figure 3.17: Electric field distribution of rectangular SIW cavity at (a) 4.3 GHz (TM_{120} mode) (b) 5.1 GHz (TM_{210} mode)

3.3.1.2 Full-wave Analysis

3.3.1.2.1 Dual-mode SIW Cavity

The resonant frequency f_C of TM_{mn0} mode in a rectangular SIW cavity can be found by

$$f_C = f_{mn0} = \frac{c_0}{2\sqrt{\varepsilon_r}}\sqrt{\left(\frac{m}{b_1}\right)^2 + \left(\frac{n}{a_1}\right)^2} \tag{3.12}$$

where c_0 is the speed of the light in vacuum. The TM_{120} and TM_{210} modes are mutually orthogonal to each other with their field distributions shown in Fig 3.17. As shown in Fig. 3.18, the frequency ratio between the two modes can be controlled through the cavity aspect ratio a_1/b_1 (from 3.12). The cavity can be modeled as a series LC-resonator with values given by [49].

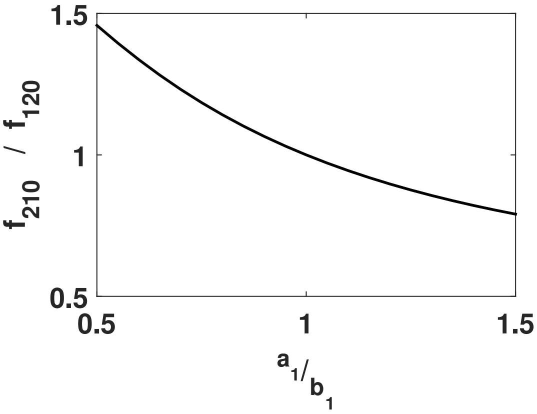

Figure 3.18: Variation of the frequency ratio f_{210}/f_{120} with aspect ratio $a_1/b_1$of the dual-mode SIW cavity.

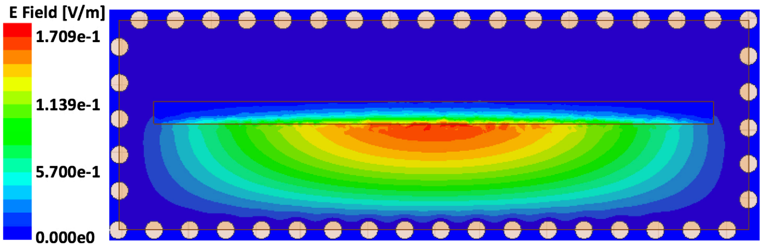

Figure 3.19: Electric field distribution in the SL cavity for high band at 5.1 GHz. The field distributions at f_A^H in the SL cavity are obtained through eigenmode solver in Ansys HFSS.

3.3.1.2.2 SL cavity

Only the method for synthesis of high-band SL cavity is discussed here, the SL cavity for lower band can be designed using the same methodology.

The slot-loaded radiating cavity behaves as a perturbed half-mode TM_{110} resonator, in a manner similar to the one presented in [50]. The non-resonant radiation slot divides the radiating cavity into two half-mode cavity parts and only the lower (larger) cavity is used as a radiating element at the operating frequency (Fig. 3.19).

The resonance frequency of the SL cavity, ${f_A}^H$, can be controlled through the cavity's dimensions (Fig. 3.20). It can be observed that values of ${f_A}^H$ are very close to f_{HMS} —

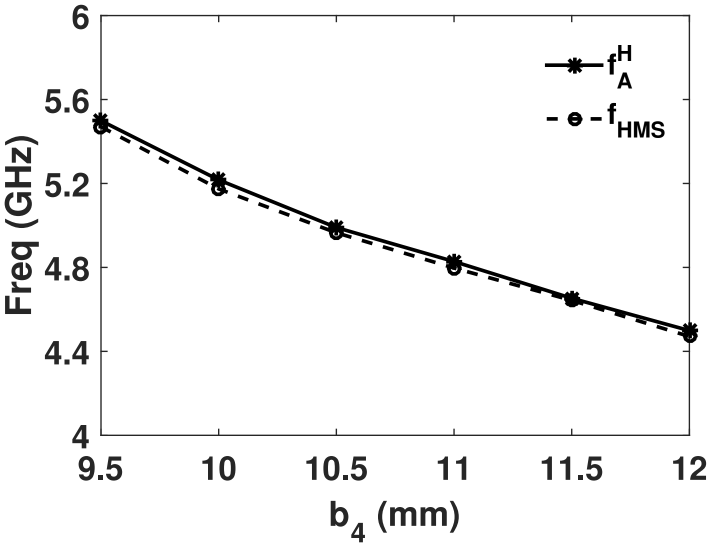

Figure 3.20: Variation of SL and HMSIW cavity resonance frequencies with b_4. The dimensions of HMSIW cavity are $a_1 \times b_4$ in x-y plane.

the resonance frequency of corresponding HMSIW cavity, confirming the similar nature of operation of the two cavities. Moreover, the value of f_{HMS} can be approximated as

$$f_{HMS} = f_A^H = \frac{c_0}{2\sqrt{\varepsilon_r}}\sqrt{\left(\frac{1}{2b_4}\right)^2 + \left(\frac{1}{a_8}\right)^2} \tag{3.13}$$

Although the analytical solution of the slot impedance has been thoroughly studied by Oliner in [51], in this work, the values of slot resistance ${R_A}^H$ are determined by de-embedding using a full wave EM solver (Ansys HFSS). Specifically, from Fig. 3.21 (a)

$${R_A}^H = Re\{Z_{in}|_{x=b_4}\} \tag{3.14}$$

The slot resistance ${R_A}^H$ can be controlled through the substrate thickness, t (Fig. 3.21 (b)).

The value of L_A^H and C_A^H can be extracted from the unloaded quality factor, Q_u^H as follows [4]:

$$L_A^H = \frac{Q_u^H R_A^H}{2\pi f_A^H} \tag{3.15}$$

$${C_A}^H = \frac{1}{\left(2\pi {f_A}^H\right)^2 {L_A}^H} \tag{3.16}$$

Q_u^H, in turn, can be extracted from the eigenmode solution of the SL cavity in EM simulator.

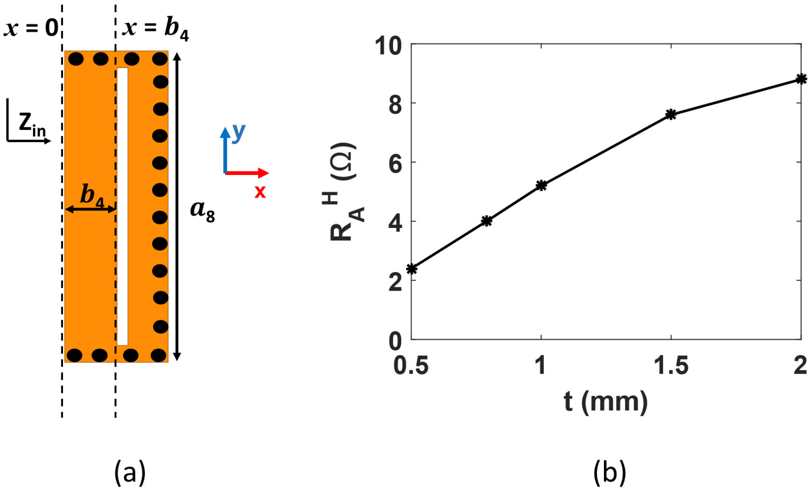

Figure 3.21: (a) Setup for extraction of slot resistance, ${R_A}^H$. (b) Variation of slot resistance, ${R_A}^H$ with substrate thickness, t.

3.3.1.2.3 External and Internal Couplings

The values of the inverter parameters K_1 and K_2 are related to the external quality factor Q_e and inter-resonator coupling coefficient k as:

$$Q_e = \frac{x_C R_S}{K_1^2} \tag{3.17}$$

$$k = \frac{K_2}{\sqrt{x_C x_A}} \tag{3.18}$$

where the slope parameter $x_{\{C,A\}} = 2\pi f_{\{C,A\}} \cdot L_{\{C,A\}}$. Both Q_e and k can be extracted by using the techniques presented in [1]. As shown in Fig 3.22, K_1 is determined by the location of the feeding line, while K_2 is controlled through the evanescent mode waveguides.

3.3.2 Measurement

The filtering antenna is realized by photolithography and chemical etching. LPKF Protomat C-40 milling machine is used to drill via-holes, which are in turn filled with copper rivets. The cross-sectional area of the ground plane is 0.72 cm^2 or 3.27 ${\lambda_g}^2$, where λ_g is the wavelength at f_L in the substrate. The reflection coefficient of the filtering antenna is measured using

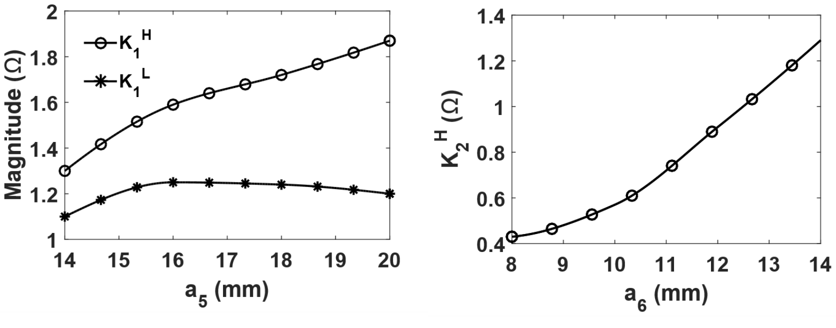

(a) (b)

Figure 3.22: Variation of (a) external couplings K_1^L and K_1^H with the position of feeding line (b) internal coupling ${K_2}^H$ with the width of evanescent mode waveguide.

Agilent 8510C VNA, while its gain is measured using a NSI 700 S near field chamber. The measured and simulated responses at the broadside of the filtering antenna, along with the calculated results of the lumped-element model are shown in Fig. 3.23. The X-polarized and Y-polarized gains are measured to show the co-polarized gains of the high band and low band channels, respectively. Reasonable agreement is achieved between simulated and measured results with slight frequency shifts due to the fabrication tolerances. The measured center frequency for low band is 4.3 GHz while that for high band is 5.02 GHz. The bandwidths for low band and high band are measured as 2.4% and 6% respectively, while the corresponding peak broadside gains are valued at 5.94 dBi and 6.45 dBi respectively. Isolation of more than 25 dB is achieved between the two operating bands. The large values of isolation are due to both the frequency selectivity of the filter and the orthogonal polarizations of the two radiating slots.

The measured radiation patterns of the filtering antenna correspond well with the simulated ones for both the bands as shown in Fig. 3.24. The cross-polarized levels are measured around 15 dB lower than the co-polarized ones for both the bands. Discrepancy between measured back-end radiation power levels and the simulated ones can be attributed to the mount of antenna, which blocks the backside radiation during measurement.

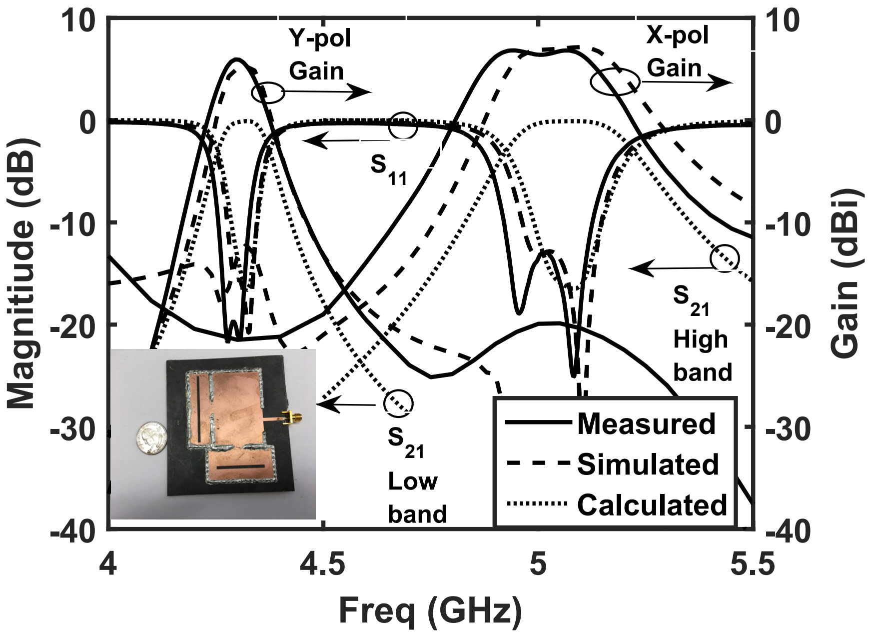

Figure 3.23: Frequency response of the filtering antenna. Gains are plotted at the broadside of the antenna. Shown in inset is the photograph of fabricated filtering antenna.

3.4 Low Profile Diplexing Filter/ Antenna Based on Common Radiating Cavity with Quasi-Elliptic Response [54]

Microwave diplexers and antennas are integral components of multiband communication systems, wherein they are independantly designed and connected through transmission lines. However, these structures have enlarged footprints and lead to inevitable transmission losses. Diplexing filtering antennas (DFAs) [55, 56, 57, 58, 59] have been proposed as integrated solutions for catering to dual-channel communication systems. Various DFAs designs aim to achieve sharp selectivity and minimum loss in two closely spaced channels with large inter-band isolation on a low profile (thin) substrate. Most of the DFAs [55, 56, 57, 59] presented in literature are multi-layer microstrip designs, which not only increase the fabrication cost and complexity of the circuit but also increase the losses produced in the filtering network. Integration of high-Q substrate integrated waveguide (SIW) diplexer with a wideband microstrip antenna was done in single-layer technology to reduce the losses in the filtering network [58].

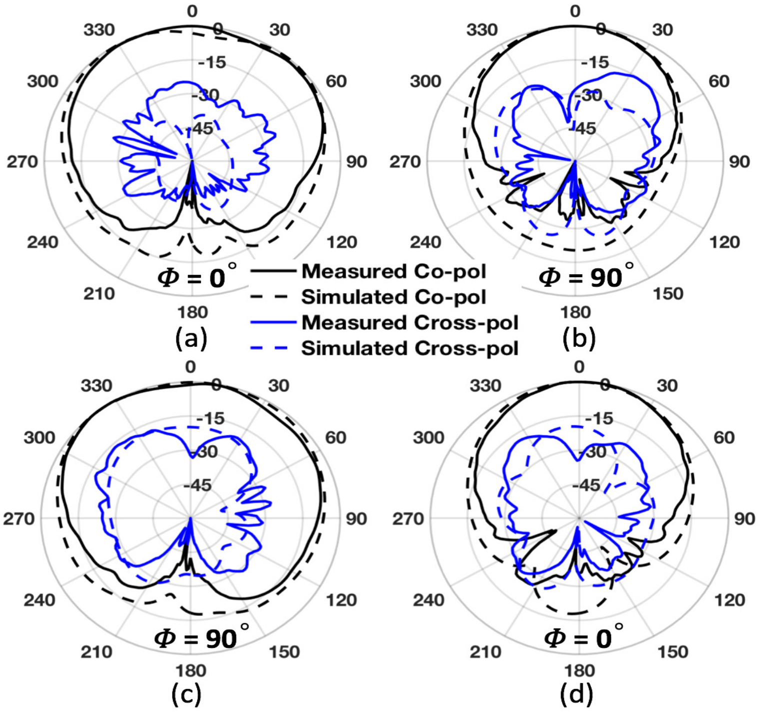

Figure 3.24: Radiation patterns for high band at 5.02 GHz in (a) x-z plane and (b) y-z plane; and for low band at 4.3 GHz in (c) y-z plane and (d) x-z plane.

However, the DFA required an additional dual-mode cavity to route the signals in the two channels, thereby increasing the size of the filtering antenna. Additionally, selectivity of the DFA can be increased by increasing the order of the DFA [56, 57, 58, 59], thereby increasing its form factor. However, selectivity can also be increased by placing a transmission zero (TZ) on either side of the passband, leading to a quasi-elliptic response [40].

In this work, a compact single-layer SIW DFA based on a common diplexing slot-loaded radiating cavity (SLC) is presented. Two-pole quasi elliptic filtering responses are obtained for both the channels. The transmission zeroes (TZs) are generated and controlled through source-load coupling [40], while the selectivity of channel responses is further enhanced by the usage of conventional SIW cavities. The proposed design provides a low inter-channel frequency ratio (FR), while maintaining reasonable inter-channel isolation between the two channels. Both channels have their main radiations polarized in the same direction with reasonable cross-pole discrimination (XPD) levels.

Table 3.2: Comparison of Filtering Antennas

	f_L / f_H (GHz)	BW (%)	Max Gain (dBi) @f_L / f_H	Tech.	Orth.	Ar ($\lambda_g{}^2$) x Height (λ_g)
[48]	2.45/ 5.8	4.5/ 3.8	-1.8/1.1	2 Layer microstrip	Yes	0.68× 0.015
[52]	3.6/ 5.2	4.1/ 3.8	7.5/8	2 Layer microstrip	No	N/A
[53]	1.9/ 2.6	2.1/ 1.9	6.7/7.3	1 Layer microstrip	No	0.71× 0.014
[34]	13.5/ 16.85	3.5/ 0.07	N/A	Horn	Yes	N/A
This Work	4.3/ 5.02	2.4/ 6	5.94* / 6.45*	1 Layer SIW	Yes	3.27× 0.016

* Note: * : Broadside Gain, BW : Bandwidth, Tech. : Technology, Orth. : Orthogonal Polarizations, Ar: Area

The synthesis of the DFA is achieved by using a fully coupling matrix method, i.e. the method does not require network synthesis approach for filtering antenna development. This allows for direct extraction of quantities from EM simulator. The method can be used for any filtering antenna topology with irregularly shaped resonators.

3.4.1 Design

Schematic of the proposed DFA is shown in Fig. 3.25. The DFA is implemented on a $t = 0.79$ mm thick Rogers RT/ Duroid 5880 board with $\epsilon_r = 2.2$ and $\tan\delta = 0.001$. Both channels of the DFA radiate through a self-diplexing SLC. The SLC is, in turn, coupled to two conventional SIW cavity resonators on its either end to improve selectivity and increase

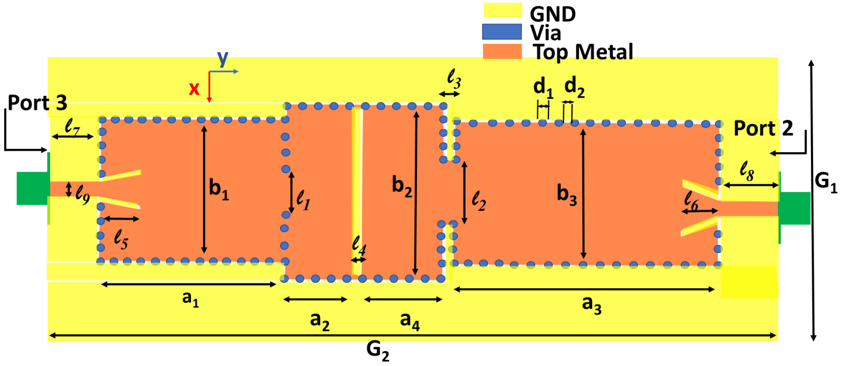

Figure 3.25: Schematic of the proposed DFA. All dimensions are all in mm: $a_1 = 28$, $a_2 = 10.5$, $a_3 = 40$, $a_4 = 12.4$, $b_1 = 21.7$, $b_2 = 26.4$, $b_3 = 21.7$, $l_1 = 8.1$, $l_2 = 10$, $l_3 = 1.5$, $l_4 = 0.9$, $l_5 = 6$, $l_6 = 5.5$, $l_7 = 5$, $l_8 = 8$, $l_9 = 2.54$, $G_1 = 35$, $G_2 = 107.5$, $d_1 = 0.8$, $d_2 = 1.6$.

bandwidth in both the channels of the DFA. Each of these conventional SIW cavities is fed by a 50 Ω radiating microstrip line, which is itself terminated by a 50 Ω non-radiating coaxial line. In Fig. 3.25, Port 1 is for feeding the upper channel, while Port 2 is for feeding the lower channel of the DFA.

The proposed design is an extension of the half-mode substrate integrated waveguide (HMSIW) cavity based single channel filtering antenna [40]. In [40], it is shown that TZs are created in the frequency response of the filtering antenna by using a radiating microstrip line to feed the antenna. The leakage from microstrip line and its inset in the conventional SIW cavity is out-of-phase with the main radiation from the HMSIW cavity and the two cancel out each other at the broadside of the filtering antenna to produce TZs. The leakage from microstrip line can be controlled through its length, thereby controlling the locations of TZs. The microstrip line, in turn, is fed by a non-radiating coaxial line to accurately control leakage from the feeding structure.

3.4.1.1 Coupling Scheme

Shown in Fig. 3.26 is the coupled-resonator topology of the DFA. The nodes C_U and C_L represent the conventional SIW cavities for upper and lower channels respectively, while the

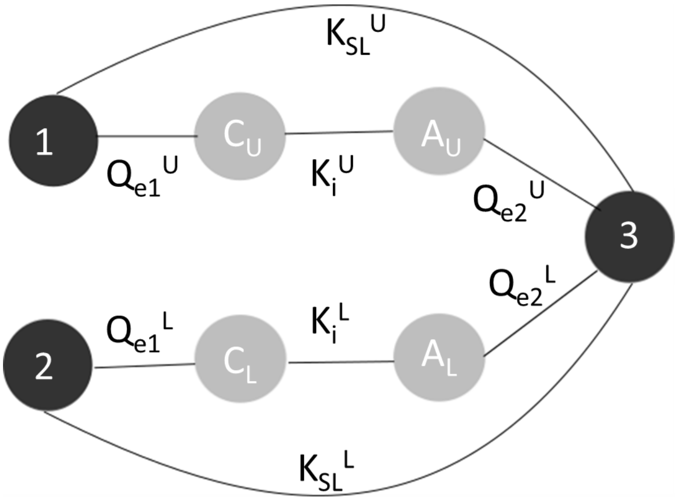

Figure 3.26: Coupling scheme of the DFA. Parameter values : $Q_{e1}^U = 37.2$, $Q_{e2}^U = 34.42$, K_i^U $=38.5 \times 10^{-3}$, $K_{SL}^U =$ - 2.3×10^{-3}, $Q_{e1}^L = 35.9$, $Q_{e2}^L = 39.65$, K_i^L $=30 \times 10^{-3}$, $K_{SL}^L =$ - 2.1×10^{-3}.

nodes A_U and A_L represent the SLC resonances in the two channels respectively. Nodes **1** and **2** represent the sources for upper and lower bands while the node **3** represents the load to the two channels due to radiation from SLC. K_i^U and K_i^L represent the internal couplings between conventional SIW resonators and SLC, while K_{SL}^U and K_{SL}^L represent the source to load couplings due to radiation from microstrip feeding lines interfering with that from SLC.

In this paper, the upper channel is synthesized to operate at $f_U = 5.85$ GHz, with a bandwidth of 5% and two TZs located at 5.4 GHz and 6.3 GHz, while the lower channel operates at $f_L = 5.3$ GHz, with a bandwidth of 3.4 % and the TZs located at 5 GHz and 5.6 GHz respectively. Both resonators in upper channel resonate at f_U and the ones in lower band resonate at f_L. The synthesis can be carried out using techniques mentioned in [37, 6]. These techniques are embedded in commercial softwares, e.g. Versatile Microwave. Once the parameter values in coupled resonator model are obtained, individual components can be designed as shown in the next section. Only the design methodology for upper channel is presented in the next section, with the understanding that the design of lower band is carried out using the corresponding steps.

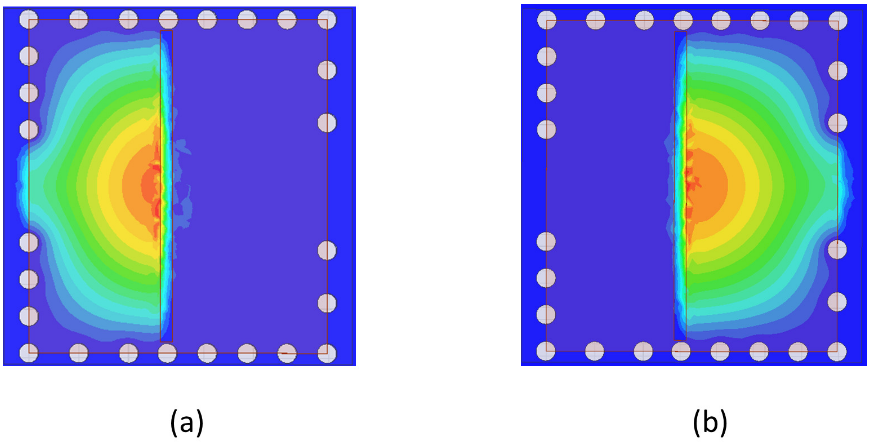

Figure 3.27: Electric field pattens in the SLC at (a) f_U and (b) f_L. The field patterns were obtained using eigenmode solver in HFSS.

3.4.1.2 Full-Wave Simulations

3.4.1.2.1 Conventional SIW Cavity

The resonance frequency of the conventional SIW cavity in TM_{110} mode is given as

$$f_C^U = \frac{c_0}{2\sqrt{\epsilon_r}}\sqrt{(\frac{1}{a_1})^2 + (\frac{1}{b_1})^2} \tag{3.19}$$

where c_0 is the speed of light in vacuum.

3.4.1.2.2 The SLC

The SLC has two radiating modes on either side of the common slot as shown in Fig. 3.27. The field patterns of these modes resemble that of a half-mode SIW (HMSIW) resonator [47]. The frequency variations of the resonant mode in SLC and that of a corresponding HMSIW resonator is shown in Fig. 3.28. It can be observed that the two frequencies closely follow each other. This enables the resonant frequency of node A_U to be approximated as:

$$f_A^U \approx f_{HMS} = \frac{c_0}{2\sqrt{\epsilon_r}}\sqrt{(\frac{1}{2a_2})^2 + (\frac{1}{b_2})^2} \tag{3.20}$$

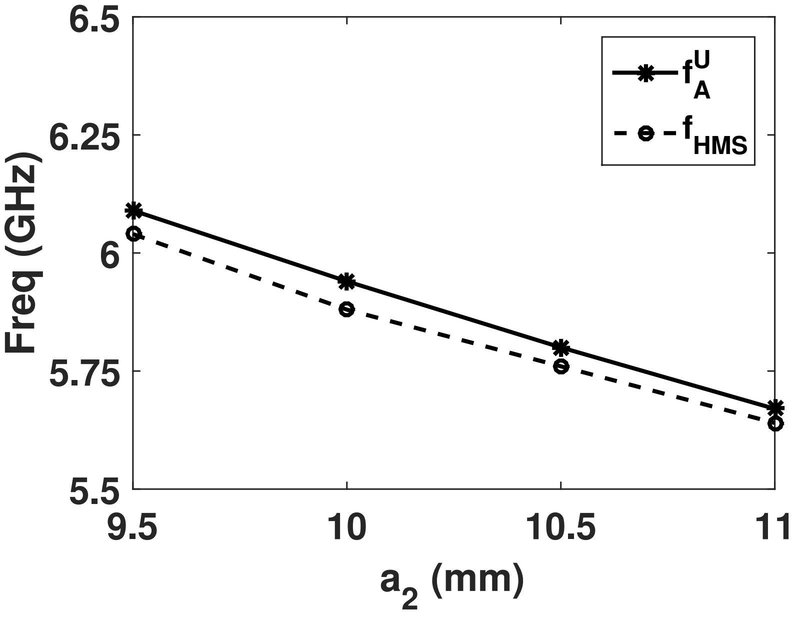

Figure 3.28: Variation of resonance frequenicies in the SLC for upper channel and in the corresponding HMSIW resonator. The dimension of the HMSIW resonator used in the simulation is $a_2 \times b_2$.

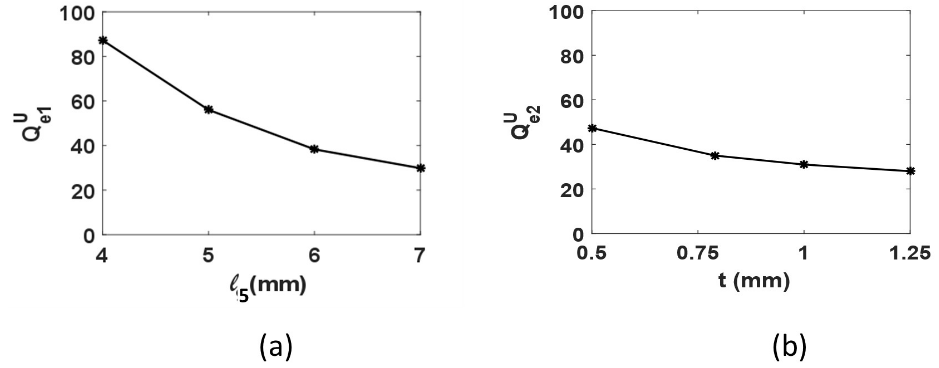

Figure 3.29: Variation of Q_{e1}^{U} and Q_{e2}^{U} with relevant parameters.

where f_{HMS} is the resonance frequency of TM_{110} mode in the corresponding HMSIW cavity.

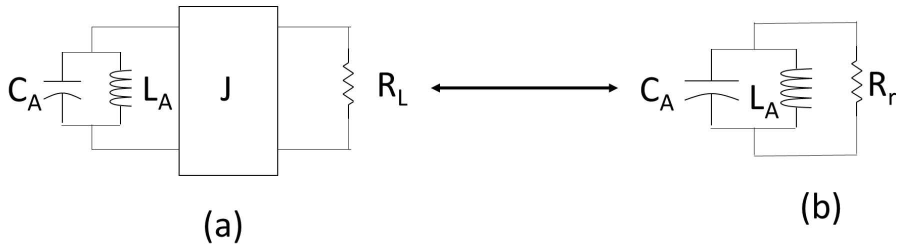

Figure 3.30: Equivalent representations of the SLC resonator with the external load, $R_L = R_r/J^2$.

3.4.1.2.3 External Quality Factor

The value of Q^U_{e1} can be calculated as [1]:

$$Q^U_{e1} = \frac{f^U_C . \tau}{4} \tag{3.21}$$

where τ is the reflection group delay of loaded conventional SIW cavity at f^U_C. The variation of Q^U_{e1} with the inset feeding structure is shown in Fig. 3.29 (a).

The variation of Q^U_{e2} with the substrate thickness is shown in Fig. 3.29 (b). The value of Q^U_{e2} can be obtained by extracting the value of SLC's loaded quality factor using the eigenmode solver in EM simulation software (HFSS). This is because Q^U_{e2} of externally loaded resonator A_U is equal to the loaded quality factor Q_u of SLC with R_r denoting resistance due to radiation (Fig. 3.30). The above steps allow a designer to use the coupling matrix method to carry out the entire design process of the filtering antenna.

3.4.1.2.4 Coupling coefficients

The combined radiation from coplanar waveguide inset into conventional SIW cavity and that from microstrip line is responsible for generation and control of TZs in the frequency response of the filtering antenna and is accounted by negative value of the coupling coefficient K^U_{SL}. This way, the TZ locations can be controlled without modifying the main filtering network or its passband response. Shown in Fig. 3.31 (a) is the variation of TZs in the response of upper band channel with varying microstrip line length. Again, the TZs in the response of

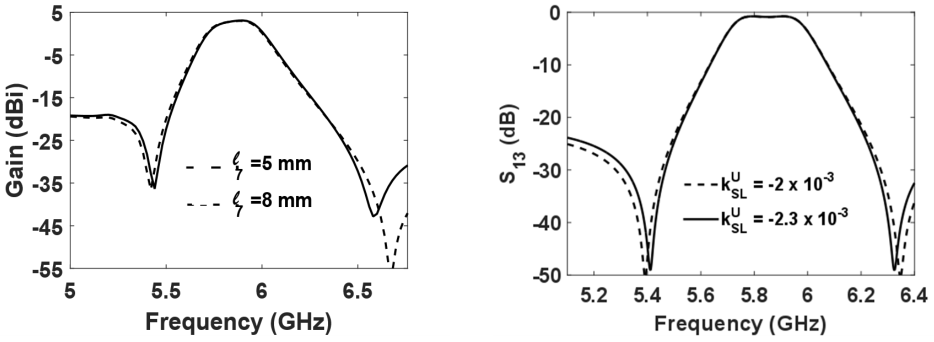

(a) (b)

Figure 3.31: Variation of TZ location with (a) feeding line length (b) source-load coupling.

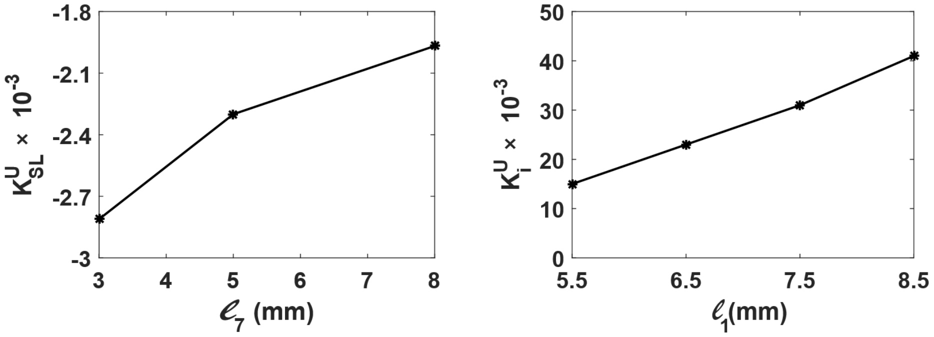

(a) (b)

Figure 3.32: Variation of coupling coefficients (a) K_{SL}^U and (b) K_i^U with relevant dimensions.

coupled resonator scheme (Fig. 3.26) can be controlled through variation of K_{SL}^U as shown in Fig. 3.31 (b). The two figures allow for mapping of microstrip-line length with K_{SL}^U (Fig. 3.32 (a)) [40]. It shoulsd be noted that only the TZ on the lower side of the passband is used for mapping as the higher frequency TZ is far away from the passband and the synthesis model is only valid for narrowband filters [60]. However, frequency-variant couplings [61] can be used to accurately model the upper TZ (primarily, as R_L changes with frequency).

Finally, the internal coupling factor, K_i^U is given as [1]:

$$K_i^U = \frac{f_1^2 - f_2^2}{f_1^2 + f_2^2} \tag{3.22}$$

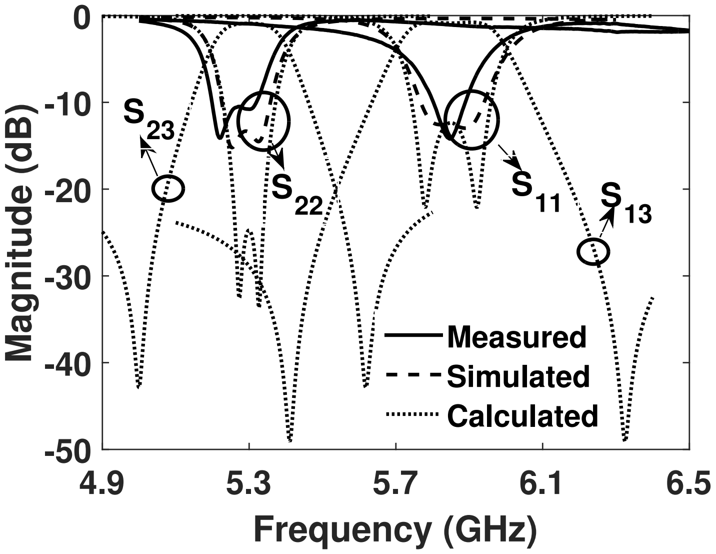

Figure 3.33: S-parameters of the filtering antenna.

where f_1 and f_2 are the resonance frequencies of the coupled conventional SIW and SLC structure. K_i^U can be controlled by varying the iris window size between the two resonators (Fig. 3.32 (b)).

3.4.2 Measurements

The DFA is manufactured using standard single layer printed circuit board (PCB) fabrication process. The size of the ground plane of the DFA is 35 mm × 107.5 mm (or 0.92 λ_g × 2.82 λ_g, where λ_g is the guided wavelength at f_L in the substrate). The calculated, simulated and measured frequency responses of the DFA are shown in Fig. 3.33, Fig. 3.34 and Fig. 3.35. From Fig. 3.33, it can be seen that the measured f_U is 5.8 GHz and f_L is 5.25 GHz, leading to a intra-channel frequency ratio (FR) of 1.1. Both channels are well matched, with return loss values greater than 13 dB. The maximum broadside gain values at upper and lower channels are 2.7 dBi and 2.65 dBi respectively with corresponding measured bandwidths of 4.5% and 3.6% (Fig. 3.34). Slight shifts in the frequencies can be attributed to fabrication tolerances. A pair of TZs can be observed on either side of the passband for both the lower channel (at 5 GHz and 5.6 GHz) and the upper channel (at 5.35 GHz and 6.5 GHz). The suppression

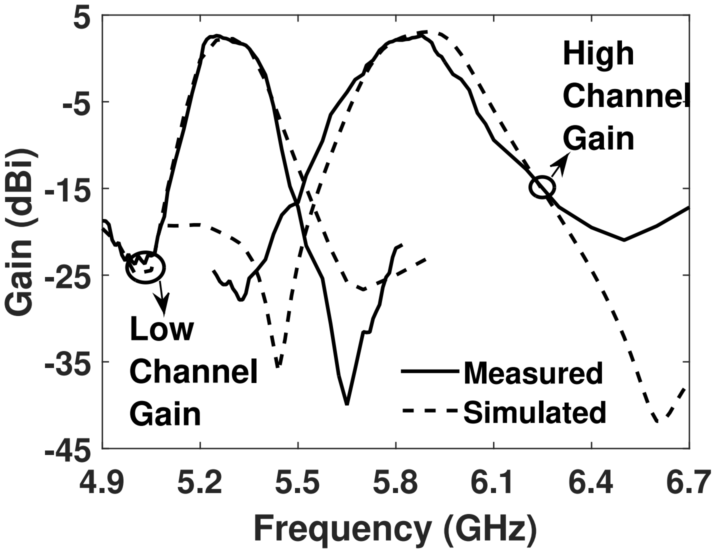

Figure 3.34: Gain response of the filtering antenna. Upper channel gain curves are obtained by feeding DFA through Port 1 and terminating Port 2 with a matched load. Similarly, low channel gain curves are obtained by feeding DFA through Port 2 and terminating Port 1 with a matched load.

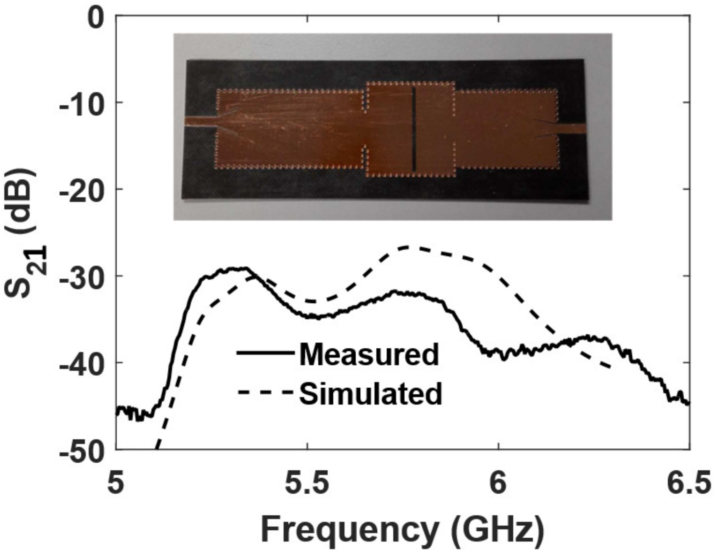

Figure 3.35: Transmission coefficient of the DFA. Shown in inset is a photograph of the fabricated DFA.

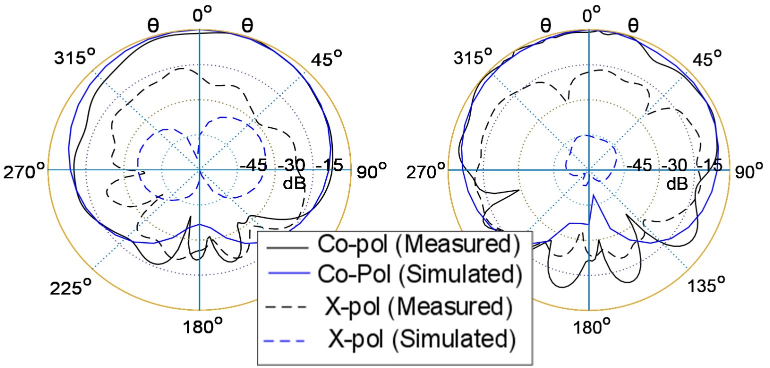

(a) x-z plane

(b) y-z plane

Figure 3.36: Radiation patterns at 5.25 GHz.

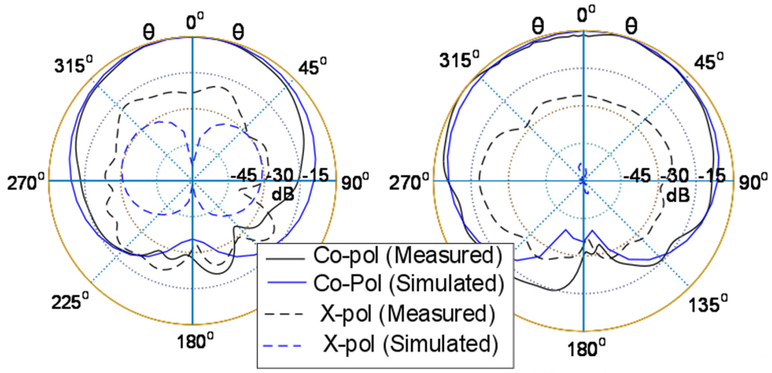

(c) x-z plane

(d) y-z plane

Figure 3.37: Radiation patterns at 5.8 GHz.

produced by the TZs in the measured results compared to simulations is reduced due to spurious radiation from coaxial cables in antenna chamber [62]. However, the broadside gain value of radiation produced at f_L, when only Port 1 is excited is as low as -26 dBi, while it is -22 dBi at f_U when only Port 2 is excited.Again, it can be seen from Fig. 3.35 that the measured inter-port isolation is greater than 29 dB in both the channels.

The radiation patterns of the DFA in the lower channel and the upper channel are shown in Fig. 3.36 and Fig. 3.37 respectively. The cross-pole discrimination (XPD) over all the angles in E- and H-planes level is more than 13 dB for the lower channel, while it is larger than 18 dB for the upper channel. The measured XPD levels are reduced in comparison to the simulated ones due to unintended radiation from connecting coaxial cables.

Table 3.3: Comparison of DFAs

Ref.	**Quasi-elliptic response**	**Height (λ_g)**	**F.R.**	**Tech.**	**Min. XPD (dB) L.C./ U.C.**
[55]	No	0.022	2.14	Multi-layer/ Microstrip	≈19 /≈16
[56]	No	0.086	1.26	Multi-layer/ Microstrip	≈9/≈7.5
[57]	No	0.043	1.38	Multi-layer/ Microstrip	≈14/≈9
[58]	N/A	N/A	1.08	Single-layer/ SIW	N/A
[59]	No	N/A	1.11	Multi-layer/ Microstrip	≈11/≈16
This work	Yes	0.02	1.1	Single-layer/ SIW	≈13/≈ 17

[*] Note: L.C. : Lower Channel, U.C. : Upper Channel

Comparison of the proposed design with the DFAs presented in literature are shown in Table 3.3. The Table clearly brings out the advantages of the proposed DFA i.e. a single layer low-profile DFA with quasi-elliptic responses in both the channels. Moreover, the proposed design allows the two channels to be placed close to each other.

3.5 Dual-Band Filtering Antenna with Novel Transmission Zero Characteristics [63]

As described in the previous section, the selectivity of the filtering antenna can be improved by placing transmission zeroes (TZs) at pre-determined locations [31, 40, 53]. The TZs are not absolute nulls, but local minima due to imperfect cancellation of the far-fields or loss of EM power in resonators with finite quality factors. Filter theory states that a maximum of n TZs can be obtained from a n- order filter, if the couplings remain constant with frequency [1, 31, 40, 53]. This requires an increase in the number of resonators, leading to larger spatial footprint and associated material loss of the filtering antenna.

Recent trends in wireless communications has spurred the need for multi-band microwave components [47, 64, 52, 53, 48, 32, 34]. Again, for the two bands of a dual-band filtering antenna (DBFA) to be placed close to each other, the order of the filtering antenna needs to be increased. A solution lies in using orthogonal polarizations for the two bands, leading to greater inter-band isolation. The DBFA in [34] presents these capabilities, but suffers from difficulty of planar integration. A planar solution is presented in [47] but it requires numerous metallic vias, increasing the complexity and cost of antenna fabrication. Additionally, none of the two designs [34, 47] present transmission zeroes (TZs) in their frequency responses.

In this paper, a single-layer two-pole vialess DBFA with orthogonal polarizations in its two bands is presented. A total of three TZs are generated in the frequency response corresponding to each polarization of the DBFA. The DBFA is based on a common dual-mode T-shaped resonator. Each mode of the T-shaped resonator couples to one of the two orthogonally placed microstrip patch antennas. The nature of resonances in the T-shaped resonator gurantees the presence of two TZs in the frequency response of a radiator near the other antenna's operating frequency. Moreover, the far-field radiation of each mode of the T-shaped resonator interferes with that of the corresponding patch antenna at its broadside, leading to generation of another TZ in the antenna response. Again, the orthogonal polarizations of the two patch antennas allow the two bands to be placed close to each other with an inter-band frequency ratio as low as 1.14. Although the DBFA is not designed for any specific application, the proposed synthesis technique allows for design for most narrow to medium bandwidth (<10 %) applications.

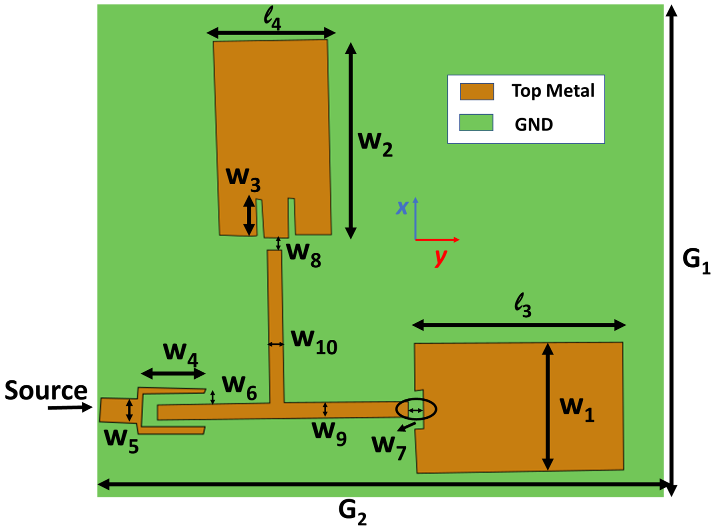

Figure 3.38: Schematic of the DBFA. All dimensions are in mm: $l_3 = 21$, $l_4 = 9$, $w_1 = 10$, $w_2 = 24.3$, $w_3 = 4.8$, $w_4 = 5.2$, $w_5 = 1.8$, $w_6 = 0.5$, $w_7 = 0.5$, $w_8 = 0.9$, $w_9 = 1.5$, $w_{10} = 1.2$, $G_1 = 70$, $G_2 = 50$.

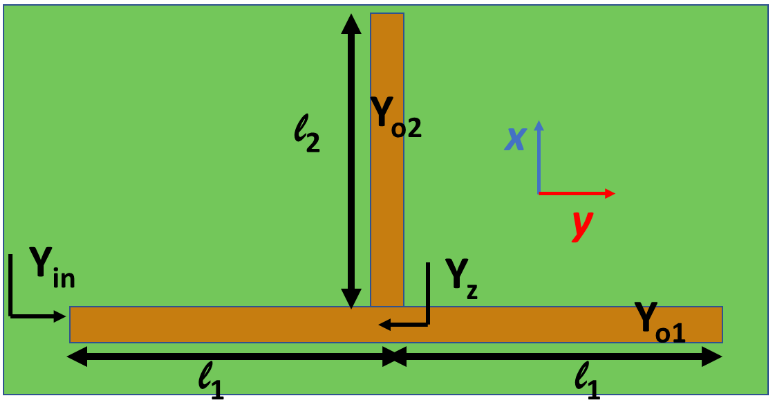

Figure 3.39: The TR with $l_1 = 11.3$ mm, $l_2 = 14.3$ mm, $Y_{o1} = (1/56)$ S, $Y_{o2} = (1/64.3)$ S

3.5.1 Design

Shown in Fig 3.38 is the schematic of the proposed DBFA. The filtering antenna is implemented on a Rogers RT/Duroid 5880 board ($\epsilon_r = 2.2$, $\tan\delta = 0.001$) with thickness $t = 0.79$ mm. It is based on a dual-mode TR (Fig. 3.39) fed by a microstrip line, with each mode of the TR being independently controllable. Each mode of the TR is coupled to one of the two

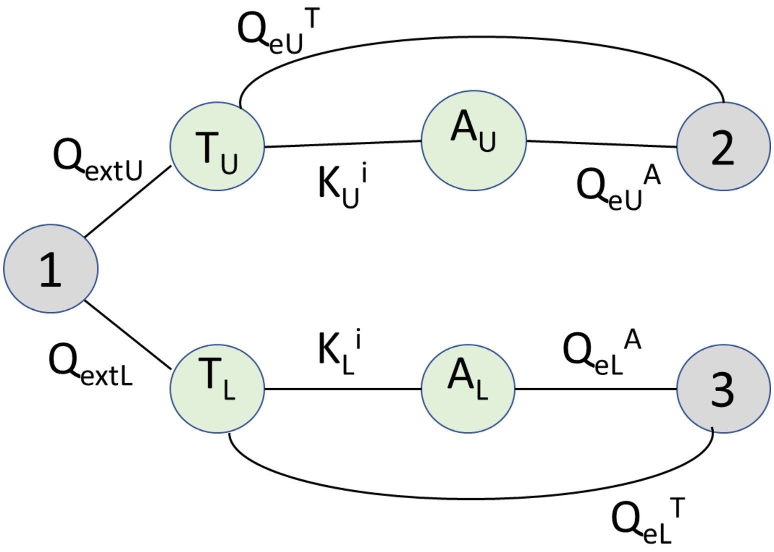

Figure 3.40: Coupling scheme of the DBFA. Parameter values: $K_U^i = 2.5 \text{ x } 10^{-2}$, $Q_{eU}^A = 45.11$, $Q_{eU}^T = 102.54$, $Q_{extU} = 26.53$, $f_U^A = 4.75$ GHz, $f_U^T = 4.66$ GHz, $K_L^i = 1.5 \text{ x } 10^{-2}$, $Q_{eL}^A = 50.88$, $Q_{eL}^T = 236.46$, $Q_{extL} = 100.35$, $f_L^A = 4.13$ GHz, $f_L^T = 4.09$ GHz .

patch antennas, leading to a two pole response in the two bands of the DBFA. Orthogonal polarizations are obtained in the two bands of the DBFA, due to the orientations of the patch antennas with respect to each other.

3.5.1.1 Coupling Scheme

Shown in Fig. 3.40 is the coupling scheme of the DBFA. Node 1 represents the source, while nodes 2 and 3 represent the resistive loads due to radiation in upper and lower bands respectively. Nodes T_U and T_L represent the upper and lower modes of the TR, while the nodes A_U and A_L represent the patches in the two bands respectively. Again, K_U^i and K_L^i represent the internal coupling coefficients of the upper and lower bands of the DBFA. The external coupling coefficients Q_{eU}^A and Q_{eL}^A are due to radiation from the patch antennas, whereas Q_{eU}^T and Q_{eL}^T are due to radiation from the two modes of TR. Finally, Q_{extU} and Q_{extL} represent the external coupling coefficients of the upper and lower modes of the TR due to microstrip feeding line.

In this paper, the DBFA is designed with the upper band centered at f_U = 4.7 GHz, 10 dB return loss bandwidth of 3% and a TZ at 4.85 GHz, while the lower band is centered at f_L = 4.1 GHz, with a bandwidth of 1.2 % and a TZ at 4.2 GHz. The parameters for each band can be synthesized independently using a commercial software, e.g. Versatile Microwave. Once the parameters are extracted, individual components of the DBFA can be designed as shown in the next section. Only the design methodology for upper band components is shown below, with the understanding that corresponding steps can be followed for the lower band.

3.5.1.2 Full Wave Simulations

3.5.1.2.1 The TR

From Fig. 3.39, the input admittance of the TR can be given as:

$$Y_{in} = Y_{o1}(\frac{Y_{eq} + jY_{o1}\tan(\beta l_1)}{Y_{o1} + jY_{eq}\tan(\beta l_1)}) \tag{3.23}$$

where Y_{eq} =$j(Y_{o1}\tan(\beta l_1) + Y_{o2}\tan(\beta l_2))$ and $\beta = (2\pi f\sqrt{\epsilon_r})/c_0$, with c_0 being the speed of light in vacuum. Now, for resonance $Y_{in} = 0$, which leads to the two eigenmode equations of the TR:

$$\frac{2\pi f_U^T\sqrt{\epsilon_r}}{c_0}l_1 = \frac{\pi}{2} \tag{3.24}$$

$$Y_{01}\tan(\frac{2\pi f_L^T\sqrt{\epsilon_r}}{c_0}l_1) = -Y_{02}\tan(\frac{2\pi f_L^T\sqrt{\epsilon_r}}{c_0}l_2) \tag{3.25}$$

It can be seen from the above equations that as long as the tranmsision line with characteristic admittance Y_{o2} is attached at the centre of the line with admittance Y_{o1}, the frequency given by (2.1) can be controlled through l_1 independently (Fig. 3.41(a)). Therafter, the second resonance frequency can be controlled independently through l_2, while keeping l_1 constant (Fig. 3.41(b)). Shown in Fig. 3.42 are the field patterns of the TR at the two resonance frequencies.

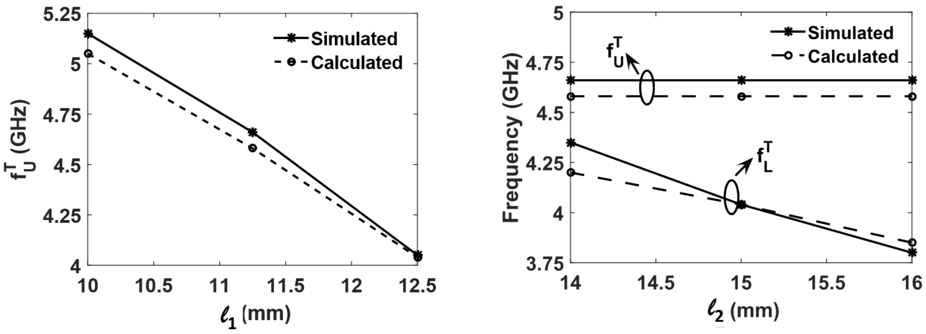

(a) (b)

Figure 3.41: Variation of (a) f_U^T and (b) f_L^T with corresponding dimensions.

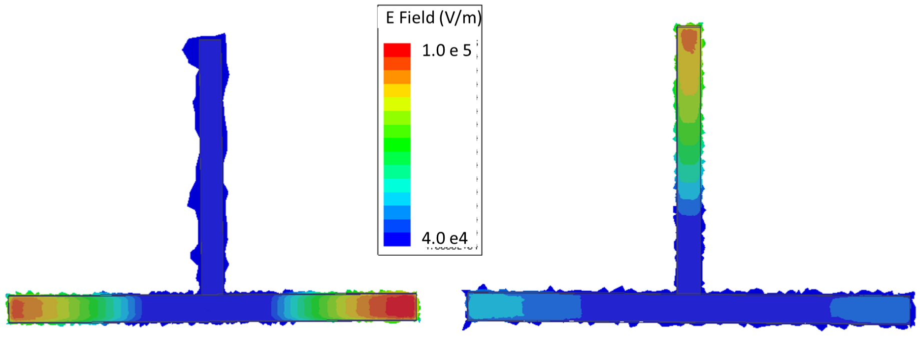

(a) (b)

Figure 3.42: Electric field patterns on the TR at (a) f_U^T and (b) f_L^T .

3.5.1.3 The Patch

Patch antennas have been widely studied in the literature. The resonannce frequency f_U^A can be calculated using formulas given in the literature [26]. The longer side of the patch (l_3) is approximately half-wavelength long at the resonant frequency, with its two open ends functioning as radiators.

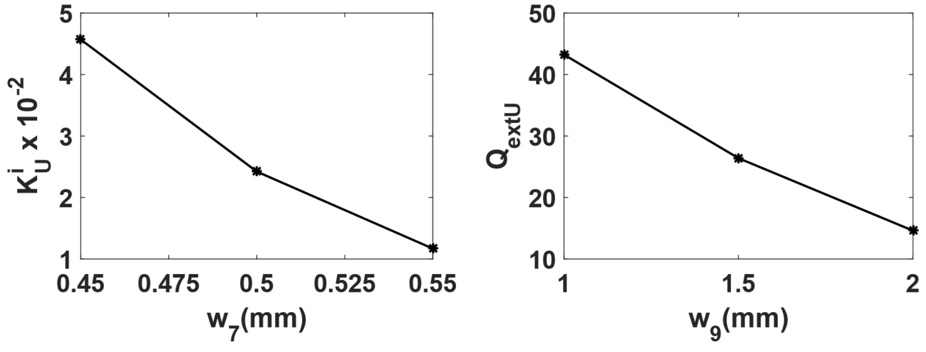

(a) (b)

Figure 3.43: Variation of (a) coupling coefficient (b) external quality factor with relevant dimensions.

3.5.1.4 Coupling Coefficient

The coupling coefficient can be calculated as [1]:

$$K_U^i = \frac{1}{2}\Big(\frac{f_U^A}{f_U^T} + \frac{f_U^T}{f_U^A}\Big)\times \sqrt{\Big(\frac{f_1^2 - f_2^2}{f_1^2 + f_2^2}\Big)^2 - \Big(\frac{{f_U^A}^2 - {f_U^T}^2}{{f_U^A}^2 + {f_U^T}^2}\Big)^2} \tag{3.26}$$

where f_1 and f_2 are the resonance frequencies obtained due to coupling of TR and the patch antenna. Shown in Fig. 3.43 (a) is the variation of coupling coefficient with varying gap between the TR and the patch antenna.

3.5.1.4.1 External Quality Factors

Q_{extU} can be calculated as [1]:

$$Q_{extU} = \frac{f_U^T . \tau}{4} \tag{3.27}$$

where τ is the reflection group delay of the TR at f_U^T. The variation of Q_{extU} with the feeding structure is shown in Fig. 3.43 (b).

Q_{eU}^A can be obtained by extracting the loaded quality factor of the patch antenna using the eigenmode solver in EM simulation software (HFSS). This is because Q_{eU}^A of the externally loaded resonator A_U due to radiation is equal to the loaded quality factor of patch antenna

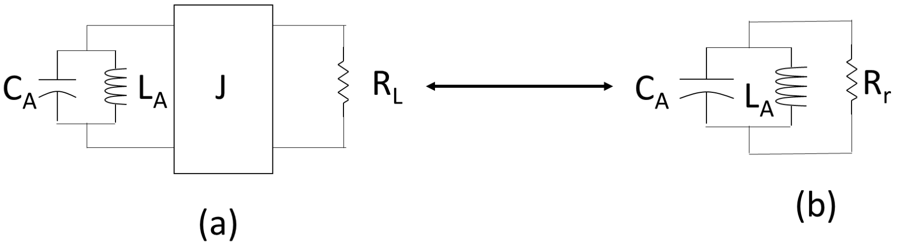

Figure 3.44: Equivalent representations of the patch antenna with the external load, $R_L = R_r/J^2$.

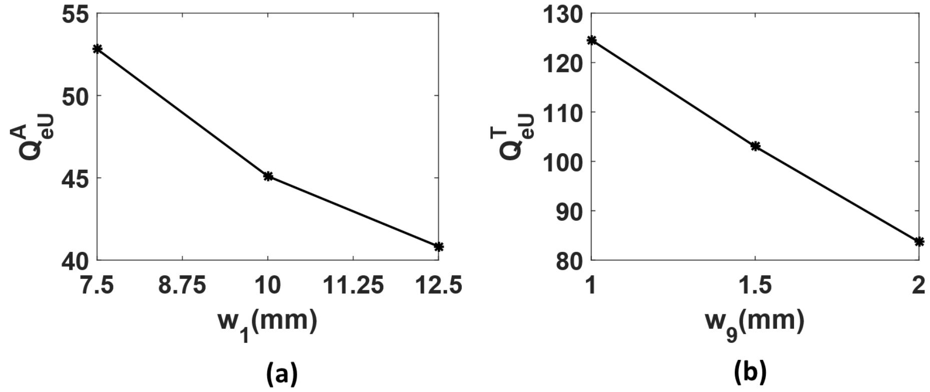

Figure 3.45: Variation of (a) Q^A_{eU} and (b) Q^T_{eU} with relevant dimensions.

with R_r denoting the resistance due to radiation (Fig. 3.44). The variation of Q^A_{eU} is shown in Fig. 3.45 (a) . Similar trend is obtained for Q^T_{eU} (Fig. 3.45 (b)), which can also be directly extracted using EM simulator. However, the value of Q^T_{eL} obtained from eigenmode solution should be approximately doubled for synthesis purposes as only one of the radiating end contributes to the X-polarized radiation.

3.5.1.4.2 The TZs

From the frequency response of Y-polarized filtering antenna (Fig. 3.46), the presence of three TZs can be observed at the broadside of the antenna ($\theta = 0$). For understanding the nature of TZs, it is important to consider the resonances in TR (Fig. 3.39). Here,

$$Y_z = j(Y_{01}\tan(\frac{2\pi f^T_L\sqrt{\epsilon_r}}{c_0}l_1) + Y_{02}\tan(\frac{2\pi f^T_L\sqrt{\epsilon_r}}{c_0}l_2) \tag{3.28}$$

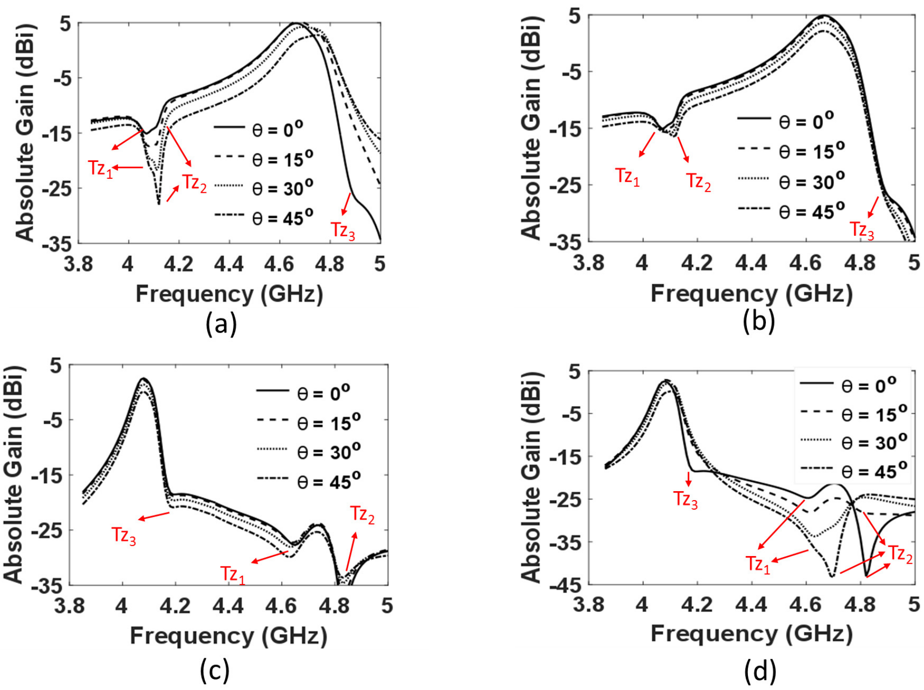

(a) (b) (c) (d)

Figure 3.46: The effect of varying observation angle on the TZs of the DBFA: (a) Y-polarized response in y-z plane (b) Y-polarized response in x-z plane (c) X-polarized response in y-z plane and (d) X-polarized response in x-z plane. The angle θ is measured from the broadside of the filtering antenna.

The TZ is generated when $Y_z = 0$, which gives the same condition as (3.25) - the eigenmode equation of the TR mode associated with the low (X- polarized) band. That is, TZ would be present in the Y-polarized frequency response near the passband of X-polarized filtering antenna. Now, due to two-pole nature of the filtering antenna, each mode of the TR itself has two resonances associated with itself. This, in turn, leads to presence of two TZs in the frequency response of the Y-polarized filtering antenna. Thus, the two-pole nature not only increases the passband bandwidth of the Y-polarized filtering antenna, but also leads to presence of two TZs in its frequency response due to two-pole nature of X-polarized filtering antenna - essentially producing a stopband.

Again, it can be seen from Fig. 3.46 (a) that the locations of Tz_1 and Tz_2 do not alter with the change in observation angle. These TZs are intrinsic to the structure of the filtering antenna. However, the patch antenna and upper mode resonance in TSR act as elements

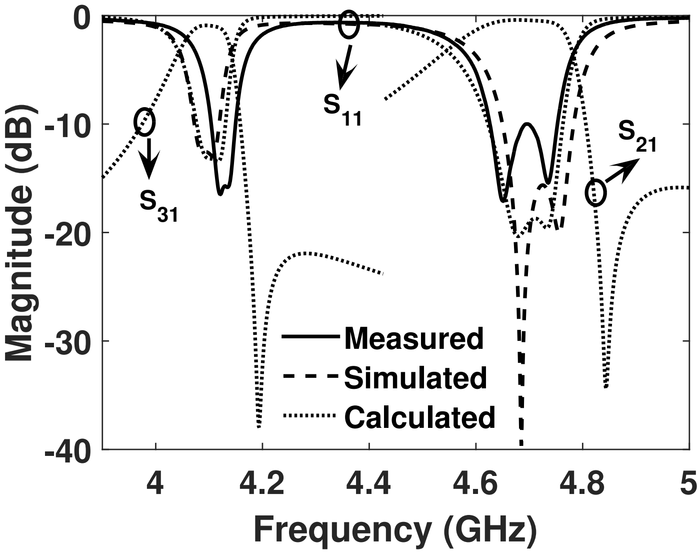

Figure 3.47: The S-parameter response of the DBFA.

of a y-directed linear array - with changing phase due to electromagnetic coupling - leading to change of Tz_3 (due to field interference or, due to combined effect of Q^T_{eU} and Q^A_{eU} at the node 2 in Fig. 3.40) location with observation angle. This affect is not seen in the z-x plane as each radiator behaves as an individual component (Fig. 3.46 (b)). Similarly, for the X-polarized frequency response the position of Tz_3 remains constant in z-y plane (Fig. 3.46 (c)), but changes in z-x plane (Fig. 3.46 (d)). Slight variations in location of intrinsic TZs can be observed due to cross-polarized radiation of the orthogonally located radiator, however both intrinsic TZs remain near the passband of orthogonal antenna.

3.5.2 Measurements

The DBFA is manufactured using the standard vialess single-layer printed circuit board (PCB) fabrication process. The size of the ground plane of the DBFA is 70 mm × 50 mm (or 1.42 $\lambda_g \times \lambda_g$, where λ_g is the guided wavelength at f_L in the substrate). The calculated, simulated and measured S-parameters of the DBFA are shown in Fig. 3.47. It can be seen that the measured f_U is 4.7 GHz, while f_L is 4.13 GHz, leading to an inter-band frequency ratio of 1.14. Both bands are well matched with return loss greater than 10 dB in the passbands. The measured bandwidth in Y-polarized (higher) band is 2.9 %, while that of

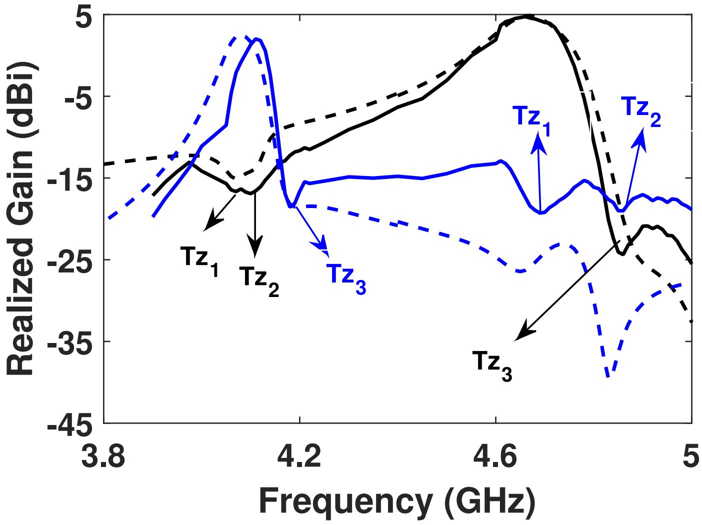

Figure 3.48: The measured (solid line) and the simulated (dashed line) realized gain response of the DBFA at its broadside (-z direction). The Y-polarized realized gain curve is shown in black, while the X-polarized realized gain is shown in blue. The TZs are explicitly marked for easier identification. The two Tz_3 are caused due to far-field interference of patch and TSR.

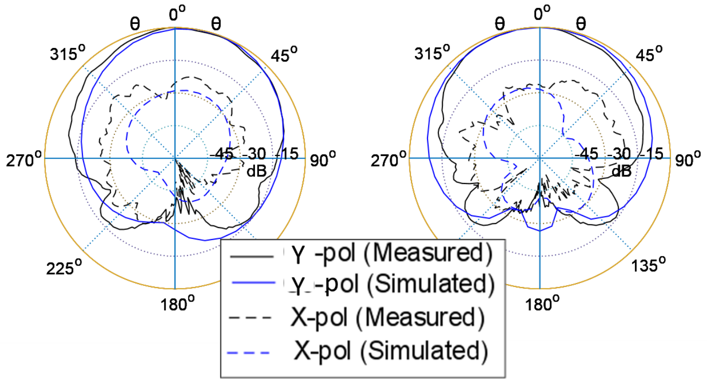

(a) y-z plane (b) x-z plane

Figure 3.49: Radiation patterns of the DBFA at f_U.

the X-polarized (lower) band is 1.2 %.

The realized gain characteristics of the DBFA are shown in Fig. 3.48. The Y-polarized response has a maximum realized gain of 4.8 dBi at it's broadside, while the X-polarized response has a maximum realized gain of 2.2 dBi. There are three TZs in the frequency

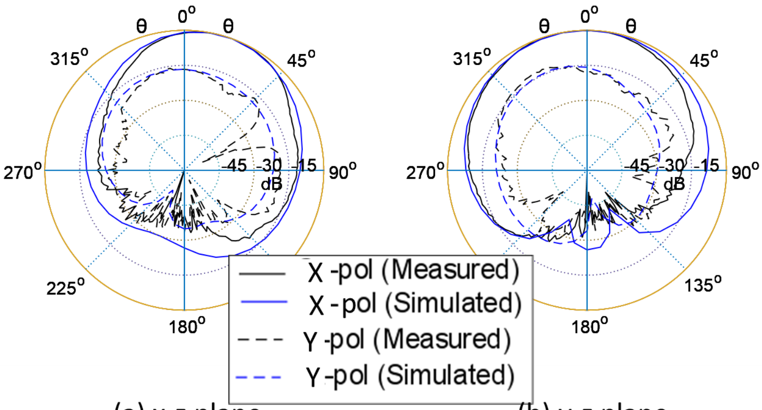

(a) x-z plane (b) y-z plane

Figure 3.50: Radiation patterns of the DBFA at f_L.

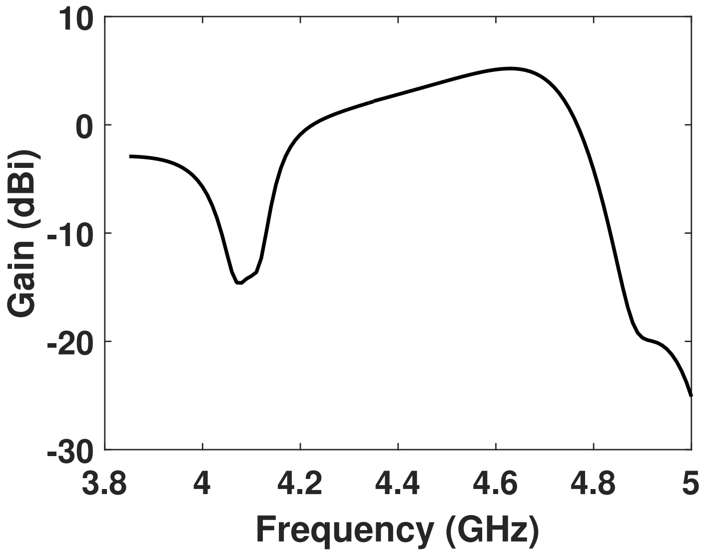

Figure 3.51: Y-polarized gain response of the DBFA at its broadside.

response of the Y-polarized response: at 4.06 GHz, at 4.11 GHz and at 4.85 GHz. Similarly, the X-ploarized response has two intrinsic TZs (at 4.7 GHz and at 4.85 GHz) and a TZ caused due to far-field interference at the broadside (at 4.18 GHz). The cross-pole discrimination is greater than 24 dB at f_U, while it is greater than 17 dB at f_L. The radiation patterns of the DBFA at f_U are shown in Fig. 3.49. It can be seen that the main beam is tilted in the y-z plane. This is beacuse the upper mode of the TSR and the Y-polarized patch antenna act as a two-element linear array . Similar beam-tilting is observed in x-z plane at f_L (Fig.

Table 3.4: Comparison of Filtering Antennas

Ref.	**Tzs**	**Frequency Ratio**	**Technology**	**Orthogonal Polarization**	**Height** (λ_g)
[64]	N.A.	1.16	1 Layer / SIW	Yes	.016
[52]	N.A.	1.44	2 Layer / microstrip	No	N.A.
[53]	4	1.36	1 Layer / microstrip	No	0.014
[48]	N.A.	2.36	2 Layer / microstrip	Yes	0.015
[35]	N.A.	1.24	Horn	Yes	N.A.
This Work	6	1.14	1 Layer/ microstrip	Yes	0.016

* Note: L.C. : Lower Channel, U.C. : Upper Channel

3.50). The array effect leads to varying gain with frequency (Fig. 3.51) and is manifested in the realized gain of Fig. 3.48 as:

$$Realized\ Gain = (1 - |S_{11}|^2) \times Gain \tag{3.29}$$

Comparison of the proposed DBFA with previously published works is shown in Table 3.4. It can be observed that the proposed DBFA is a single-layer vialess design with 6 TZs (3 each in X-polarized and Y-polarized responses) in its frequency response. Additionally, orthogonal polarizations of the radiators corresponding to the two bands enables the bands to be placed close to each other.

CHAPTER 4

On-chip Terahertz Filtering Antenna

At microwave frequencies, the passive devices are connected to the integrated circuits (ICs) through interconnects. This is done to take advantage of silicon technology for active devices, with low-loss substrates functioning as materials for microwave passives [65]. However front ends at terahertz frequencies can not afford the interconnects due to heavy losses in the metallic conducting wires [66], calling for on-chip antenna solutions. The standared CMOS technology has its own problems for antenna integration, primary being the thin substrates [67]. The very thin substrate drastically decreases the antenna radiation efficiency. For future terahertz applications, it is strongly desirable to achieve high-efficiency antennas, which would lead to integrated transmitters and receivers with efficiency much higher than the current state of the art.

Leaky wave Antennas (LWAs) have been proposed as candidates to increase the efficiency of terahertz front-ends, however their large size makes the use prohibitive on commercial CMOS wafers. On the other hand, the resonant antennas not only suffer from low radiation efficiencies, but also narrow bandwidths (1%-2%) [68]. Considering that the CMOS technology is not well characterized at terahertz regime, small changes in antenna resonance frequency can render the front-end mismatched to the antenna.

In this small section, we present a SIW antenna [69] operating on 550 GHz based on commercial 65 nm CMOS technology (Fig. 4.1). To prevent most of radiation leaking into high permittivity Si, the bottom-most copper layer is used as the ground plane of the antenna. The top-most copper layer is used to feed the antenna through a copper-line. However, the role of SIW top surface is taken over by the aluminium layer. Even though aluminium has lower electrical conductivity than copper, the additional height provided by a layer of

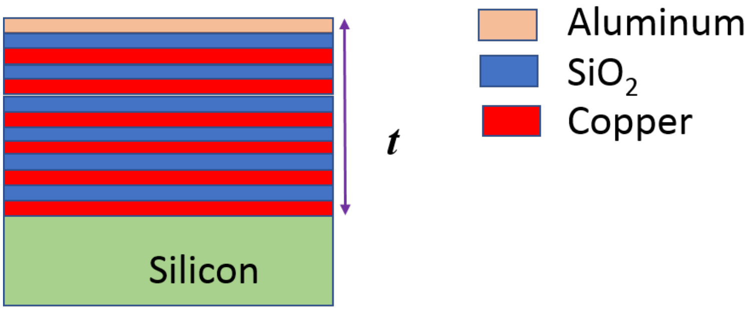

Figure 4.1: Dielectric stack-up of the proposed antenna.

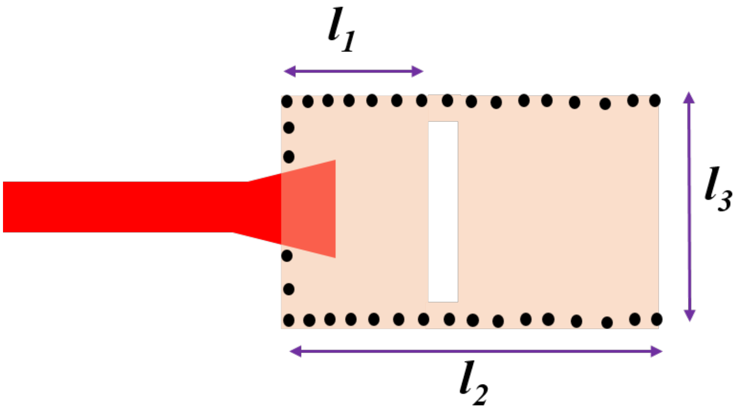

Figure 4.2: Top-view schematic of the proposed antenna with only the top copper layer and aluminium layer shown. Here, $l_1 = 60$ μm, $l_2 = 237$ μm and $l_3 = 93$ μm.

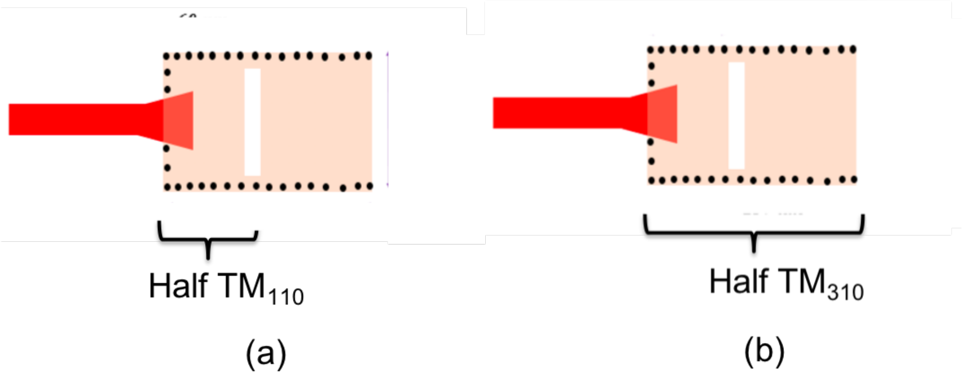

Figure 4.3: Effective cavities for (a) half TM_{110} mode (b) half TM_{310} mode.

silicon-di-oxide and air increases the cavity Q.

The schematic of the proposed antenna is shown in Fig. 4.2. As described in previ-

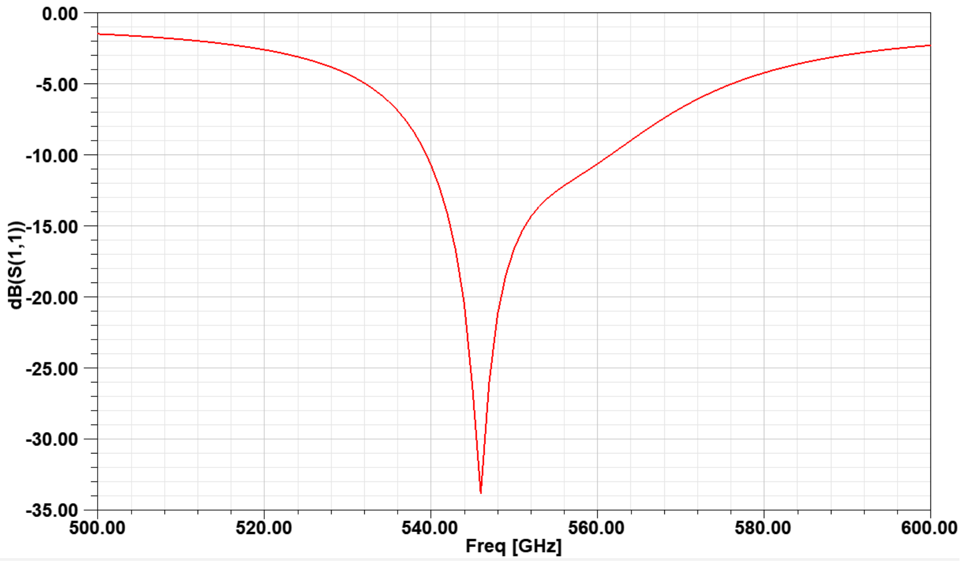

Figure 4.4: Simulated frequency response of the antenna.

ous chapter, a half TM_{110} mode is generated in the cavity with dimension $l_1 \times l_3$ and the corresponding frequency given as:

$$f_{HM1} = \frac{c_0}{2\sqrt{\epsilon_r}} \sqrt{(\frac{1}{2l_1})^2 + (\frac{1}{l_3})^2} \tag{4.1}$$

where ϵ_r is the effective permittivity of substrate between top aluminium layer and the bottom copper layer. The antenna radiates from the open edge (or the slot of width $l_2 - l_1$) of corresponding cavity.

On the other hand, the cavity of cross-sectional size $l_2 \times l_3$ resonates in the half TM_{310} mode with the operating frequency given as:

$$f_{HM3} = \frac{c_0}{2\sqrt{\epsilon_r}} \sqrt{(\frac{3}{2l_2})^2 + (\frac{1}{l_3})^2} \tag{4.2}$$

The presence of slot not only provides radiation for TM_{110} modes, but also causes capacitive loading on the TM_{310} mode. Therefore, the dimensions l_1 and l_2 are taken as such the two modes operate close (in frequency domain) to each other. The inter-frequency gap can be used to set the bandwidth of the antenna, while the presence of two radiators being half-wavelength away from each other increases its broadside directivity.

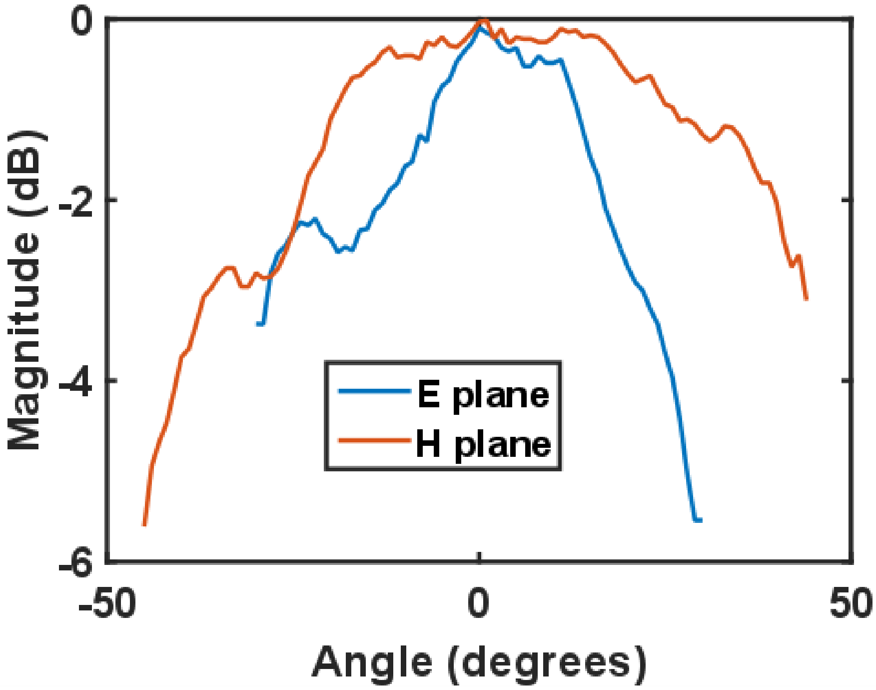

Figure 4.5: Radiation patterns of the antenna.

Shown in Fig. 4.4 is the simulated frequency response of the antenna. The antenna has a 10-dB reflection loss bandwidth of 20 GHz or 3.6%, which is approximately twice that of conventional patch antennas. For measuring the radiation pattern of the antenna, the antenna is driven by a triple-pushed Colpitts voltage-controlled oscillator [70]. The measured radiation patterns of the antenna are shown in Fig. 4.5. The measured 3-dB beamwidths in the E-plane (θ_E) and H- plane (θ_H) are 55°and 85°resepectively. The directivity can be approximated as [19]:

$$D = \frac{32400}{\theta_E \theta_H} \tag{4.3}$$

which gives D = 6.93. Using the simulated efficiency of 22% together with measured directivity, we arrive at the gain value of 1.89 dB, which is the highest reported gain for a resonant antenna in the literature.

CHAPTER 5

Conclusion

The dissertation provides contributions made by the author in the field of filters and filtering antennas. Simulations and measured results have been provided to support the benefits of using dual-mode and dual-resonance resonators for realising the devices.

In Chapter 2, a transmission line equivalent model is presented for a Möbius Loop Resonator based filter and subsequently a microstrip version is implemented for the same. This is followed by introduction of dual-mode and a dual-resonance SIW cavity for realizing a dual-band filter. The last section of the chapter focuses on integration of planar resonators with SIW cavities to obtain high Q, compact PCB-based filters.

Chapter 3 delves into the topic of filtering antennas. Source-Load coupling is introduced for the first time to introduce flexible TZs in the response of a filtering antenna. THis is followed by introduction of first single-layer dual-band filtering antenna with orthogonal polarizations in the two bands. We proceed to introduce a full-coupling matrix synthesis model for filtering antennas and use it to implement a single layer diplexing filtering antenna. Finally, a vialess microstrip filtering antenna is introduced which breaks the fundamental limit of maximum possible n- TZs from a n resonator based filter, provided that a multi-band filtering antenna is implemented.

The last chapter of substance - Chapter 4 details a broadband and high gain on-chip antenna for terahertz application. This antenna is implemented on 65 nm commercial CMOS technology and uses filtering antenna techniques to realise the desired properties.

REFERENCES

[1] J.-S. G. Hong and M. J. Lancaster, *Microstrip filters for RF/microwave applications*, vol. 167. John Wiley & Sons, 2004.

[2] Sparkfun, “Etching your own circuit boards,” 2016.

[3] H. W. Bode *et al.*, “Network analysis and feedback amplifier design,” 1945.

[4] R. J. Cameron, C. M. Kudsia, and R. Mansour, *Microwave filters for communication systems.* John Wiley & Sons, 2015.

[5] G. Matthaei, “Microwave filters, impedance-matching networks, and coupling structures (artech microwave library),”

[6] W. A. Atia, K. A. Zaki, and A. E. Atia, “Synthesis of general topology multiple coupled resonator filters by optimization,” in *Microwave Symposium Digest, 1998 IEEE MTT-S International*, vol. 2, pp. 821–824, IEEE, 1998.

[7] D. Swanson and G. Macchiarella, “Microwave filter design by synthesis and optimization,” *IEEE Microwave Magazine*, vol. 8, no. 2, pp. 55–69, 2007.

[8] K. Dhwaj, H. Lee, L. Jiang, and T. Itoh, “Transmission-line equivalent and microstrip structure for planar möbius loop resonator,” in *Microwave Symposium (IMS), 2015 IEEE MTT-S International*, pp. 1–3, IEEE, 2015.

[9] E. Starostin and G. Van Der Heijden, “The shape of a möbius strip,” *Nature materials*, vol. 6, no. 8, p. 563, 2007.

[10] R. L. Davis, “Non-inductive electrical resistor,” Aug. 16 1966. US Patent 3,267,406.

[11] A. K. Poddar, D. Sundararajan, and U. L. Rohde, “Real time signal retention device using co-planar waveguide (cpw) as mobius strip,” in *Microwave Symposium Digest (IMS), 2013 IEEE MTT-S International*, pp. 1–4, IEEE, 2013.

[12] A. K. Poddar, U. L. Rohde, and D. Sundararajan, “A novel mobius-coupled printed resonator based signal sources,” in *Microwave Symposium Digest (IMS), 2013 IEEE MTT-S International*, pp. 1–4, IEEE, 2013.

[13] J. M. Pond, “Mobius dual-mode resonators and bandpass filters,” *IEEE Transactions on Microwave Theory and Techniques*, vol. 48, no. 12, pp. 2465–2471, 2000.

[14] K. Dhwaj, X. Li, Z. Shen, and S. Qin, “Cavity resonators do the trick: A packaged substrate integrated waveguide, dual-band filter,” *IEEE Microwave Magazine*, vol. 17, no. 1, pp. 58–64, 2016.

[15] J. Curtis and S. Fiedziuszko, “Miniature dual mode microstrip filters,” in *Microwave Symposium Digest, 1991., IEEE MTT-S International*, pp. 443–446, IEEE, 1991.

[16] Z.-C. Hao, W. Hong, J.-X. Chen, X.-P. Chen, and K. Wu, "Compact super-wide bandpass substrate integrated waveguide (siw) filters," *IEEE Transactions on Microwave Theory and Techniques*, vol. 53, no. 9, pp. 2968–2977, 2005.

[17] H. J. Tang, W. Hong, J.-X. Chen, G. Q. Luo, and K. Wu, "Development of millimeter-wave planar diplexers based on complementary characters of dual-mode substrate integrated waveguide filters with circular and elliptic cavities," *IEEE Transactions on Microwave Theory and Techniques*, vol. 55, no. 4, pp. 776–782, 2007.

[18] W. Shen, X.-W. Sun, W.-Y. Yin, J.-F. Mao, and Q.-F. Wei, "A novel single-cavity dual mode substrate integrated waveguide filter with non-resonating node," *IEEE Microwave and Wireless Components Letters*, vol. 19, no. 6, pp. 368–370, 2009.

[19] C. A. Balanis, *Advanced engineering electromagnetics.* John Wiley & Sons, 1999.

[20] A. L. C. Serrano, F. S. Correra, T.-P. Vuong, and P. Ferrari, "Synthesis methodology applied to a tunable patch filter with independent frequency and bandwidth control," *IEEE transactions on microwave theory and techniques*, vol. 60, no. 3, pp. 484–493, 2012.

[21] K. Dhwaj, R. Hadi, T. Yang, L. J. Jiang, J. Kovitz, and T. Itoh, "Planar resonator embedded substrate integrated waveguide (siw) cavity filter," in *2018 48th European Microwave Conference (EuMC)*, pp. 761–764, IEEE, 2018.

[22] X.-P. Chen and K. Wu, "Substrate integrated waveguide cross-coupled filter with negative coupling structure," *IEEE Transactions on Microwave Theory and Techniques*, vol. 56, no. 1, pp. 142–149, 2008.

[23] W. Shen, W.-Y. Yin, X.-W. Sun, and L.-S. Wu, "Substrate-integrated waveguide bandpass filters with planar resonators for system-on-package," *IEEE Transactions on Components, Packaging and Manufacturing Technology*, vol. 3, no. 2, pp. 253–261, 2013.

[24] W. Shen, L.-S. Wu, X.-W. Sun, W.-Y. Yin, and J.-F. Mao, "Novel substrate integrated waveguide filters with mixed cross coupling (mcc)," *IEEE Microwave and Wireless Components Letters*, vol. 19, no. 11, pp. 701–703, 2009.

[25] S. Sirci, M. Á. Sánchez-Soriano, J. D. Martı, V. E. Boria, F. Gentili, W. Bösch, R. Sorrentino, *et al.*, "Design and multiphysics analysis of direct and cross-coupled siw combline filters using electric and magnetic couplings," *IEEE transactions on microwave theory and techniques*, vol. 63, no. 12, pp. 4341–4354, 2015.

[26] R. C. Johnson and H. Jasik, "Antenna engineering handbook," *New York, McGraw-Hill Book Company, 1984, 1356 p. No individual items are abstracted in this volume.*, 1984.

[27] C.-K. Lin, S.-J. Chung, *et al.*, "A filtering microstrip antenna array," *IEEE Transactions on Microwave Theory and Techniques*, vol. 59, no. 11, pp. 2856–2863, 2011.

[28] I. J. Bahl and P. Bhartia, *Microstrip antennas.* Artech house, 1980.

[29] T. Huynh and K.-F. Lee, "Single-layer single-patch wideband microstrip antenna," *Electronics letters*, vol. 31, no. 16, pp. 1310–1312, 1995.

[30] J. Jung, W. Choi, and J. Choi, "A small wideband microstrip-fed monopole antenna," *IEEE microwave and wireless components letters*, vol. 15, no. 10, pp. 703–705, 2005.

[31] C.-K. Lin and S.-J. Chung, "A compact filtering microstrip antenna with quasi-elliptic broadside antenna gain response," *IEEE Antennas and wireless propagation letters*, vol. 10, pp. 381–384, 2011.

[32] P. F. Hu, Y. M. Pan, K. W. Leung, and X. Y. Zhang, "Wide-/dual-band omnidirectional filtering dielectric resonator antennas," *IEEE Transactions on Antennas and Propagation*, vol. 66, no. 5, pp. 2622–2627, 2018.

[33] J. Y. Jin, S. Liao, and Q. Xue, "Design of filtering-radiating patch antennas with tunable radiation nulls for high selectivity," *IEEE Transactions on Antennas and Propagation*, vol. 66, no. 4, pp. 2125–2130, 2018.

[34] M. Barbuto, F. Trotta, F. Bilotti, and A. Toscano, "Design and experimental validation of dual-band circularly polarised horn filtenna," *Electronics Letters*, vol. 53, no. 10, pp. 641–642.

[35] M. Barbuto, F. Trotta, F. Bilotti, and A. Toscano, "Filtering chiral particle for rotating the polarization state of antennas and waveguides components," *IEEE Transactions on Antennas and Propagation*, vol. 65, no. 3, pp. 1468–1471, 2017.

[36] R. J. Cameron, "Advanced coupling matrix synthesis techniques for microwave filters," *IEEE Transactions on Microwave Theory and Techniques*, vol. 51, no. 1, pp. 1–10, 2003.

[37] S. Amari, "Direct synthesis of folded symmetric resonator filters with source-load coupling," *IEEE Microwave and Wireless Components Letters*, vol. 11, no. 6, pp. 264–266, 2001.

[38] W.-H. Tu and K. Chang, "Compact microstrip bandstop filter using open stub and spurline," *IEEE Microwave and Wireless Components Letters*, vol. 15, no. 4, pp. 268–270, 2005.

[39] F. J. Pollack, "New microarchitecture challenges in the coming generations of cmos process technologies (keynote address)," in *Proceedings of the 32nd annual ACM/IEEE international symposium on Microarchitecture*, p. 2, IEEE Computer Society, 1999.

[40] K. Dhwaj, J. Kovitz, H. Tian, L. Jiang, and T. Itoh, "Half-mode cavity based planar filtering antenna with controllable transmission zeroes," *IEEE Antennas and Wireless Propagation Letters*, 2018.

[41] Y. Yusuf, H. Cheng, and X. Gong, "A seamless integration of 3-d vertical filters with highly efficient slot antennas," *IEEE Transactions on Antennas and Propagation*, vol. 59, pp. 4016–4022, Nov 2011.

[42] H. Chu, C. Jin, J. X. Chen, and Y. X. Guo, "A 3-d millimeter-wave filtering antenna with high selectivity and low cross-polarization," *IEEE Transactions on Antennas and Propagation*, vol. 63, pp. 2375–2380, May 2015.

[43] Y. Yusuf and X. Gong, "Compact low-loss integration of high- q 3-d filters with highly efficient antennas," *IEEE Transactions on Microwave Theory and Techniques*, vol. 59, pp. 857–865, April 2011.

[44] T. Kaufmann and C. Fumeaux, "Wearable textile half-mode substrate-integrated cavity antenna using embroidered vias," *IEEE Antennas and Wireless Propagation Letters*, vol. 12, pp. 805–808, 2013.

[45] B. Potelon, J.-F. Favennec, C. Quendo, E. Rius, C. Person, and J.-C. Bohorquez, "Design of a substrate integrated waveguide (siw) filter using a novel topology of coupling," *IEEE Microwave and Wireless Components Letters*, vol. 18, no. 9, pp. 596–598, 2008.

[46] S. Stuchly, C. Sibbald, and J. Anderson, "A new aperture admittance model for open-ended waveguides," *IEEE transactions on microwave theory and techniques*, vol. 42, no. 2, pp. 192–198, 1994.

[47] K. Dhwaj, H. Tian, and T. Itoh, "Low-profile dual-band filtering antenna using common planar cavity," *IEEE Antennas and Wireless Propagation Letters*, pp. 1–1, 2018.

[48] C.-Y. Hsieh, C.-H. Wu, and T.-G. Ma, "A compact dual-band filtering patch antenna using step impedance resonators," *IEEE Antennas and wireless propagation letters*, vol. 14, pp. 1056–1059, 2015.

[49] D. M. Pozar, *Microwave engineering 3rd.* John Wiley & Sons, 2005.

[50] S. Mukherjee and A. Biswas, "Design of self-diplexing substrate integrated waveguide cavity-backed slot antenna," *IEEE Antennas and Wireless Propagation Letters*, vol. 15, pp. 1775–1778, 2016.

[51] A. Oliner, "The impedance properties of narrow radiating slots in the broad face of rectangular waveguide: Part i–theory," *IRE Transactions on Antennas and Propagation*, vol. 5, no. 1, pp. 4–11, 1957.

[52] C. X. Mao, S. Gao, Y. Wang, B. Sanz-Izquierdo, Z. Wang, F. Qin, Q. X. Chu, J. Li, G. Wei, and J. Xu, "Dual-band patch antenna with filtering performance and harmonic suppression," *IEEE Transactions on Antennas and Propagation*, vol. 64, pp. 4074–4077, Sept 2016.

[53] X. Y. Zhang, Y. Zhang, Y. M. Pan, and W. Duan, "Low-profile dual-band filtering patch antenna and its application to lte mimo system," *IEEE Transactions on Antennas and Propagation*, vol. 65, pp. 103–113, Jan 2017.

[54] K. Dhwaj, X. Li, L. J. Jiang, and T. Itoh, "Low-profile diplexing filter/antenna based on common radiating cavity with quasi-elliptic response," *IEEE Antennas and Wireless Propagation Letters*, vol. 17, no. 10, pp. 1783–1787, 2018.

[55] Y.-J. Lee, J.-H. Tarng, and S.-J. Chung, "A filtering diplexing antenna for dual-band operation with similar radiation patterns and low cross-polarization levels," *IEEE Antennas and Wireless Propagation Letters*, vol. 16, pp. 58–61, 2017.

[56] X.-J. Lin, Z.-M. Xie, P.-S. Zhang, and Y. Zhang, "A broadband filtering duplex patch antenna with high isolation," *IEEE Antennas and Wireless Propagation Letters*, vol. 16, pp. 1937–1940, 2017.

[57] C.-X. Mao, S. Gao, Y. Wang, Y. Liu, X.-X. Yang, Z.-Q. Cheng, and Y.-L. Geng, "Integrated dual-band filtering/duplexing antennas," *IEEE Access*, vol. 6, pp. 8403–8411, 2018.

[58] Z. Kordiboroujeni, L. Locke, and J. Bornemann, "A diplexing antenna system in substrate integrated waveguide technology," in *Antennas and Propagation & USNC/URSI National Radio Science Meeting, 2015 IEEE International Symposium on*, pp. 1042–1043, IEEE, 2015.

[59] C.-X. Mao, S. Gao, Y. Wang, F. Qin, and Q.-X. Chu, "Compact highly integrated planar duplex antenna for wireless communications," *IEEE Transactions on Microwave Theory and Techniques*, vol. 64, no. 7, pp. 2006–2013, 2016.

[60] A. E. Atia and A. E. Williams, "Narrow-bandpass waveguide filters," *IEEE Transactions on Microwave Theory and Techniques*, vol. 20, no. 4, pp. 258–265, 1972.

[61] S. Shin and R. V. Snyder, "At least n+ 1 finite transmission zeros using frequency-variant negative source-load coupling," *IEEE microwave and wireless components letters*, vol. 13, no. 3, pp. 117–119, 2003.

[62] C. Icheln, J. Krogerus, and P. Vainikainen, "Use of balun chokes in small-antenna radiation measurements," *IEEE Transactions on Instrumentation and Measurement*, vol. 53, no. 2, pp. 498–506, 2004.

[63] K. Dhwaj, L. Jiang, and T. Itoh, "Dual-band filtering antenna with novel transmission zero characteristics," *IEEE Antennas and Wireless Propagation Letters*, 2018.

[64] K. Dhwaj, J. M. Kovitz, R. Al-Hadi, and T. Itoh, "Compact dual-band filtering antenna based on capacitor loaded patch radiator," in *Microwave Conference (APMC), 2017 IEEE Asia Pacific*, pp. 1188–1191, IEEE, 2017.

[65] J.-H. Lee, N. Kidera, G. DeJean, S. Pinel, J. Laskar, and M. M. Tentzeris, "A v-band front-end with 3-d integrated cavity filters/duplexers and antenna in ltcc technologies," *IEEE Transactions on Microwave Theory and Techniques*, vol. 54, no. 7, pp. 2925–2936, 2006.

[66] H. M. Cheema and A. Shamim, "The last barrier: on-chip antennas," *IEEE Microwave Magazine*, vol. 14, no. 1, pp. 79–91, 2013.

[67] S. Pan and F. Capolino, "Design of a cmos on-chip slot antenna with extremely flat cavity at 140 ghz," *IEEE Antennas and Wireless Propagation Letters*, vol. 10, pp. 827–830, 2011.

[68] G. Q. Luo, Z. F. Hu, L. X. Dong, and L. L. Sun, "Planar slot antenna backed by substrate integrated waveguide cavity," *IEEE Antennas Wireless Propag. Lett*, vol. 7, no. 1, pp. 236–239, 2008.

[69] K. Dhwaj, Y. Zhao, R. Al Hadi, X. Li, F. M.-C. Chang, and T. Itoh, "A 0.55 thz on-chip substrate integrated waveguide antenna," in *2018 43rd International Conference on Infrared, Millimeter, and Terahertz Waves (IRMMW-THz)*, pp. 1–2, IEEE, 2018.

[70] Y. Zhao, H.-C. Lu, H.-P. Chen, Y.-T. Chang, R. Huang, H.-N. Chen, C. Jou, F.-L. Hsueh, and M.-C. F. Chang, "A 0.54-0.55 thz 2× 4 coherent source array with eirp of 24.4 dbm in 65nm cmos technology," in *Microwave Symposium (IMS), 2015 IEEE MTT-S International*, pp. 1–3, IEEE, 2015.